Non-Parametric Estimation of Uncertain Closed-Loop Multivariate Frequency Response for Stability Assurance

A THESIS
SUBMITTED TO THE FACULTY OF THE GRADUATE SCHOOL
OF THE UNIVERSITY OF MINNESOTA
BY

Christopher D. Regan

IN PARTIAL FULFILLMENT OF THE REQUIREMENTS
FOR THE DEGREE OF
Doctor of Philosophy

Peter J. Seiler

March, 2022

Acknowledgements

My interest in "real-time stability margin" estimation started when I was a relatively new flight control and dynamics engineer. I'd been tasked with implementing a "RTSM" system for use during flight envelope expansion of the X-48B. It was suggested that I talk to "Boz"; John Bosworth was THE person to talk to about all things related to assessing stability margins from real world flight data.

The machination required to turn flight data into Bode plots was well established at that point; after all this was the fourth or fifth time a similar system had been implemented. What was not apparent was the intuition required to quickly evaluate the frequency response plots, mentally filter the signal from the noise, and make a real-time call. It is easy to say flight testing should follow a safe and a conservative approach; it is a whole different experience to be in the seat to make the call.

Boz was the kind of engineering role-model that made it easier to make safe calls, to follow your intuition if it's saying slow down. That's what he did. On numerous occasions we did slow down, performed repeated excitations if the results didn't quite seem right. Or that particular little wiggle in the Bode plot showed up at a sensitive frequency.

I've used Boz's 1997 publication on multivariable stability-margins estimation with the X-31A as the jumping off point for this study. There are a few similar publications that proceeded the X-31A use case, and several following that incrementally built upon it, but in most meaningful ways RTSM as described by Boz in 1997 has been the standard. It's now been at least 15 years since I first asked about RTSM, and I think I've finally expanded the envelope.

Dedication

To Ayla and Rue, who would often wonder why I stayed up late some nights during the last five years. Well, it's a bit complicated, and I look forward to explaining it all to you some day.

Abstract

System identification of closed-loop, multivariate systems presents a complex challenge; the use case for this study is on estimation for the purpose of stability margin assurance. Assessing both the nominal, or "best", estimated stability margins and the uncertainty range of those estimates are critical. This challenge is addressed by subjecting the system to multisine excitations and evaluating the response at both the excited frequencies and a set of null frequencies that are interleaved with the excited frequencies. This unique form of frequency separation allows for isolation of the response due to disturbances; which provides a critical source of estimation uncertainty. Additional sources of uncertainty, arising from response variations with time and spectral leakage, are combined to form a total estimated uncertainty. The impact of nonlinearities in the response are addressed, along with a particular approach to identification of nonlinearities. System stability assessment is performed, that directly accounts for estimation uncertainty. The approach to system estimation and stability assessment requires minimal prior knowledge and relies on only *in situ* data; the result is an independent assurance of system stability.

Contents

List of Tables

List of Figures

Chapter 1

Introduction

Introduction of new systems to practice generally presents a significant level of uncertainty, as models of real systems are necessarily based on imperfect knowledge. Often the presence of uncertain models, variations in the operating environments, or imperfect measurements motivate the application of a feedback control system. However, the presence of a control system presents a confounding problem for improving knowledge of the system itself.

1.1 Motivation

A representative system block diagram is presented in Figure 1.1. The controller, $K(s)$, and plant, $G(s)$, are presented as linear time-invariant systems and may be multivariate, multi-input multi-output (MIMO), systems. An error signal, e, is the tracking error signal for the controller; based on the reference command, r, and measured plant output, z. The signal n provides an exogenous additive output plant disturbance; this disturbance is treated generally and may contain elements of input disturbances and functions of the plant itself. Signals r, z, e, and u are directly measurable; n and y are not measured.
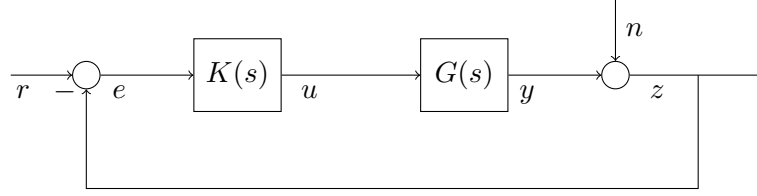
Figure 1.1: System Block Diagram.

Several useful systems can be identified from the block diagram depicted in Figure 1.1. If both the plant and controller are sufficiently stable, then signals in the closed-loop response could be opened to aid in identification. For example, it is often desirable to identify the plant response, $G(s)$; by opening the control signal, u, and injecting an excitation, u_{ex}, directly into the plant system; the plant response can be estimated with signals u_{ex} and z. Another use case is to identify a loop function of the system, $G(s)K(s)$ or $K(s)G(s)$, for stability assessment. Again, opening the control signal, u, and injecting an excitation, u_{ex}, into the plant system allows for estimation of $G(s)K(s)$ with the excitation, u_{ex}, and the return command, u. The other loop function, $K(s)G(s)$, could be estimated by opening the feedback signal, z, and using r as the excitation and z as the output signal. However, for many real-world systems, the loop closures must remain intact, this may be necessary due to the plant or controller being unstable or due to operational restrictions. This thesis will deal with the frequency response estimation (FRE) technique under the assumption that the loop closures must remain intact.

A critical element of any identification problem is estimation of the uncertainty associated with the estimate itself. In a closed-loop system, the content of the disturbance signal, n, will appear in all signals in the feedback loop; z, e, u, and y. This presents a challenge for estimating uncertainty, as the signals in the feedback loop become correlated with the unknown disturbance.

Much of the work in this study addresses the estimation of multivariate closed-loop systems in a fairly general sense. However, the particular interest here is for application in identification of flight vehicle characteristics; where the closed-loop response identification, plant identification, and stability assessment are of interest. In addition to addressing the challenge of identification of closed-loop MIMO systems, this work has been developed with the intent of real-time applications and applications that demand

time efficiency. The desire for time efficiency manifests in cases where the vehicle only operates at a condition for a short period of time and in cases where there is significant variation in the operational environment.

This study specifically addresses system identification for stability assessment of closed-loop multivariate systems in the presence of disturbances. The approach here allows all control system loops to remain intact; measures are assumed available for r, z, e, and u in Figure 1.1. Excitation signals are injected into the operating system to allow estimation of both a nominal system and the uncertainty of the estimate: injection onto u will yield stability estimates for $G(s)K(s)$ and injection onto r or e will yield stability estimates for $K(s)G(s)$. The result is a non-parametric method that requires minimal prior knowledge that results in a comprehensive stability assessment accounting for the nominal system estimate and estimation uncertainty.

1.2 Literature Review

The general modeling and identification problems encountered here are ubiquitous and are generally treated within the general topics: signal processing, system identification, and control analysis.

Much of the necessary background in signal processing and system identification can be gleaned from the common texts on the topic. Signal processing is well addressed in the popular texts by Bendat [1], Pintelon [2], Oppenheim [3], and Rao [4]. System identification is well addressed in Ljung [5, 6], Tischler [7, 8], and Klein and Morelli [9, 10]. Necessary control system modeling and stability analysis, with particular emphasis on robust multivariate stability analysis, is sufficiently addressed in the text by Skogestad and Postlethwaite [11].

One of the motivating use cases for this work is in-flight assessment of flight vehicle stability. Many of the published works on in-flight stability estimation have been produced by the NASA Armstrong Flight Research Center (formerly known as the Dryden Flight Research Facility and Dryden Flight Research Center). The original motivation for their development was flight testing statically unstable X-29A aircraft. The X-29A required an active flight control system to maintain flight safety, therefore estimation of the system response and stability could only be obtained from closed-loop response.

The basic approach is outlined in publications by Bosworth and West [12], Gera and Bosworth [13], and Clarke, Burken, Bosworth, and Bauer. [14]. Estimation of the system stability margins from flight data used a combination of pilot inputs and automated frequency sweeps, with offline computation of the gain and phase margins.

In-flight stability was further developed by Burken and Bosworth with the incorporation of multisine excitations and multivariate stability analysis, as part of the X-31A aircraft flight program [15, 16, 17]. As in the X-29A envelope expansion, the X-31A stability analysis occurred in near real-time, with flight test engineers monitoring the results. Key to the application in a flight test program was the comparison of the flight-derived FRE with *a priori* linear model frequency responses. Computation of structured singular values, using *a priori* uncertainty estimates, was published by Miotto and Paduano [18].

The X-31A in-flight stability approach, for closed-loop MIMO systems as described in Bosworth and Burken [17], is the basis for several additional publications. Balough [19] applied a variation to flight testing the X-36, Baumann [20] applied more time-efficient multisine excitations, detailed by Morelli [21], to the hypersonic X-43A, Regan [22] applied the technique to flight testing the X-48B aircraft. These examples of closed-loop stability estimation using multisine excitations either neglect the estimation uncertainty or apply *a priori* determined uncertainty to the nominal results.

Several publications by Lind and Brenner established methods for robust stability estimates focused on aeroelastic response [23, 24, 25]. Aircraft flutter margins are often presented in the form of a margin in airspeed to the unstable flutter boundary. Projecting the estimated local system robust stability margin to a flutter margin (in terms of airspeed) necessitates *a priori* models and some form of model updating. Several approaches to robust stability margin specification are presented in this context by Brenner [24]. Model updating and flutter margin predictions are described by Lind in the context of an open-loop aeroelastic system [25].

An approach to estimating non-parametric uncertainty was published by Lichter, Bateman, and Balas [26]. The method reported by Lichter used multisine excitations and the variance of multiple estimates as the basis for establishing uncertainty in frequency response; robust stability margins incorporating the estimated nominal and uncertainty were also presented [26]. A particular method is presented to project the

estimated plant FRE, nominal and uncertain, through a non-linear transformation to provide margins of the closed-loop system. The stability margin results were based on single-input single-output (SISO) loop-at-a-time type stability assessments.

Recently, several approaches have been published to address plant model estimation, within closed-loop systems, in the presence of disturbances. Grauer and Morelli developed a method for estimating frequency responses (using multisine excitations), and uncertainties arising from measurement noise, as well as propagating those uncertainties to a final estimate [27]. Grauer and Boucher further developed the approach by estimating the measurement noise at high frequency and applying a deconvolution scheme to project the uncertainty to the frequency range of interest [28]. Grauer and Boucher also presented a technique for handling correlation that arises in closed-loop system identification [29], some advancement in frequency-domain methods [30], and *in situ* characterization of turbulence [31].

1.3 Overview and Contributions

This study is focused on the estimation of robust stability margins purely from *in situ* measurements. The scope of the study is limited to non-parametric methods, and more specifically to application of spectral methods. While the motivation here is *in situ* stability assessment, the methods can be readily adapted to other estimation objectives in closed-loop systems.

The thesis is organized as follows:

- Chapter 2 establishes the essential concepts required for the FRE, specifically an overview of multisine excitations and the required fundamentals of spectral analysis are provided. Specification of a null frequency set is defined in order to estimate the spectra of the disturbance signal.

- Chapter 3 addresses the inherent errors that arise from the FRE. Several diagnostic metrics to quantify errors are presented along with mitigation strategies to minimize the impact of estimation error. Estimated uncertainties are first quantified and then propagated to the final estimate.

- Chapter 4 applies the estimation techniques to multivariate, closed-loop stability analysis.

- Chapter 5 presents limited results from application to aircraft simulation and flight tests.

Prior art for specification of multisine excitation signals has been somewhat *ad hoc* and relies on heuristics to determine suitable excitation amplitude and duration. Characteristics of the multisine excitation are exploited in spectral analysis described in prior art, however the specific impacts of excitation definition on accuracy and resolution have not been established in literature. The emphasis here on quantifying uncertainty has warranted developing a means of specifying multisine parameters that allows for quantitative trade-offs in terms of accuracy, amplitude, duration, and resolution.

Methods for assessing stability of uncertain MIMO systems has been well established [11]. Application of estimated robust stability methods with estimated frequency responses has only partially been addressed in the literature: Miotto [18] used *a priori* uncertainty bounds in a MIMO robust stability assessment, Lichter [26] used estimated uncertainty and a stochastic sampling approach to determine robust stability. Prior applications of stability assessment have relied upon *a priori* uncertainty specifications, require a known controller model, or necessitates breaking one or more feedback signals.

This work has advanced the prior practices in the following key areas.

- A novel approach to the estimation of uncertainty arising from disturbances in the closed-loop response is presented based on the concept of a null frequency basis that does not rely on *a priori* models. The null frequency concept is introduced in relation to the excitation frequencies in Section 2.1; spectral analysis and application to multivariate systems are addressed for the excitation and null frequencies in Section 2.2 and Section 2.3, respectively.

- Quantification of multisine excitations to yield desired estimation accuracy and resolution are developed and related to the specification of multisine duration and amplitude. This results in reduced reliance on *ad hoc* and heuristic approaches to excitation design. The critical relationships are developed in the sections on uncertainty due to disturbances and leakage in Section 3.2.

- Total estimation uncertainty has been developed to leverage additional information arising from signals in the null frequency basis. Uncertainty due to system disturbances, system variation, disturbance variation, and spectral leakage are accounted; along with applicable diagnostic metrics. Uncertainty sources are discussed in Section 3.2 and propagated to form a total estimation uncertainty in Section 3.3.

- A framework for refining an excitation in real-time based primarily on *in situ* estimates is presented in a specific application example in Section 3.5.

- Application of the nominal and uncertain system estimates are shown to be applicable for use in closed-loop MIMO robust stability assessment. Prior application of robust stability techniques utilized *a priori* uncertainty models of a form amenable to existing robust stability analysis frameworks, the form of the estimated uncertainty required derivation of an alternative formulation for robust stability. Specification of the nominal and robust stability definitions, using estimated uncertainty, is discussed throughout Chapter 4.

This work has also been developed for real-time applications and applications that demand time efficiency. The examples used throughout this thesis use an off-line Fourier transform for which there is an equivalent recursive form that is suitable to real-time application. The FRE and stability assessments provide a very systematic approach for the nominal and uncertainty estimates; this could significantly reduce the reliance on engineering judgement in stability evaluation during flight test.

This work also resulted in several additional finding that should be addressed within the context of the application of multisine excitations in general. First, mean square coherence is often presented in literature as providing a means of determining the degree of nonlinearity in a system response. For multisine excitations (or any periodic signal), a nonlinear system response can be shown to preserve perfect coherence. In much of the literature, the actual nonlinearities addressed are changes in operating point; however, in other cases, coherence is used incorrectly to indicate the absence of a broader definition of nonlinearity. Nonlinearities are discussed in brief in Section 3.4; coherence in the presence of nonlinearities is addressed via a servo mechanism example in Section 3.5.1. Second, it is well established that spectral leakage for a multisine signal is periodically

zero. This behavior is often used to neglect leakage as a contributor to uncertainty when the excitation signal is periodic. However, for signals that contain both periodic and non-periodic components, only spectral leakage of the periodic components of the signal can be safely neglected. Leakage and the distinction between the leakage of periodic and non-periodic signals is discussed in Section 3.2.2.

Chapter 2

Frequency Response Estimation

Frequency Response Estimation is a broadly employed technique for estimating the frequency response of a system based on the time histories of the input and output signals of the system. The estimated frequency response may be used directly for analysis, or may be an integral component of a broader system identification analysis. Necessary excitation conditions for FRE processes are provided by either replacing or augmenting the input signals with known excitation signals. Estimation of frequency response uncertainty using a specific class of excitations is emphasized.

An open-loop system block diagram is presented in Figure 2.1. A generic plant, $G(s)$, and disturbance model, $N(s)$, are presented as a linear time-invariant systems and may be MIMO systems. The plant has an input signal, u, and output signal, y. The signal m provides an exogenous source for Gaussian white noise (GWN); and acts through $N(s)$ to disturb the plant output. Signals u and z are directly measurable.
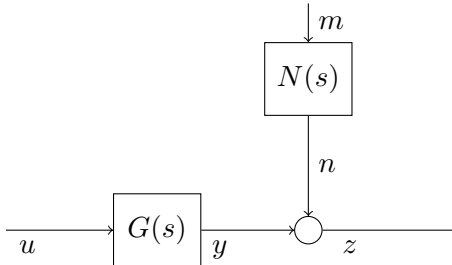
Figure 2.1: Simplified MIMO open-loop system block diagram.

Frequency Response Estimation is a common topic in literature. The principal objective of FRE is to generate an estimate of the plant as $\hat{G}(s)$. A secondary objective of FRE is to also provide an error estimation, as a measure of how close $\hat{G}(s)$ is to $G(s)$. Many of the essential elements of FRE used in this study follow the definitions and procedures in [32] and [2].

A particular class of excitation known as a multisine will be introduced in Section 2.1. Spectral analysis for continuous and discrete systems are introduced in Section 2.2. Spectral analysis is expanded to multivariate systems in Section 2.3.

This thesis introduces a new concept referred to as the null frequency set. The null frequency set is first introduced in connection with the excitation frequency set in Section 2.1. Traditional spectral methods have been expanded to incorporate the notion of the null set in Section 2.2. Expansion of spectral analysis to multivariate systems, in Section 2.3, addresses evaluation of multivariate systems incorporating the null spectra.

2.1   Excitation and Null Frequencies

The excitations used for the FRE process are multisines as described in [21]. These excitations allow for multichannel excitation based on the principal that sine waves generated from any subset of harmonics of a fundamental frequency, ω_F, are mutually orthogonal. The set of the first H harmonic frequencies is depicted in Equation (2.1).

$$\Omega_H := \{i \ \omega_F \ : \ i \in I_H\} \qquad I_H = \{1, 2, \ldots, H\} \tag{2.1}$$

Excitation signals are computed following selection of desired excitation frequencies, where the excitation frequencies are members of the harmonic set; $I_E \subset I_H$ and $\Omega_E \subset \Omega_H$. The excitation frequency set is further decomposed into C channels, with each channel designated as $c \in \{1, 2, \ldots, C\}$. Each channel of the excitation selects a unique subset of indices and corresponding harmonic frequencies; $I_c \subset I_E$ and $\Omega_c \subset \Omega_E$. Thus, the intersection of any pair of excitation channel sets is empty: $\Omega_k \cap \Omega_j = \emptyset$ for $k \neq j$. Generation of each channel of the multisine excitations is shown in Equation (2.2).

$$u_c(t) := \sum_{i \in I_c} a_i \sin(\omega_i \ t + \varphi_i) \qquad I_c \subset I_E \tag{2.2}$$

Since the channels of the excitation signal are generated from unique sets of harmonic frequencies, the signals themselves are mutually orthogonal; $u_1 \perp u_2 \perp \ldots \perp u_c$. Orthogonality of the excitation signals can be validated by checking that the inner product of any two signals is zero; $\langle u_j, u_k \rangle = 0$ for $j \neq k$. The excitation amplitudes, a_i, are selected independently at each excitation frequency. Signal phases, φ_i, are generally selected to reduce the peak factor (sometimes referred to as crest factor) of the time signal, u_c, for each channel of the excitation. Reduction of peak factor is often desirable to minimize excursions from the operating condition during experimentation; large peak factor excitations are more likely to result in significant changes in operating condition and may encounter additional system nonlinearities. For example, in application to aircraft excitation, it is often desirable to maintain the aircraft flight condition near the initial trim condition. Peak factor is defined simply as the ratio of vector norms of the signal, as defined in Equation (2.3).

$$\mathrm{PF}(u_c) = \frac{||u_c||_\infty}{||u_c||_2} \tag{2.3}$$

Two methods for defining multisine phases are commonly encountered. Schroeder multisines are based on a heuristic equation for determining the component phase angle based on the frequency and amplitude of the signal that results in a low peak factor [33, 2]. Phase angles for Schroeder multisines are computed for an excitation set, Ω_E with M evenly spaced components, as shown in Equation (2.4).

$$\phi_m = \phi_1 - 2\pi \sum_{l=1}^{m-1} (m-l)p_l^2 \qquad m = \{1, 2, \ldots, M\}$$

$$\text{where: } p_l = \frac{1}{M}(\frac{a_l}{a_{max}})^2 \tag{2.4}$$

The other method for determination of component phase angles is referred to as optimal multisines (OMS). OMS seek a minimum peak factor signal through varying individual phase components; generally with OMS generation, a global minimum peak factor is impractical and unnecessary [21, 2]. Unlike Schroeder multisines, optimal multisines can be computed for each individual channel of the excitation signal and does not require the frequencies in the set be evenly spaced. The typical peak factor for Schroeder multisines are around 2.4 to 2.8 and the peak factor for OMS signals are

typically 2.0 [2]. Schroeder multisines will be used throughout due to the simplicity of generating the phase angles.

The null frequency set, Ω_N, is a subset of the set of harmonic frequencies, $\Omega_N \subset \Omega_H$, that are not contained in the excitation set, $\Omega_E \cap \Omega_N = \emptyset$. Any signal consisting of only frequencies in the null set are orthogonal to the excitation signals, $u_N \perp u_E$. In general, the excitation frequencies and null frequencies can be selected arbitrarily from a harmonic set, so long as they are mutually exclusive. Examples herein will use a simple approach to defining the excitation and null sets. For illustration of this simplified approach, define a set of harmonic frequencies and corresponding indices, $\Omega_H = \{\omega_1, \omega_2, \ldots, \omega_H\}$ and $I_H = \{1, 2, \ldots, H\}$.

Frequencies in the excitation set are then defined as distributed into three excitation channels ($C = 3$); denoted as sets 1, 2, and 3 with a "zippered" distribution Equation (2.5).

$$
\begin{aligned}
\Omega_1 &= \{\omega_1, \omega_7, \ldots, \omega_{M-4}\} \\
\Omega_2 &= \{\omega_3, \omega_9, \ldots, \omega_{M-2}\} \\
\Omega_3 &= \{\omega_5, \omega_{11}, \ldots, \omega_M\}
\end{aligned}
\tag{2.5}
$$

The three channels of the excitation signals are generated via Equation (2.2). The union of the three channels of the excitation signals is the excitation set; $\Omega_E = \Omega_1 \cup \Omega_2 \cup \Omega_3$. are depicted generically as members of the excitation signal in Equation (2.6).

$$
u_E(t) = \begin{bmatrix} u_1(t) \\ u_2(t) \\ u_3(t) \end{bmatrix}
\tag{2.6}
$$

The three channels of the excitation signal are generated with frequency sets Ω_1, Ω_2, and Ω_3, therefore, the signals are mutually orthogonal; $u_1 \perp u_2 \perp u_3$.

The null set is then selected as the intermediate frequencies between the frequencies in the excitation set Equation (2.7).

$$
\Omega_N = \{\omega_2, \omega_4, \ldots, \omega_{M-1}\}
\tag{2.7}
$$

The null set is orthogonal to the excitation set; $\Omega_N \perp \Omega_E$.

In practice, the FRE will use only real-valued, evenly sampled time-series. Discretization of the excitation definition is straightforward. The time-domain signals are sampled at times t_n, with interval, Δt, and for a finite number of samples, N, in Equation (2.8).

$$t_n = n\ \Delta t \qquad n \in \{1, 2, \ldots, N\} \tag{2.8}$$

The excitation time-series, $u_c[t_n]$, samples the excitation signal, $u_c(t)$. The duration of the time-series, T, must meet or exceed the duration required for the minimum excitation frequency: $T \geq \frac{2\pi}{\omega_{min}}$ where ω_{min} is the minimum excitation frequency. For discrete time-series, the maximum frequency in the time-series is constrained to the Nyquist frequency: $\omega_{Nyquist} := \frac{\pi}{\Delta t}$. An equivalent definition for harmonic frequencies defined as integer ratios of a fundamental frequency, $\Omega_H := \{\omega_F/I_H \ : \ I_H = 1, 2, \ldots, H\}$, this can be convenient when using the Nyquist frequency as the fundamental harmonic frequency in discrete systems.

Note that a null set can always be defined from a harmonic excitation set. If the excitation fundamental frequency is ω_F, then the same excitation set and a null set can be constructed with $\omega_F/2$.

2.1.1   Example - Schroeder Multisine Excitation

The prior zippered excitation with three channels is further developed for application in a discrete environment.

For this example, the signal is sampled at 50 Hz ($\Delta t = 0.02$ seconds) for a duration of 20 seconds. The minimum and maximum excitation frequencies are constrained by the time duration and Nyquist frequency. The frequency range of interest is 0.10 Hz to 10 Hz; $\omega_{min} = 0.628$ rad/sec and $\omega_{max} = 62.83$ rad/sec. The fundamental frequency for the harmonic set is 0.10 Hz: $\omega_F = 0.628$ rad/sec. Finally, the desired frequency spacing in the excitation time-series is 0.2 Hz: $\Delta\omega = 1.26$ rad/sec. The channels of the excitation set are shown in Equation (2.9).

$$\Omega_1 = 2\pi\{0.10, 0.70, \ldots, 9.10, 9.70\}$$
$$\Omega_2 = 2\pi\{0.30, 0.90, \ldots, 9.30, 9.90\} \tag{2.9}$$
$$\Omega_3 = 2\pi\{0.50, 1.10, \ldots, 8.90, 9.50\}$$

The excitation set itself is: $\Omega_E = \Omega_1 \cup \Omega_2 \cup \Omega_3$. Note that the highest frequency of the excitation has been decreased to 9.90 Hz, rather than the desired 10 Hz.

The null frequencies are taken to be between the excitation frequencies, Equation (2.10).

$$\Omega_N = 2\pi\{0.20, 0.40, 0.60, \ldots, 9.60, 9.80\} \tag{2.10}$$

The time-series is generated as a Schroeder multisine. The excitation frequency and phase for all three channels in the excitation are listed in Table 2.1.

Table 2.1:   Example three channel Schroeder multisine definition.

Channel #1		Channel #2		Channel #3	
Frequency [Hz]	Phase [deg]	Frequency [Hz]	Phase [deg]	Frequency [Hz]	Phase [deg]
0.10	10.046	0.30	38.845	0.50	458.774
0.70	409.552	0.90	434.995	1.10	523.302
1.30	386.750	1.50	408.838	1.70	525.523
1.90	301.640	2.10	320.374	2.30	825.436
2.50	514.223	2.70	529.601	2.90	703.041
3.10	664.498	3.30	676.521	3.50	878.339
3.70	392.465	3.90	761.134	4.10	991.329
4.30	778.125	4.50	783.438	4.70	1042.011
4.90	741.477	5.10	743.435	5.30	1390.386
5.50	642.521	5.70	1001.124	5.90	1316.452
6.10	841.258	6.30	836.506	6.50	1540.212
6.70	977.687	6.90	969.580	7.10	1701.663
7.30	1051.808	7.50	1040.346	7.70	1800.807
7.90	1063.622	8.10	1408.804	8.30	1837.643
8.50	1013.128	8.70	1354.955	8.90	2172.171
9.10	1260.326	9.30	1238.798	9.50	2084.392
9.70	1085.216	9.90	1420.333	10.10	2294.305

Each channel has been normalized such that the 2-norm ($\|u_c\|_2$) of each channel in the excitation time-series is unity, the component amplitudes are adjusted accordingly (the resulting amplitude is 0.34334 at all frequencies in Ω_E). The peak factors of the three channels are: 2.42, 2.50, and 2.45.

The three excitation time-series are shown in Figure 2.2.
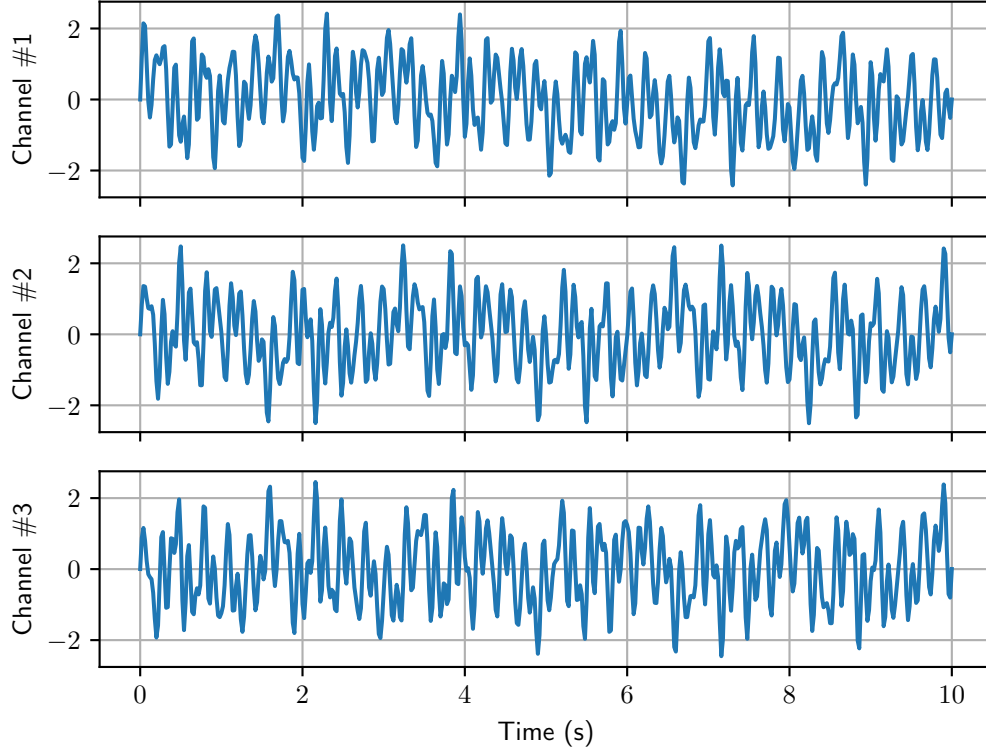
Figure 2.2: Example of a three channel Schroeder multisine time-series.

2.2 Spectral Analysis

The overall approach to spectral analysis follows a multi-periodogram approach, leveraging an ensemble of periodograms from segmented time-series. Individual "rough" periodograms are estimated via a Discrete Fourier Transform (DFT). Merging the rough periodograms will be briefly discussed here and further expanded in Chapter 3. The system depicted in Figure 2.1 is used as reference.

Spectral analysis is a general framework for transforming signals between the sampled "time-domain" and the "frequency-domain". The terms "time-domain" and the "frequency-domain" will be used to denote a signal or time-series in the time sense and its dual frequency based form, respectively. In literature, the time-domain generally

has a consistent meaning, whereas the definition of the frequency-domain is generally inferred by the transforms themselves; thus, the definition of the frequency-domain is induced from the transform definition. For example, the DFT and Chirp Z-transform (CZT) do not strictly operate upon equivalent vector spaces, although the generic term "frequency-domain", is sufficiently ubiquitous to readily adopt.

Appendix A contains a consistent set of assumptions and definitions for both continuous and discrete transforms. The subscript notation in Appendix A denoting the type of transform (or the specific vector-space), such as $X_{\mathcal{DFT}}$ to denote the DFT of x, will be eliminated.

Estimation error and uncertainty of the FRE will be discussed in Chapter 3.

2.2.1 Definitions in the Continuous Domain

In Figure 2.1 signals $u(t)$ and $y(t)$ represent the input and output of an LTI system, $G(s)$. The objective of FRE is to estimate $G(s)$ with only the input and output signals, u and z. In Figure 2.1 the measurable output, z, has an unknown disturbance, n, added such that: $z = y + n$.

The frequency response function (FRF) of two signals is defined as the ratio of the cross-spectra, $\Theta_{u \to z}$, and the input auto-spectrum, Θ_{uu}, in Equation (2.11).

$$\Theta_{u \to z}(j\omega) := \frac{\Phi_{u \to z}(j\omega)}{\Phi_{uu}(j\omega)} \tag{2.11}$$

The subscripted signal notation $u \to z$ is introduced (equivalent to zu) to accommodate the more complex symbology required later. The FRF is an approximation of the system, $G(s)$, for $s = j\omega$; the approximation converges as $T \to \infty$ for a stable system, Equation (2.12).

$$\Theta_{u \to z}(j\omega) \hat{=} G(j\omega) \tag{2.12}$$

Note that transient responses are neglected when taking only the harmonic component of s, such that $s = j\omega$. Thus, the free response due to both the initial conditions and any offsets from the steady state are neglected [34].

The mean-square coherence, $\gamma^2_{u \to z}$, of a pair of signals is defined in Equation (2.13).

$$\gamma_{u \to z}^2(j\omega) := \frac{|\Phi_{u \to z}(j\omega)|^2}{\Phi_{uu}(j\omega)\ \Phi_{zz}(j\omega)} \qquad 0 \le \gamma_{u \to z}^2(j\omega) \le 1 \tag{2.13}$$

Coherence is nominally unity for two signals representing the input and output signals of an LTI system as $T \to \infty$. Where again, the system's free response transient is neglected but will impact the estimate.

2.2.2 Estimates in the Finite and Discrete Domains

The discrete and finite spectra follow from the continuous spectra definitions above, where the perspective is that spectra are an intrinsic property of the continuous signal. Prior use of $u(t)$ to represent an infinite-continuous function of time will be replaced by a time-series $u[t_n]$ to represent the finite, discrete time-series. Similarly, the frequency-domain function $U(j\omega)$ will be replaced by $U[\omega]$.

The following spectral definitions rely upon time-series segmentation and windowing to produce a "rough" spectra estimate, denoted as $\tilde{\Phi}$. The "smooth" spectra estimates, denoted as $\hat{\Phi}$, will be introduced in Chapter 3 along with rationale for the time-series segmentation and windowing. In anticipation of the smoothing operation, the duration of each segment, T_s, and the number of segments, L, are defined. The number of samples in a time-series segment is: $N_s = T_s/\Delta t$.

The DFT will be the basis for the frequency transformation and spectral estimates. The general form of the DFT is given in Equation (A.7), a variation of the DFT for a rough estimate and time-series of length N_s is defined as Equation (2.14).

$$\tilde{X}[\omega_m] = \sum_{n=0}^{N_s-1} x[t_n]\ e^{-j(\omega_m \Delta t)n} \tag{2.14}$$

The frequency basis of the DFT in Equation (2.14) is stated generically as ω_m. The common frequency basis for the DFT provides "full resolution" in the frequency domain; $\omega_m = 2\pi \dfrac{m}{N\Delta t}$ for $m \in \{0, 1, \ldots, N\}$. Rather than computing the "full resolution" DFT, the frequency basis will be restricted to only a channel of the excitation frequency set or the null frequency set. The technique described herein easily generalizes to various forms of frequency transform so long as the frequency basis can be freely specified.

In the continuous definition, the approximation for $U(s)$ and $Z(s)$ required $s = j\omega$

and $T \to \infty$, and was subject to transients associated with the system's free response. In the discrete sampled approximations, the frequency transform is necessarily finite. Rather than converging at $T \to \infty$, the discrete transforms must be limited in time, which places a lower frequency bound for the approximation as: $\omega_{min} \geq 1/T$. The discrete approximation must also be bound by the Nyquist frequency, $\omega < \omega_{rate}/2$. Generally, it is reasonable to assume that the free transient response of the system is within the frequency range of interest and so the discrete transform will also be influenced by the transient response.

Detrending and window functions are applied to the time-series to mitigate the effects of using finite datasets that necessarily have discontinuities on the ends [35]. Linear detrending removes the time-series mean and linear trend; the result in the frequency-domain is elimination of the zero-frequency component and the frequency component associated with the duration of the finite time-series $(1/T)$ [34]. The window function is defined as a finite time-series, $w[t_n]$, and applied as an element-wise multiplication; $u_w[t_n] = w[t_n]\, u[t_n]$. The DFT then operates on the windowed time-series $u_w[t_n]$ and $z_w[t_n]$ to produce frequency-domain series $\tilde{U}_w[\omega]$ and $\tilde{Z}_w[\omega]$. Further discussion of window functions and their impact are discussed in Section 3.2.2.

Parseval's Theorem for discrete and finite systems, Theorem A.2, relates the signal total power in both the time-domain and frequency-domain and provides the basis for defining the PSD, Equation (A.16) and Equation (A.17). Spectral power loss due to application of both detrending and window functions are typically accounted for in the spectra definition rather than in the frequency transform itself [34]. Estimates of the rough auto-spectra and cross-spectra associated with the cth excitation channel are depicted in Equation (2.15).

$$\tilde{\Phi}_{uu}[\Omega_c] = \frac{2}{(\sum w)^2}\, |\tilde{U}[\Omega_c]|^2$$
$$\tilde{\Phi}_{zz}[\Omega_c] = \frac{2}{(\sum w)^2}\, |\tilde{Z}[\Omega_c]|^2 \qquad (2.15)$$
$$\tilde{\Phi}_{u \to z}[\Omega_c] = \frac{2}{(\sum w)^2}\, \tilde{U}^*[\Omega_c]\tilde{Z}[\Omega_c]$$

The common scale term in Equation (2.15) produces the power spectral density (PSD) and accounts for the power loss due to application of a window function, such

that the total power in Φ matches the total power in $u[t_n]$ (not the total power in $u_w[t_n]$). Estimates of the rough auto-spectra associated with the null frequency set are depicted in Equation (2.16).

$$
\begin{aligned}
\tilde{\Phi}_{uu}[\Omega_N] &= \frac{2}{(\sum w)^2} \, |\tilde{U}[\Omega_N]|^2 \\
\tilde{\Phi}_{zz}[\Omega_N] &= \frac{2}{(\sum w)^2} \, |\tilde{Z}[\Omega_N]|^2
\end{aligned}
\tag{2.16}
$$

The input signal, u, should have zero spectral power when evaluated on the null frequency set; so $\tilde{\Phi}_{uu}[\Omega_N]$ should be zero everywhere. $\tilde{\Phi}_{uu}[\Omega_N]$ is used in Chapter 3 to provide a diagnostic measure of spectral leakage. Similarly, $\tilde{\Phi}_{yy}[\Omega_N]$ should also be zero, though time-series y is not a measured signal. The output signal, z, evaluated on the null frequency set, provides an estimate of the spectral power contained in z that does not originate from y (or indirectly from u). At the null frequencies, the spectra in n is the same as the spectra in z; $\tilde{\Phi}_{nn}[\Omega_N] = \tilde{\Phi}_{zz}[\Omega_N]$. Note that $\tilde{\Phi}_{zz}[\Omega_N]$ is only taking a subset of frequencies contained within the time-series since the power in n is not solely contained within Ω_N. A "full resolution" PSD of n would contain $N/2$ unique frequencies; so the total power in z can be approximated as: $\frac{N}{2M_N}\tilde{\Phi}_{zz}$ where M_N in the number of frequencies in Ω_N.

The discrete FRF with time-series input u and output z is defined as the ratio of cross-spectrum and input auto-spectrum, Equation (2.17).

$$
\tilde{\Theta}_{u\to z}[\Omega_c] = \frac{\tilde{\Phi}_{u\to z}[\Omega_c]}{\tilde{\Phi}_{uu}[\Omega_c]}
\tag{2.17}
$$

The discrete FRF with input u and output n is defined as the square root of the input to output auto-spectra, Equation (2.18).

$$
\tilde{\Theta}_{u\to n}[\Omega_c] = \sqrt{\frac{\tilde{\Phi}_{zz}[\Omega_N]|_{\Omega_c}}{\tilde{\Phi}_{uu}[\Omega_c]}}
\tag{2.18}
$$

$\tilde{\Theta}_{u\to n}$ is strictly real-valued; u and n are uncorrelated. Equation (2.18) requires a change of frequency basis with $\tilde{\Phi}_{zz}[\Omega_N]$ transforming from the frequency basis Ω_N to basis Ω_c. Throughout this study, linear interpolation is used to change the frequency basis (to avoid interpolation across potential phase-wraps, all complex linear interpolation

is conducted in polar coordinates).

Smooth spectra estimates are produced via multiple independent rough spectra with the excitation frequencies; Equation (2.19).

$$\hat{\Phi}_{uu}[\Omega_c] = \mathrm{E}[\tilde{\Phi}_{uu}[\Omega_c]]$$
$$\hat{\Phi}_{zz}[\Omega_c] = \mathrm{E}[\tilde{\Phi}_{zz}[\Omega_c]] \tag{2.19}$$
$$\hat{\Phi}_{u \to z}[\Omega_c] = \mathrm{E}[\tilde{\Phi}_{u \to z}[\Omega_c]]$$

Smooth spectra estimates are using the null frequencies are defined in Equation (2.20).

$$\hat{\Phi}_{uu}[\Omega_N] = \mathrm{E}[\tilde{\Phi}_{uu}[\Omega_N]]$$
$$\hat{\Phi}_{zz}[\Omega_N] = \mathrm{E}[\tilde{\Phi}_{zz}[\Omega_N]] \tag{2.20}$$

The expected value E[ ] is taken as a simple mean for Φ_{uu} and Φ_{zz} (complex-valued spectra are averaged in polar coordinates to avoid the phase-wrapping problem noted for interpolation). In order for the expected values in Equation (2.19) to be bounded and convergent, the disturbance, n, and plant output, y, must be bounded; which implies that $G(s)$ and $N(s)$ must be stable.

Smooth FRF estimates are produced from multiple rough FRF estimates in both the excitation frequency sets and the null frequency set; Equation (2.21) and Equation (2.22).

$$\hat{\Theta}_{u \to z}[\Omega_c] = \mathrm{E}[\tilde{\Theta}_{u \to z}[\Omega_c]] \tag{2.21}$$

$$\hat{\Theta}_{u \to n}[\Omega_c] = \mathrm{E}[\tilde{\Theta}_{u \to n}[\Omega_c]] \tag{2.22}$$

The discrete FRF, $\hat{\Theta}_{u \to z}$, estimates the continuous FRF, $\Theta_{u \to z}$, which in turn estimates the plant G, Equation (2.23).

$$\hat{\Theta}_{u \to z}[\Omega_c] \mathrel{\hat{=}} \Theta_{u \to z}(j\omega) \mathrel{\hat{=}} G(j\omega) \tag{2.23}$$

The magnitude of $N(j\omega)$ can be estimated by using the PSD of the output signal in the null frequencies, $\Phi_{zz}[\Omega_N]$, and the fact the m is GWN with unity variance ($\Phi_{mm} = 1$). The estimation of the magnitude of $N(j\omega)$ is depicted in Equation (2.24).

$$\hat{\Theta}_{m \to n}[\Omega_N] = \sqrt{\frac{\hat{\Phi}_{zz}[\Omega_N]}{\Phi_{mm}[\Omega_N]}} = \sqrt{\hat{\Phi}_{zz}[\Omega_N]} \,\hat{=}\, |N(j\omega)| \qquad (2.24)$$

In practice, the source of the disturbances are unknown, the utility of Equation (2.24) is limited to verification exercises and will be used in Section 2.4. $\hat{\Theta}_{u \to n}$ will be a critical component for uncertainty quantification in Chapter 3.

Finally, the coherence of a pair of input and output time-series is defined for a rough estimate in Equation (2.25).

$$\tilde{\gamma}_{u \to z}^2[\omega] = \frac{|\tilde{\Phi}_{u \to z}[\omega]|^2}{\tilde{\Phi}_{uu}[\omega] \, \tilde{\Phi}_{zz}[\omega]} \qquad 0 \le \tilde{\gamma}_{u \to z}^2[\omega] \le 1 \qquad (2.25)$$

Pintelon [2] notes that if $\tilde{\gamma}$ is less than one, it indicates the presence of extraneous noise in the measurements, leakage errors of the frequency transform, or other inputs contributing to the output. Critically, nonlinearities do not impact coherence for purely periodic input signals, coherence is affected by nonlinear distortion and the presence of unaccounted signals that impact the system output [2]. The multitude of potential sources of coherence degradation makes its use as a estimation quality metric challenging.

A smooth version of the coherence is shown in Equation (2.26), where the smooth spectra estimates, rather than the rough spectra estimates, are used.

$$\hat{\gamma}_{u \to z}^2[\omega] = \frac{|\hat{\Phi}_{u \to z}[\omega]|^2}{\hat{\Phi}_{uu}[\omega] \, \hat{\Phi}_{zz}[\omega]} \qquad 0 \le \hat{\gamma}_{u \to z}^2[\omega] \le 1 \qquad (2.26)$$

The smooth coherence estimates the signal coherence, Equation (2.27).

$$\hat{\gamma}_{u \to z}^2[\omega] \,\hat{=}\, \gamma_{u \to z}^2(\omega) \qquad (2.27)$$

The form of Equation (2.17) is often referred to as the "H1" FRF method. The "H2" method relates the output spectra and cross-spectra as in: $\Theta_{H2} = \Phi_{zz}/\Phi_{u \to z}$. The difference between H1 and H2 methods is directly related to the magnitude of the coherence, such that: $|\Theta_{H1}| \le |G(s)| \le |\Theta_{H2}|$ where Θ_{H1} is defined in Equation (2.17). In the case of purely periodic input time-series, the "H1" method is the maximum likelihood estimator of $G(s)$ [2].

2.3   MIMO Estimate

In Section 2.2 the FRE process and FRF were presented for a channelized multisine excitation input. This results in a set of single-input multiple-output (SIMO) estimates (one SIMO estimate for each excitation channel). In this section, the FRE process will be expanded to merge the SIMO estimates into a single MIMO estimate. The basic approach to producing the MIMO estimate follows the approach outlined in [16, 17].

An index notation system is introduced such that u_i represents the ith input channel, and z_o represents the oth output channel. The number of input channels and output channels are denoted: C_i and C_o. The system $G_{u \to y}(s)$ then has dimension $C_o \times C_i$.

The previously presented SIMO FRF estimates are re-stated from Equation (2.17) with this expanded notation system, Equation (2.28).

$$\tilde{\Theta}_{u_i \to z}[\Omega_i] = \frac{\tilde{\Phi}_{u_i \to z_o}[\Omega_i]}{\tilde{\Phi}_{u_i u_i}[\Omega_i]} \quad o \in \{1, 2, \ldots, C_o\} \tag{2.28}$$

Equation (2.28) is taken at each channel of the input, $i \in \{1, 2, \ldots, C_i\}$, producing C_i individual SIMO estimates. Note that for a multisine excitation, the input auto-spectra are nonzero only if the excitation frequencies match the channel: $\phi_{u_i u_i}[\omega_i]$. For example, $\phi_{u_1 u_1}[\omega_2]$ would be zero, whereas $\phi_{u_1 u_1}[\omega_1]$ would be the nonzero excitation in channel 1.

To form a MIMO response matrix, each SIMO response estimate is evaluated on a consistent frequency basis; the natural choice is to use the basis of the full excitation set, Ω_E, and depicted in Equation (2.29).

$$\tilde{\Theta}_{u \to z}[\Omega_E] = \left[\ldots, \tilde{\Theta}_{u_i \to z}[\Omega_i]|_{\Omega_E}, \ldots \right] \qquad i \in \{1, 2, \ldots, C_i\} \tag{2.29}$$

In Equation (2.29) $\tilde{\Theta}_{u_i \to z}[\Omega_i]|_{\Omega_E}$ indicates a change of frequency basis of $\tilde{\Theta}_{u_i \to z_o}[\Omega_i]$ from Ω_i to Ω_E. Linear interpolation is again used to expand the frequency basis from Ω_i to Ω_E. The approach is amenable to both non-parametric higher order interpolation methods and parametric model fitting to evaluate the SIMO responses on a consistent frequency basis.

Evaluation of the null set is similar to the expansion of the excitation set to the full MIMO estimate, although it is slightly simplified because the input signal evaluated on

the null frequency set is zero everywhere, Equation (2.30).

$$\Phi_{u_i u_i}(\Omega_N) = 0.0 \qquad i \in \{1, 2, \ldots, C_i\} \tag{2.30}$$

The FRF from u to z in the null frequencies produces a series of SIMO response estimates; here the SIMO responses are all evaluated on the excitation basis, Equation (2.31).

$$\tilde{\Theta}_{u_i \to n}[\Omega_E] = \sqrt{\frac{\tilde{\Phi}_{z_o z_o}[\Omega_N]|_{\Omega_E}}{\tilde{\Phi}_{u_i u_i}[\Omega_i]|_{\Omega_E}}} \qquad o \in \{1, 2, \ldots, C_o\} \tag{2.31}$$

The expansion of Equation (2.31) to a MIMO system requires a consistent frequency basis, again Ω_E is the natural choice. Note that $\tilde{\Theta}_{u_i \to n}$ is real-valued, u is uncorrelated with n, so only the magnitude of the response function contains information. Each SIMO response matrix is simply concatenated to form the MIMO response matrix, Equation (2.32).

$$\tilde{\Theta}_{u \to n}[\Omega_E] = \left[\ldots, \tilde{\Theta}_{u_i \to n}[\Omega_E], \ldots \right] \qquad i \in \{1, 2, \ldots, C_i\} \tag{2.32}$$

The FRF of the excitation and null sets are maintained as distinct components.

In the preceding, the excitation and null FRF share a common input, $\tilde{\Phi}_{u_i u_i}$. An alternative formulation highlights that the signal-to-noise ratio (SNR) and noise-to-signal ratio, $\beta[\Omega_E]$, are also estimated through the segregation of frequency components, Equation (2.33).

$$\text{SNR} = \frac{1}{\tilde{\beta}[\Omega_E]} = \frac{\tilde{\Phi}_{z_o z_o}[\Omega_E]}{\tilde{\Phi}_{z_i z_i}[\Omega_N]|_{\Omega_E}} - 1 \tag{2.33}$$

$$i \in \{1, 2, \ldots, C_i\} \quad o \in \{1, 2, \ldots, C_o\}$$

The FRF matrix $\tilde{\Theta}_{u \to z}$ is complex-valued with dimension $C_o \times C_i$. The FRF null matrix $\tilde{\Theta}_{u \to n}$ (and the SNR matrix) is real-valued with dimension $C_o \times C_i$. Note that the FRF matrices could be rank deficient. For pure plant output disturbances, the columns of $\tilde{\Theta}_{u_i \to n_o}[\Omega_E]$ are linearly dependent; similarly, for pure plant input disturbances, the rows are linearly dependent.

2.4   Example - Open-Loop MIMO FRE

A simplified, open-loop MIMO system representing just a plant, $G(s)$, and output disturbance, n, is presented to illustrate the FRE method. The system block diagram is presented in Figure 2.3.
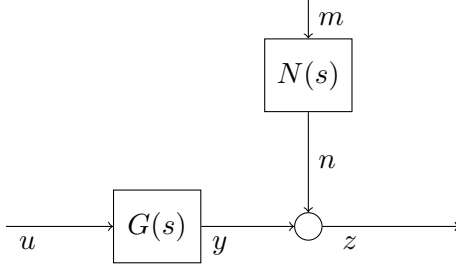
Figure 2.3: Example MIMO open-loop system block diagram.

The output equation is shown in Equation (2.34) and the parameterization of the components are detailed in Table 2.2.

$$
\begin{bmatrix} z_1 \\ z_2 \end{bmatrix} = \begin{bmatrix} G_{1\to1}(s) & G_{2\to1}(s) \\ G_{1\to2}(s) & G_{2\to2}(s) \end{bmatrix} \begin{bmatrix} u_1 \\ u_2 \end{bmatrix} + \begin{bmatrix} N_{1\to1}(s) & 0 \\ 0 & N_{2\to2}(s) \end{bmatrix} \begin{bmatrix} m_1 \\ m_2 \end{bmatrix} \tag{2.34}
$$

Table 2.2:   Plant and Controller system definitions.

Component	Parameterization			Transfer Function
$G_{1\to1}(s)$	$k = 1.0$	$\omega_N = 3$ Hz	$\zeta = 0.2$	$\dfrac{k\,\omega_N^2}{s^2 + 2\zeta\omega_N\,s + \omega_N^2}$
$G_{2\to1}(s)$	$k = 0.5$	$\omega_N = 5$ Hz	$\zeta = 0.3$	$\dfrac{k\,\omega_N^2}{s^2 + 2\zeta\omega_N\,s + \omega_N^2}$
$G_{1\to2}(s)$	$k = 0.25$	$\omega_N = 4$ Hz	$\zeta = 0.1$	$\dfrac{k\,\omega_N^2}{s^2 + 2\zeta\omega_N\,s + \omega_N^2}$
$G_{2\to2}(s)$	$k = 1.0$	$\omega_N = 6$ Hz	$\zeta = 0.4$	$\dfrac{k\,\omega_N^2}{s^2 + 2\zeta\omega_N\,s + \omega_N^2}$
$N_{1\to1}(s)$	$k = 0.125$	$\omega_N = 6$ Hz	$\zeta = 0.1$	$\dfrac{k(-s^2 + \omega_N^2)}{s^2 + 2\zeta\omega_N\,s + \omega_N^2}$
$N_{2\to2}(s)$	$k = 0.25$			k

The plant consists of four second-order transfer functions with varying gain, natural frequency, and damping. The noise model, $N(s)$, is driven by a zero-mean GWN input signal, m, with unity variance. The noise model was selected to produce a range of SNR levels throughout the frequency range of interest. The $N_{1\to1}$ component of the noise model has a low-damped response centered at 6 Hz, which will be shown to dominate the frequency response ($G_{1\to1}$ and $G_{2\to1}$ are attenuated prior to 6 Hz). The $N_{2\to2}$ component of the noise model matches the response gain of the $G_{1\to2}$ component at low frequencies; $N_{2\to2}$ dominates the frequency response after $G_{1\to2}$ has attenuated at high frequency.

A multisine excitation has been generated for frequencies between 0.05 Hz and 10 Hz, with 3 repetitions (total duration is 30 seconds). The excitation is injected into the system directly as the plant input, u. The resultant excitation and null frequency sets are detailed in Equation (2.35).

$$
\begin{aligned}
\Omega_1 &= 2\pi \ \{0.05, \ 0.45, \ \ldots, \ 9.25, \ 9.65\} \\
\Omega_2 &= 2\pi \ \{0.25, \ 0.65, \ \ldots, \ 9.45, \ 9.85\} \\
\Omega_E &= \Omega_1 \cup \Omega_2 \\
\Omega_N &= 2\pi \ \{0.15, \ 0.35, \ 0.55, \ \ldots, \ 9.55, \ 9.75\}
\end{aligned}
\tag{2.35}
$$

The frequency and phase of each component of the excitation is tabulated in Table 2.3; each component was generated with an amplitude of 0.04 and both channels of the excitation have a peak factor of 2.32.

Table 2.3:   Schroeder multisine definition.

Channel #1		Channel #2	
Frequency [Hz]	Phase [deg]	Frequency [Hz]	Phase [deg]
0.05	2.28972	0.25	4.22945
0.45	373.408	0.65	349.397
0.85	355.725	1.05	305.764
1.25	309.243	1.45	233.331
1.65	233.961	1.85	132.098
2.05	129.879	2.25	362.065
2.45	356.997	2.65	203.232
2.85	195.314	3.05	375.599
3.25	364.832	3.45	159.166
3.65	505.550	3.85	273.934
4.05	257.468	4.25	359.901
4.45	340.586	4.65	417.068
4.85	394.903	5.05	85.4350
5.25	420.421	5.45	445.002
5.65	417.139	5.85	415.769
6.05	385.057	6.25	357.736
6.45	324.175	6.65	270.903
6.85	594.492	7.05	155.271
7.25	476.010	7.45	370.838
7.65	688.728	7.85	197.605
8.05	512.646	8.25	355.572
8.45	667.764	8.65	484.739
8.85	434.081	9.05	225.106
9.25	531.599	9.45	296.673
9.65	600.317	9.85	339.441

Estimation of the defined system, $G(s)$, uses only the time-series u and z; m, n, y are not used in the estimate (in order to compare the disturbance estimate to the defined system disturbance, the signal m is assumed to be driven by as unity GWN). The frequency response was estimated with a "rectangular" window function.

A portion of the estimated power spectra for z_1 is depicted in Figure 2.4 and Figure 2.5.
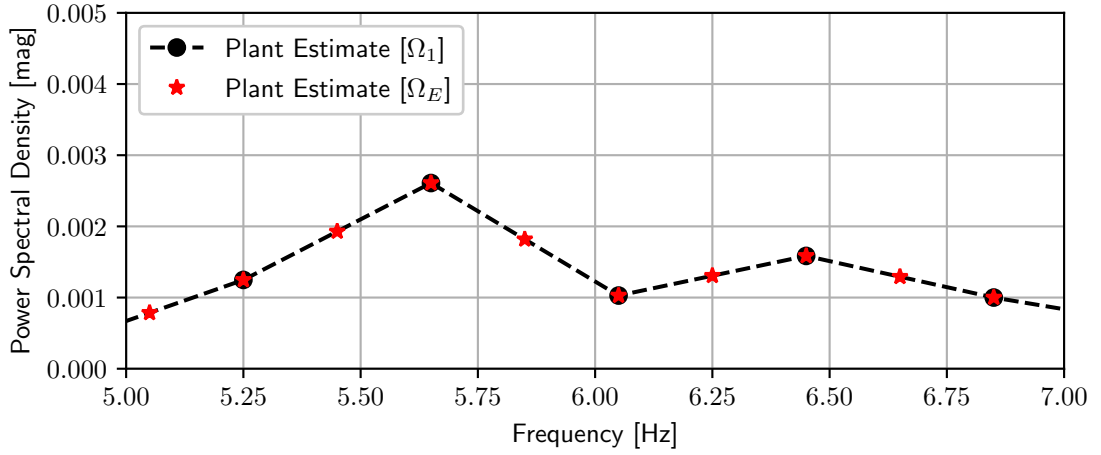
Figure 2.4: Power spectral density of z_1 showing the interpolation from the SIMO frequencies set, Ω_1, to the full set of excitation frequencies, Ω_E, to be incorporated in the MIMO estimate.
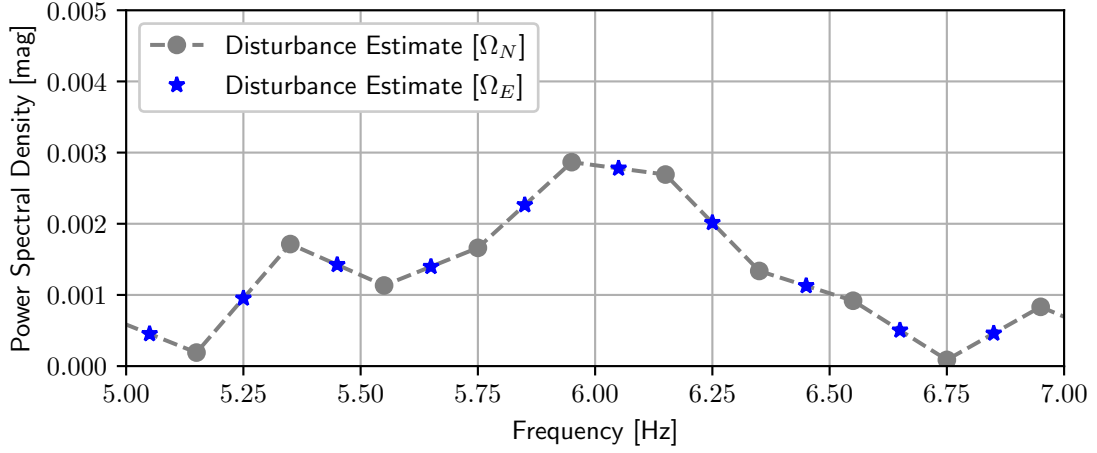
Figure 2.5: Power spectral density of z_1 showing the interpolation from the Null frequencies set, Ω_N, to the full set of excitation frequencies, Ω_E, to be incorporated in the MIMO estimate.

The interpolation scheme to evaluate both the excited channel frequencies, Ω_1 or Ω_2, and null components, Ω_N, of the spectra to the frequency basis used in the MIMO system, Ω_E, is highlighted.

A Bode plot corresponding to the $G_{1\to1}(s)$ element of the plant and the $N_{1\to1}(s)$ element of the disturbance is shown in Figure 2.6 along with the linear model and linear model disturbance.
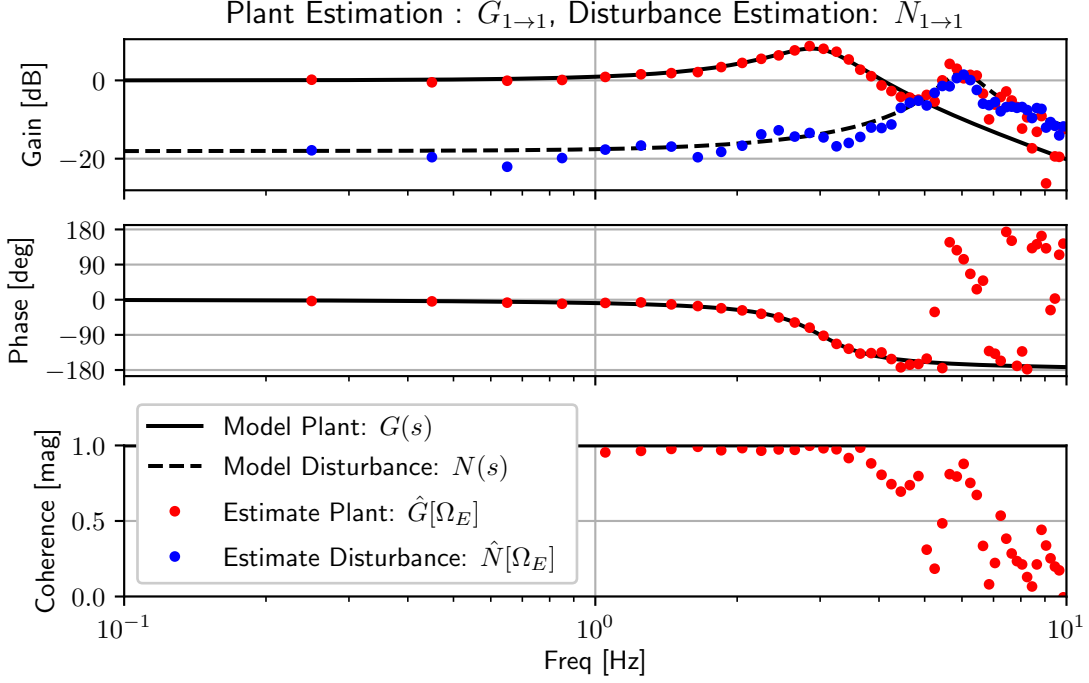
Figure 2.6: Bode plot of the FRE for u_1 to z_1 showing the plant model response and plant estimation as well as the disturbance model response and disturbance estimation.

The figure shows both the estimate of the nominal system, where $\hat{G}_{1\to1}[\omega] = \hat{\Theta}_{u_1 \to z_1}[\Omega_E]$ and the disturbance components of $\hat{N}_{1\to1}[\omega] = \hat{\Theta}_{m_1 \to n_1}[\Omega_E]$ generally align with the linear models. Note that the disturbance estimation does not contain any phase information, so only the gain plot is used to compare the modeled disturbance and estimated disturbance response. Relatively high plant estimation error is encountered near the peak of the disturbance response at 6 Hz. The disturbance peak also corresponds to a loss in coherence, as uncorrelated noise dominates the output spectra.

The Bode plot corresponding to the $G_{2\to1}(s)$ element of the plant is shown in Figure 2.7 along with the linear model.
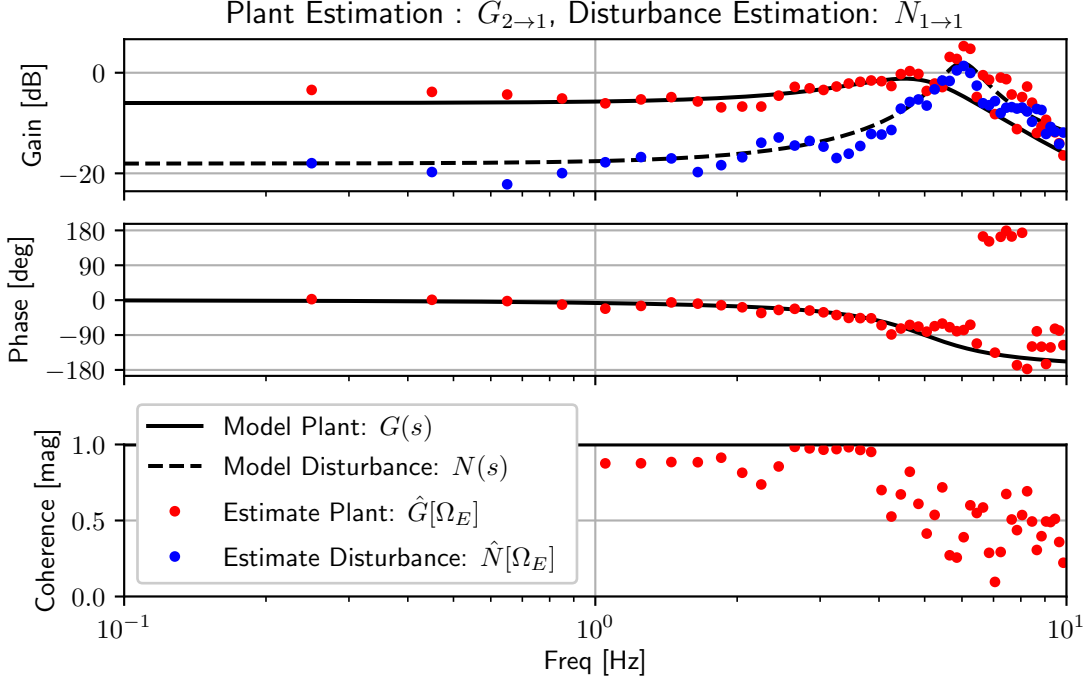
Figure 2.7: Bode plot of the FRE for u_2 to z_1 showing the plant model response and plant estimation as well as the disturbance model response and disturbance estimation.

The disturbance linear model and estimate is identical to that of Figure 2.6; highlighting that the disturbance estimates in this example are aligned with the output channels. The figure shows both the nominal and disturbance components of $\hat{G}_{2\rightarrow1}$ and $\hat{N}_{2\rightarrow1}$; again, the estimation in general follows the linear model at low frequency and has a relatively high error around the peak disturbance.

The Bode plot corresponding to the $G_{1\rightarrow2}(s)$ and $G_{2\rightarrow2}(s)$ components of the model and estimation response are shown in Figure 2.8 and Figure 2.9.
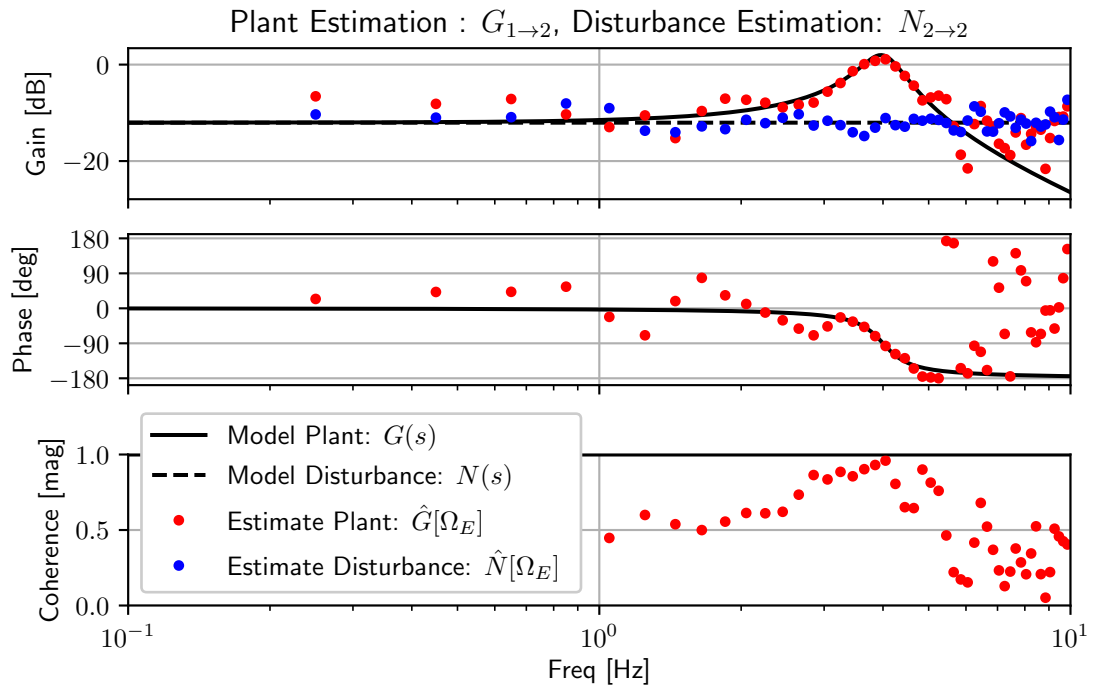
Figure 2.8: Bode plot of the FRE for u_1 to z_2 showing the plant model response and plant estimation as well as the disturbance model response and disturbance estimation.
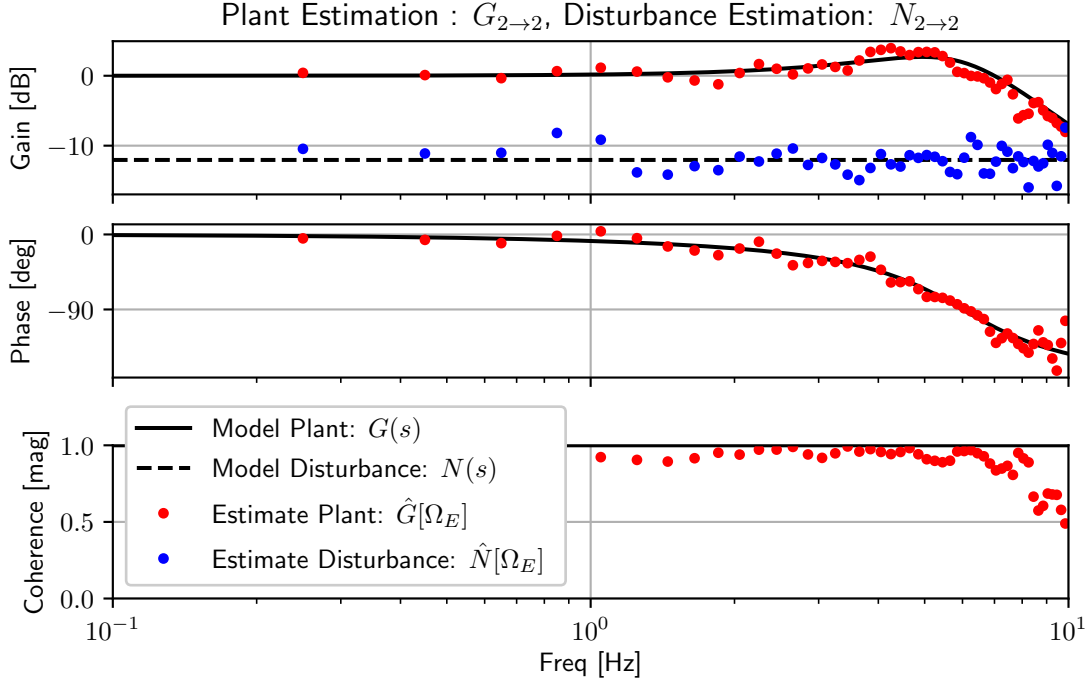
Figure 2.9: Bode plot of the FRE for u_2 to z_2 showing the plant model response and plant estimation as well as the disturbance model response and disturbance estimation.

Again, the estimates follow the linear models. The SNR of the second output channel yields a relatively high random error; however, the resulting variation in the resultant nominal system uncertainty estimate will be minimal.

This example shows that the FRE method allows simultaneous estimation of MIMO plant models and estimation of the disturbance model spectra. The orthogonal excitation signals enable isolation of channelized input-output frequency responses associated with the plant, as well as isolation of the noise. Estimation of the disturbance spectra will be a critical component of the quantification of estimation uncertainties; this example will be revisited for uncertainty quantification in Section 3.6.

Chapter 3

Uncertainty Quantification and Propagation

This chapter aims to quantify and propagate FRE uncertainty for use in the final objective, such as stability margin estimation. The approach to FRE outlined in Chapter 2 introduced key assumptions required for the validity of the FRF estimates; namely, the system must be linear, signals are stationary (at least wide-sense stationary such that the signal mean and variance are time-invariant). Disturbances, in the form of filtered noise, were previously introduced and will result in a significant source of estimation uncertainty. Spectral leakage, and the mitigation with windowing functions, were also introduced.

In the proceeding, "estimation error" and "uncertainty" have a similar meaning; "uncertainty" will be used in relation to in-situ applications, where the "uncertainty" is estimated along with the nominal response estimate. "Estimation error" will be used in direct applications where a truth comparison is available or an *a priori* analysis allows some estimation of error.

The

In system identification literature, the term "nonlinearity" can have broad meaning, incorporating changes in operating condition, changes in system disturbances, and nonlinear elements in the system (such as a freeplay and rate limits). Here, the term "nonlinearity" will only refer to systems with nonlinear elements. Changes in operating

condition and changes in disturbance signals will be referred to as a "time-variation" of the system and disturbances, respectively. While changes in operating condition may be explainable via further evaluation of experimental data; initially, in the context of FRE, the system will appear to change with time.

Results for analytical expressions of expected estimation error are summarized in Section 3.1; these results provide valuable insights into the estimation error that will be used throughout the chapter. Section 3.1.1 presents results for spectra estimation with random signals as input; Section 3.1.2 modifies those results for use with sparse frequency transforms. Section 3.1.3 further modifies the results presented for random sparse spectra to be limited to sparse spectra in the presence of only periodic inputs. The approaches throughout Section 3.1 maintain key assumptions for system linearity and time variance.

Estimation of disturbances will be related directly to the estimation error analysis for periodic signals, leading to a significant component of estimation uncertainty in Section 3.1.3. The concept of spectra in the null frequency set, introduced in Chapter 2, is critical to isolating the disturbance signal in the presence of excitation. Spectral leakage is a fundamental consequence of approximating continuous functions with finite, discrete time-series for use in spectral estimation. Leakage is addressed in Section 3.2.2 along with a novel diagnostic metric for use in both uncertainty quantification and mitigation through selection of appropriate excitation parameters and window functions. A unique approach to addressing time-variance is introduced in Section 3.2.3 as arising from both system transients and changes in the disturbance signal. The different sources of uncertainty in the estimates are combined in Section 3.3 to establish a total estimate uncertainty.

As discussed, the systems depicted in Figure 1.1 are assumed to be linear; an additional requirement for linearity will arise in Chapter 4 for defining system stability. Nonlinearities in the systems are discussed in Section 3.4, where describing functions (DF) are presented to generalize the impacts of nonlinearities and provide guidance for refinement of the excitation. An example of a nonlinear servo mechanism is also presented in Section 3.4. The servo example is used to illustrate the influence of nonlinearities on the FRE process, as well as form the basis for an example of excitation refinement in Section 3.5.

Finally, the MIMO example of Section 2.4 is developed further to address the estimate uncertainty in Section 3.6.

3.1 Spectra Estimation Error Analysis

Spectral estimation is often used in the presence of random input signals, which result in random output signals. Results of error analysis for spectral estimation with random signals are presented in Section 3.1.1; these results are derived in Bendat [1] and Pintelon [2] and are simply repeated here. Multisine excitations have a significant impact on the FRE error analysis. Multisines are relatively sparse in frequency (the number of frequencies in the excitations is much less than the number of samples), which allows for the full content of the multisine to be evaluated with a sparse DFT, as discussed in Chapter 2. Multisines are also nonrandom and periodic, which further simplifies the spectral error analysis; the error analysis for multisines is derived in Pintelon [2] and is simply repeated here. Implications of using multisine excitation on the error analysis will be addressed in Section 3.1.2 and Section 3.1.3.

Error of the rough spectra estimates, $\tilde{\Phi}(\omega)$ will be captured in terms of a errors associated with random variation and bias with respect to the know spectra, $\Phi(\omega)$. The relative random error, ε_r, and relative bias error, ε_b, are defined in terms of the variance and bias in Equation (3.1) and Equation (3.2); notation indicating the dependence of the spectra on frequency, ω, has been dropped.

$$\varepsilon_r[\tilde{\Phi}] := \frac{\sigma[\tilde{\Phi}]}{\Phi} = \frac{\sqrt{\mathrm{Var}[\tilde{\Phi}]}}{\Phi} \tag{3.1}$$

$$\varepsilon_b[\tilde{\Phi}] := \frac{\mathrm{b}[\tilde{\Phi}]}{\Phi} \tag{3.2}$$

Bias and variance are combined to form the total (root-mean-square) relative error, Equation (3.3)

$$\varepsilon[\tilde{\Phi}] := \frac{\sqrt{\sigma^2[\tilde{\Phi}] + \mathrm{b}^2[\tilde{\Phi}]}}{\Phi} = \sqrt{\varepsilon_r^2[\tilde{\Phi}] + \varepsilon_b^2[\tilde{\Phi}]} \tag{3.3}$$

Relative error of the smooth spectra estimates are denoted $\varepsilon_r[\hat{\Phi}]$, $\varepsilon_b[\hat{\Phi}]$, and $\varepsilon[\hat{\Phi}]$ for

the random, bias, and total relative error.

The derivations for the random error analysis are based on a Taylor series expansion of the auto-spectra and cross-spectra; Equation (3.4).

$$\varepsilon_r[\tilde{\Phi}_{uu}] = \frac{\sqrt{\text{Var}[\tilde{\Phi}_{uu}]}}{\tilde{\Phi}_{uu}}$$

$$\varepsilon_r[\tilde{\Phi}_{zz}] = \frac{\sqrt{\text{Var}[\tilde{\Phi}_{zz}]}}{\tilde{\Phi}_{zz}} \tag{3.4}$$

$$\varepsilon_r[\tilde{\Phi}_{u\to z}] = \frac{\sqrt{\text{Var}[\tilde{\Phi}_{u\to z}]}}{\tilde{\Phi}_{u\to z}}$$

The auto-spectra and cross-spectra relative error are written in terms of the DFT of the time-series; recall that for a time segment $\tilde{U}$ is the DFT of u and $\tilde{Z}$ is the DFT of z. Equation (3.4) is used as the basis for the results in the following sections. The FRE approach here assumes that the input time-series u is known exactly, in which case Equation (3.4) significantly simplifies; this result is addressed specifically in Section 3.1.3. The Taylor expansion and error propagation for the FRF follows from the auto and cross-spectra errors, Section 3.1.3 will address both the simplification for use with known multisine excitations and expansion to the FRF.

3.1.1   Results for Random Signals

A common approach to determine estimation error assumes random signals and a full resolution DFT to produce spectra estimates. This approach follows the results obtained by Bendat [1]. The full resolution DFT has frequencies for the transformation, ω_m, spanning the range from zero to the sampling frequency in increments of $\Delta\omega = \frac{2\pi}{N\Delta t}$ (in practice, for real-valued time-series, the frequencies are limited by the Nyquist frequency).

The relative random estimation error, $\varepsilon_r[\tilde{\Phi}]$, of the resulting auto-spectra yields a succinct approximation derived in [1] as Equation (3.5); wherein frequency resolution, $\Delta\omega$, is established by the number of samples in the segmented time-series, N_s.

$$\varepsilon_r[\tilde{\Phi}] \approx \sqrt{\frac{2\pi}{\Delta\omega \ T_s}}$$

$$\text{Where: } \Delta\omega \approx \frac{2\pi}{N_s\Delta t} = \frac{2\pi}{T_s} \tag{3.5}$$

It is easy to see from Equation (3.5), that in this case the random error of the spectra estimate, $\varepsilon_r[\tilde{\Phi}]$, is unity; indicating that the variance is of the same magnitude as the expected value.

To approximate the bias error, the approach from Bendat [1] is followed, wherein a particular response model is assumed. For concreteness, consider the special case of a second-order system $B(s) = \frac{\omega_n^2}{s^2+2\zeta\omega_n s+\omega_n^2}$ with natural frequency, ω_n, and damping ratio, ζ. The bias error for this second-order system can be approximated with $\omega_r = \omega_n\sqrt{1-\zeta^2}$ for $0 \leq \zeta \leq 1$ or simply as $\omega_r \approx \omega_n$ for $\zeta \ll 1$. The relative bias error is defined in Equation (3.6) along with an approximation based on model parameters, ω_n and ζ, and a rectangular window function [1].

$$\varepsilon_b[\tilde{\Phi}] \approx -\frac{1}{3}\left(\frac{\Delta\omega}{2\pi \ |B_r|}\right)^2 \approx -\frac{1}{3}\left(\frac{\pi}{N_s\Delta t\zeta\omega_n}\right)^2$$

$$\text{Where: } |B_r| \approx \frac{\zeta\omega_n}{\pi} \tag{3.6}$$

The relative estimation error bias depends on the frequency resolution, $\Delta\omega$. For a lightly damped system, which produced the largest bias error, the gain factor at the resonance frequency is approximated as: $B_r = |B(\omega_r)|$ in Equation (3.6). The bias error is representative of a low damped response that is "missed" by the frequencies in the spectra estimate; as evident by inspection of Equation (3.6) as $\zeta \to 0$ then $\varepsilon_b \to \infty$. The negative sign in Equation (3.6) is a result of the particular assumed model; low damping of that model results in peaks in the response, a similar second-order model can be constructed, with troughs rather than peaks, in which case the bias overestimates the spectra at the troughs.

The ensemble of rough spectra estimates are combined to produce smooth spectra estimates. Continuing with the assumption that each of the L segments represents a unique sample of a signal, both the random and bias errors are reduced as $\propto \frac{1}{\sqrt{L}}$ [1], Equation (3.7).

$$\varepsilon_r[\hat{\Phi}] \approx \frac{1}{\sqrt{L}}\varepsilon_r[\tilde{\Phi}] = \frac{1}{\sqrt{L}}$$

$$\varepsilon_b[\hat{\Phi}] \approx \frac{1}{\sqrt{L}}\varepsilon_b[\tilde{\Phi}] = -\frac{1}{3\sqrt{L}}\left(\frac{\pi}{N_s \Delta t \zeta \omega_n}\right)^2$$

(3.7)

The result of Equation (3.7) requires that the underlying signal is a wide-sense stationary random signal; further, the ensemble mean requires the underlying signal is ergodic. This result is the familiar Central Limit Theorem for sampled means. The requirement for wide-sense stationary random signals, and the potential for misapplying this assumption, will be partially addressed by accounting for time-variations in the FRE results on a segment-by-segment basis.

The random error variance is reduced by segmentation and merging the segmented results into a smooth estimate. The smoothed bias error has a trade-off between achievable DFT resolution, $\Delta\omega$, and the number of segments, L, to achieve an accuracy, ε_b. This trade-off stems from the DFT performing a full resolution transform; with $\Delta\omega = \frac{2\pi}{N_s \Delta t}$.

3.1.2 Results for Random Signals with Sparse Spectra

The spectral estimation method described herein, specifically using sparse DFT spectra estimation coupled with multisine excitations, alters the error analysis results obtained previously. This distinction is highlighted by redefining the frequency resolution to Equation (3.8); where ω_{min} is the minimum frequency in the excitation, $\Delta\omega$ is the frequency spacing, and the cth excitation channel has M_c frequencies.

$$\text{Let: } \omega_m = \omega_{min} + m\ \Delta\omega \qquad m = \{0, 1, ..., M_c\} \tag{3.8}$$

It is evident that there is no advantage to further narrowing the estimation resolution, all signal content occurs at the excitation frequencies. For use with multisine excitations, a natural approach is to segment the time-series into integer multiples of the longest excitation period; such that: $N_s = R\frac{2\pi}{\Delta t\ \omega_{min}}$ where R is an integer number of excitation repetitions in each of the L segments. The rough spectra error estimates follow from redefining the DFT frequencies to match the excitation frequencies, Equation (3.9).

$$\varepsilon_r[\tilde{\Phi}] \approx \sqrt{\frac{\omega_{min}}{R \ \Delta\omega}} \tag{3.9}$$

The relative error bias for the rough spectra, $\varepsilon_b[\tilde{\Phi}]$, is again based on "missing" frequencies and requires specification of a simple second-order system (analogous to Equation (3.6)), Equation (3.10).

$$\varepsilon_b[\tilde{\Phi}] \approx \frac{-1}{3}\left(\frac{\Delta\omega}{2\zeta\omega_n}\right)^2 \tag{3.10}$$

The bias error is again dependent upon the system characteristics, with the possibility that $\varepsilon_b \to \infty$; because the potential for $\zeta \to 0$ is unavoidable. The rough bias error, $\varepsilon_b[\tilde{\Phi}]$, also indicates that the spectra are underestimated (though redefining the second-order system would result in overestimating the spectra).

The resulting smooth spectra random error estimate, $\varepsilon_r[\hat{\Phi}]$ in Equation (3.11), is a function of the ratio $\frac{\omega_{min}}{\Delta\omega}$ and the total number of repetitions of the excitation, LR.

$$\varepsilon_r[\hat{\Phi}] \approx \frac{1}{\sqrt{L}}\varepsilon_r[\tilde{\Phi}] = \sqrt{\frac{\omega_{min}}{LR\Delta\omega}} \tag{3.11}$$

Mitigation of random estimation error is addressed through specification of the excitation frequencies (via parameters ω_{min} and $\Delta\omega$) and the total duration of the estimate.

The resulting smooth spectra bias error, $\varepsilon_b[\hat{\Phi}]$ in Equation (3.12), still shows a strong dependence on the excitation frequency spacing, $\propto (\Delta\omega)^2$, and a weaker dependence on the number of segments, $\propto \frac{1}{\sqrt{L}}$.

$$\varepsilon_b[\hat{\Phi}] \approx \frac{1}{\sqrt{L}}\varepsilon_b[\tilde{\Phi}] = \frac{-1}{3\sqrt{L}}\left(\frac{\Delta\omega}{2\zeta\omega_r}\right)^2 \tag{3.12}$$

When the DFT is performed on a sparse grid with random inputs, the potential bias error is much higher than with a full resolution DFT. As noted earlier, the bias error is influenced by the window function side-lobe magnitude; therefore, the mitigation approach to address spectral leakage will also partially address estimation bias error. However, the "missed" condition also arises as a consequence of interpolation. Interpolation is used in the FRE to expand the SIMO estimates to MIMO estimates and changing the disturbance spectra estimations from the null frequencies to the excitation

frequency basis.

To gain further insight into the bias error, a critical damping ratio is defined in Equation (3.13) such that if $\zeta = \zeta_{crit}$ then $|\varepsilon_b| = |\varepsilon_r|$; the magnitude of the bias and random error are the same.

$$\zeta_{crit} = \frac{1}{3} \left(\frac{\Delta\omega}{2\omega_r} \right)^2 \sqrt{\frac{R\Delta\omega}{\omega_{min}}} \tag{3.13}$$

For $\zeta < \zeta_{crit}$ the bias error becomes dominant. The worst-case condition for ζ_{crit} occurs at the minimum interpolated frequency in the FRE, so ω_r in Equation (3.13) is small. For the purpose of simplifying the critical damping equation, the lowest interpolated frequency is taken as the minimum frequency itself: $\omega_r \approx \omega_{min}$. Equation (3.13) then yields Equation (3.14).

$$\zeta_{crit} \approx \frac{\sqrt{R}}{12} \left(\frac{\Delta\omega}{\omega_{min}} \right)^{2.5} \tag{3.14}$$

The relative importance of the ratio of frequency step and minimum frequency is again apparent.

For $\zeta > \zeta_{crit}$ the upper bound for the RMS error is derived by substituting ζ_{crit} from Equation (3.14) into Equation (3.3) (with Equation (3.11) and Equation (3.12) for the random and bias terms). The resulting inequality for the RMS error provides a simple statement for the relative error upper bound, Equation (3.15).

$$\varepsilon < \sqrt{\frac{2\,\omega_{min}}{LR\Delta\omega}} \tag{3.15}$$

Note that all the terms in Equation (3.14) and Equation (3.15) are established by the excitation definition; as such, uncertainty due to this component of the estimation error can be bounded prior to estimating the frequency response.

In the particular case of a single repeat of the excitation, $R = 1$, and the base frequency of the harmonics is the minimum excitation frequency, $\Delta\omega = \omega_{min}$, the critical damping ratio is $1/12$ or 8.3%. Thus, for any system with a damping ratio greater than 8.3%, it can be expected that the random error will be larger than the bias error.

3.1.3 Results for Periodic Signals

Section 3.1.2 provided an analysis of the expected relative estimation error when using random signals and a sparse frequency DFT. The multisine excitations are nonrandom and periodic. The error analysis for such systems with periodic inputs and randomly disturbed output measurements is derived in Pintelon [2]. The derivation starts as a Taylor series expansion of the rough auto-spectra and cross-spectra in Equation (3.4).

 With the condition that input to the plant, u, is periodic and free from measurement noise, the DFT of u contains zero variance from the true value; $E[\tilde{U}] = U$ and $Var[\tilde{U}] = 0$. Further, since the variance of the system input is zero, any covariance with the system input will also be zero; $Cov[\tilde{U}^*, \tilde{Z}] = 0$. The relative uncertainty for the input is zero; $\varepsilon_r[\tilde{\Phi}_{uu}] = 0$. Via the Taylor expansion Equation (3.4) simplifies to Equation (3.16).

$$\varepsilon_r[\tilde{\Phi}_{u \to z}] = \frac{1}{2}\varepsilon_r[\tilde{\Phi}_{zz}] = \frac{1}{2}\frac{\sqrt{Var[\tilde{\Phi}_{zz}]}}{\tilde{\Phi}_{zz}} \tag{3.16}$$

 The error due to randomness in z resulting in the cross-spectra error, $\varepsilon_r[\tilde{\Phi}_{u \to z}]$, is simply half the auto-spectra error $\varepsilon_r[\tilde{\Phi}_{zz}]$. Following with the same assumption on u (periodic and non-random), the cross-spectra and FRF are unbiased [2]. The cross-spectra random error and FRF random error are also identical (this is not the case if $Var[\Phi_{uu}] \neq 0$).

$$\varepsilon_r[\hat{\Theta}_{u \to z}] = \varepsilon_r[\hat{\Phi}_{u \to z}] \tag{3.17}$$

 The smoothed spectra and FRF contain the same relations as in prior cases; repeated here as Equation (3.18).

$$\begin{aligned} \varepsilon_r[\hat{\Phi}] &\approx \frac{1}{\sqrt{L}}\varepsilon_r[\tilde{\Phi}] \\ \varepsilon_r[\hat{\Theta}] &\approx \frac{1}{\sqrt{L}}\varepsilon_r[\tilde{\Theta}] \end{aligned} \tag{3.18}$$

 The cross-spectra and FRF are unbiased; however, they are evaluated on a finite frequency basis. The approach to error bias associated with "missed" modes in the spectra and frequency from Section 3.1.2 is appropriate.

3.2 Uncertainty Sources

The FRF estimate is composed of a "nominal" component and an "uncertain" component in an additive model; Equation (3.19).

$$\hat{G}[\Omega_E] := \bar{G}[\Omega_E] + \Delta \circ \dot{G}[\Omega_E] \tag{3.19}$$

A complex-valued perturbation matrix Δ is introduced in Equation (3.19) to allow the uncertainty to influence the nominal estimate to produce a range of complex-valued estimates.

The nominal estimate, $\bar{G}$, is produced from rough estimates of the FRF, $\tilde{\Theta}_{u \to z}$. The operator for the expected value over L rough segments is depicted as $\mathrm{E}_L[\ ]$ in Equation (3.20).

$$\bar{G}[\Omega_E] := \mathrm{E}_L[\tilde{\Theta}_{u \to z}[\Omega_E]] = \mathrm{E}_L[\frac{\tilde{\Phi}_{u \to z}[\Omega_E]}{\tilde{\Phi}_{uu}[\Omega_E]}] \tag{3.20}$$

The nominal estimate has been expanded to depict the FRF as rough cross-spectra, $\tilde{\Phi}_{u \to z}$, with respect to input auto-spectra, $\tilde{\Phi}_{uu}$.

The uncertain component of the FRF is depicted in Equation (3.21) as the expected value of rough uncertain components.

$$\dot{G}[\Omega_E] := \mathrm{E}_L[\dot{\Theta}_{u \to z}[\Omega_E]] = \mathrm{E}_L\left[\frac{\sqrt{\mathrm{Var}[\tilde{\Phi}_{u \to z}[\Omega_E]]}}{\tilde{\Phi}_{uu}[\Omega_E]}\right] \tag{3.21}$$

The uncertain estimate has been expanded to depict the cross-spectra variance, $\mathrm{Var}[\tilde{\Phi}_{u \to z}]$, with respect to input auto-spectra, $\tilde{\Phi}_{uu}$. The variance is estimated for each of the rough spectra; the $\mathrm{Var}[\ ]$ operator in Equation (3.21) is not taken over the L rough estimates, it is variance within the rough estimates. An estimate of the variance term will be provided in Section 3.2.1 and then modified in Section 3.2.2.

3.2.1 Uncertainty due to Disturbance Signals

Disturbances introduce a significant source of estimation uncertainty. The variance term in Equation (3.21) can be estimated via evaluation of z in the null frequency set. The variance of $\tilde{\Phi}_{zz}[\Omega_E]$ can be determined from the magnitude of the disturbance

auto-spectra. This is a result of Parseval's Theorem, Appendix A.4, and the commutative property of the variance operator in spectra analysis. The estimation random uncertainty due to disturbance can then be expressed as Equation (3.22).

$$\text{Var}[\tilde{\Phi}_{zz}[\Omega_E]] \approx \tilde{\Phi}_{nn}[\Omega_E] \tag{3.22}$$

In the null frequencies, all the spectral power is contained within z (u in the null is zero) thus $\tilde{\Phi}_{nn}$ has twice the spectral power of $\tilde{\Phi}_{u \to n}$. This can also be shown via a Taylor expansion of the cross-spectra and auto-spectra.

In Chapter 2 it was shown that the magnitude of the disturbance PSD, $\tilde{\Phi}_{nn}$, can be estimated from the output time-series z.

The rough FRF uncertainty due to disturbances is then estimated with the estimated FRF, $\grave{\Theta}_d[\Omega_E]$ in Equation (3.23).

$$\grave{\Theta}_d[\Omega_E] \mathrel{\hat{=}} \sqrt{\frac{\tilde{\Phi}_{nn}[\Omega_E]}{\tilde{\Phi}_{uu}[\Omega_E]}} \tag{3.23}$$

3.2.2   Uncertainty due to Spectral Leakage

Spectral leakage is a direct result of performing a time-frequency transformation with finite time-series, specifically it is due to discontinuities at the end points. Spectral leakage, and time-series window functions as the common mitigation, are discussed at length in [35] and [36]; and for similar applications in [34]. It will be shown that a simple metric can quantify the magnitude of leakage, as well as the inherent accuracy limitations of the spectral estimate, and provides useful guidance for excitation definition and spectral analysis.

Excitation Leakage

Recall that the multisine excitations introduced in Section 2.1 are mutually orthogonal, and the excitation frequency set is orthogonal to the null frequency set. Estimation of the excitation spectrum at the null frequencies should be exactly zero by construction of the excitation, hence any spectral power estimated at the null frequencies of the excitation contributes to the estimation error. Corresponding leakage errors are present in the spectral estimation of any signal in the system. The leakage error can thus be

independently estimated and accounted in the final estimate. The following approach will also expose any errors associated with the inherent accuracy limitations of spectral analysis [37, 38].

Evaluation of the null-to-excitation ratio, $\tilde{\eta}$ in Equation (3.24), is somewhat analogous to the noise-to-signal ratio, $\tilde{\beta}$, and provides a useful metric to quantify spectral leakage and underlying spectral estimate accuracy.

$$\tilde{\eta}[\Omega_E] = \frac{\tilde{\Phi}_{uu}[\Omega_N]|_{\Omega_E}}{\tilde{\Phi}_{uu}[\Omega_E]} \tag{3.24}$$

The spectral power estimated in the null frequencies is normalized by the excitation spectral power at each frequency, thus $\hat{\eta}_{leakage} \leq 1$ for all frequencies. The excitation auto-spectrum is evaluated independently at both the excitation frequencies, $\hat{\Phi}_{uu}(\Omega_E)$, and at the null frequencies, $\hat{\Phi}_{uu}(\Omega_N)$. The null-to-excitation ratio can be estimated with rough estimates or with smooth estimates (replace ˜ with ˆ in Equation (3.24)).

The null-to-excitation ratio can also be defined as a scalar leakage metric by simply taking the expected values, Equation (3.25).

$$\hat{\Theta}_{leakage} = \frac{\mathrm{E}[\hat{\Phi}_{uu}(\Omega_N)]}{\mathrm{E}[\hat{\Phi}_{uu}(\Omega_E)]} \tag{3.25}$$

The leakage assessment as described is sufficient for multisine excitations and should be performed during excitation definition. The particular application of signal leakage of interest here is the disturbance signal power, as estimated via $\tilde{\Phi}_{zz}[\Omega_N]$, leaking into the estimate of output signal power, $\tilde{\Phi}_{zz}[\Omega_E]$.

Time-series window functions are typically employed with finite time-series to smooth the discontinuities at the start and end of the finite series. Unfortunately, there is not a simple parameterization that captures the trade-offs between sources of leakage in terms of window functions; a detailed treatment of window functions is provided in [35]. In order to provide guidance, three window functions have been approximated, Table 3.1, that represent commonly employed functions.

Table 3.1:   Spectral window function approximations of side-lobe maxima.

Window	Approx Equation	Parameter Values		Min Bin
Rectangular (Dirichlet)	$\lvert W \rvert = 10^a\ b^s$	$a = $ -0.51	$s = $ -0.98	0.58
Triangular (Bartlett)	$\lvert W \rvert = 10^a\ b^s$	$a = $ -0.43	$s = $ -1.95	1.19
Hann	$\lvert W \rvert = 10^a\ b^s$	$a = $ -0.41	$s = $ -3.12	1.72

The approximation functions have the same underlying equation, $\lvert W \rvert = 10^a b^s$ where b is a bin number, $\lvert W \rvert$ is relative power magnitude, and parameters a and s were determined from curve fits of the window function local maxima. The approximations intersect the main-lobe of the window spectrum at the "Min Bin" width of Table 3.1. The functions and approximations relate the spectral power of the window function to the frequency bin width; the bin widths are then dimensionalized as a relation of frequencies, Equation (3.26).

$$\Delta \omega_{bin} = \frac{2\ \omega_{min}}{R} \tag{3.26}$$

The window spectrum and associated approximations are shown in Figure 3.1.
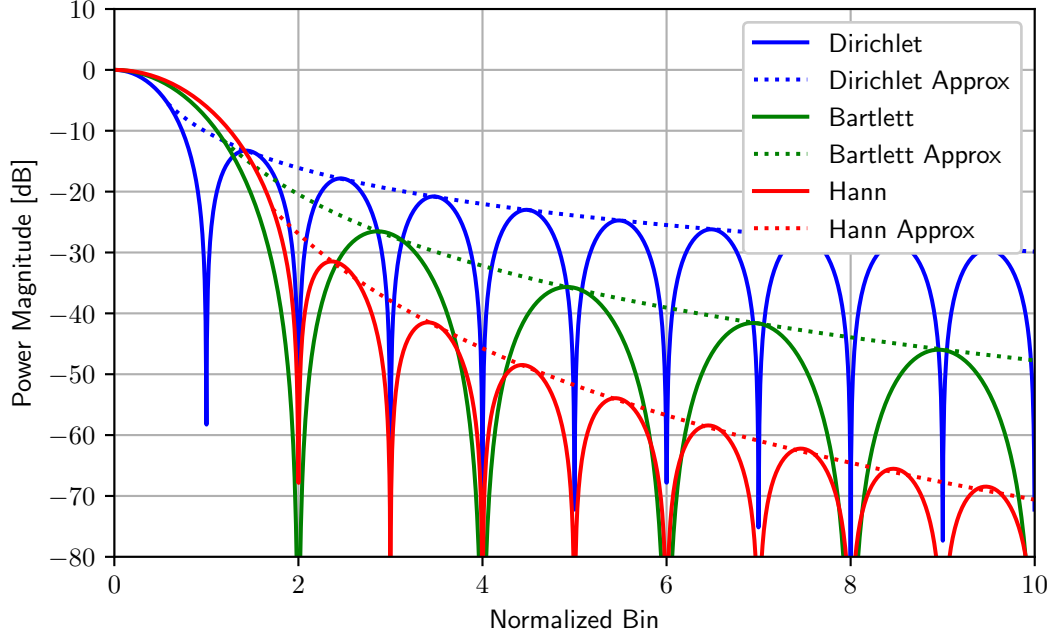
Figure 3.1: Magnitude of spectral window functions and approximation of side-lobe maxima.

The window function approximations capture the peaks of the magnitudes of the side-lobes of the window spectrum and are monotonically decaying. The definition of bins follows from [35], where the width of each bin is a normalization of the frequency basis in terms of parameters amenable to the excitation definition, Equation (3.26), where R is the number of repeated cycles of the lowest frequency in the excitation.

The window function also manifests in the time-domain, with a corresponding time duration of each bin, Δt_{bin} in Equation (3.27).

$$\Delta t_{bin} = \frac{4\pi}{\Delta\omega} \tag{3.27}$$

An excitation is defined with a single channel and frequency spacing of 0.2 Hz. The frequency set for the excitation and null are listed in Equation (3.28).

$$\Omega_E = \Omega_1 = 2\pi \; \{0.05, \; 0.15, \; \ldots, \; 9.85, \; 9.95\}$$
$$\Omega_N = 2\pi \; \{0.10, \; 0.20, \; 0.30, \; \ldots, \; 9.80, \; 9.90\} \tag{3.28}$$

A leakage target threshold is specified with a desire for leakage to be less than 10% (-20 dB). Application of the inverse of the Dirichlet approximation, from Table 3.1, yields that at least 3.15 bins are required to provide less than 10% leakage between the excitation frequency components. Application of Equation (3.27) specifies that the time duration of each bin is 10 seconds. Therefor, the excitation must be at least 31.5 seconds in duration. The period of the lowest frequency in the excitation is 20 seconds, application of Equation (3.26) specifies the number of repetitions of the excitation, $R = 2$. Hence, the excitation will have 2 cycles with the lowest frequency of 0.05 Hz; for a total excitation duration of 40 seconds.

Spectral leakage for the described excitation is computed for each instant in time and presented in the time-domain Figure 3.2.
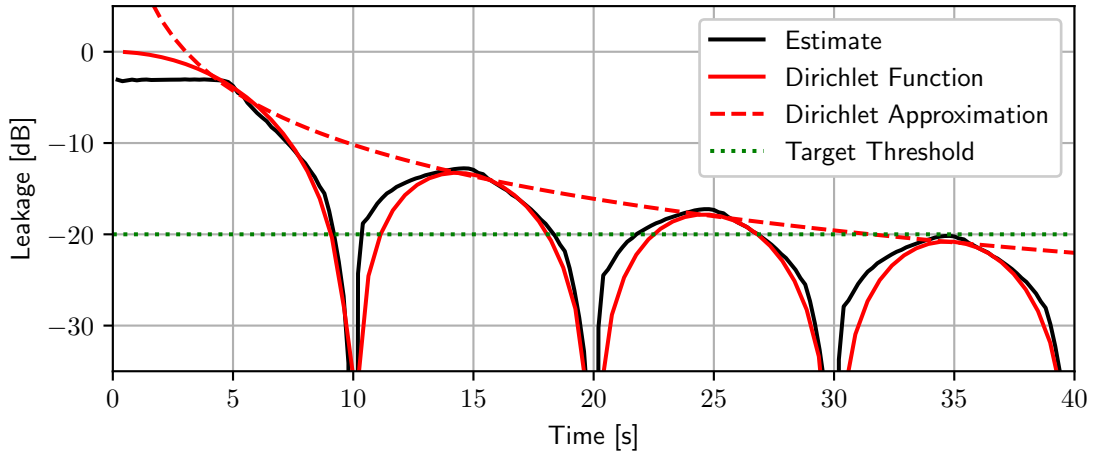
Figure 3.2: Time history of spectral leakage as estimated from a time-series, ideal Dirichlet function, an approximation of the Dirichlet function, and the desired leakage threshold.

The leakage estimate is computed, as $\Theta_{leakage}$ from Equation (3.25), with the excitation time-series at each time instance; the estimation at each time instance is computed for a truncated excitation time-series. After an initial startup transient (t < 5.0 s), the excitation-to-null metric follows the Dirichlet function. The Dirichlet approximation provides a smooth, monotonically decaying upper bound for the magnitude of leakage. Periodicity of the leakage is evident, resulting in negligible leakage at intervals of the time bin duration; every 10 seconds. The target threshold is achieved at approximately

31.5 seconds, corresponding to 3.15 bins required to achieve the desired threshold.

Similar results can be attained with the Bartlett and Hann windows; for comparison, the excitation defined above would yield 4% leakage with a Bartlett window, and 1.1% with a Hann window.

Output Leakage

The preceding focused on leakage detection with the excitation signal it The output signals in general will be composed of a combination of periodic signals, as in the input, and random data originating from disturbances. Excitations are periodic with negligible leakage at intervals of Δt_{bin}, the same is true for any periodic signal. So, the periodic component of the output signal will also have negligible leakage at intervals of Δt_{bin}. Hence, at intervals of Δt_{bin} only the non-periodic component of the output signal will be subject to leakage.

In practice, excitations are defined to have integer multiples of Δt_{bin}. The FRF uncertainty due to leakage, $\dot{\Theta}_w$ in Equation (3.29), is then simply the approximate window function scaled by the uncertainty due to disturbances, $\dot{\Theta}_d$ from Equation (3.23).

$$\dot{\Theta}_w[\Omega_E] = |W| \, \dot{\Theta}_d[\Omega_E] \tag{3.29}$$

The approximate window function, $|W|$ is computed from Table 3.1 for the appropriate window function and number of bins in the time-series.

Spectral leakage also addresses the spectral estimate bias error that is associated with potentially "missed" frequencies with low damping, as discussed in Section 3.1. For mitigation of bias error, some leakage may be desirable to allow narrowband power (low damping modes) to leak into neighboring frequency bins and aid in observability.

3.2.3 Uncertainty due to Time-Variance

The frequency response estimation of Chapter 2, and later the stability definition in Chapter 4, are predicated on systems and signals being time-invariant. Two principal sources of time variance are addressed, although the general approach is generic. First, the spectral estimation presented in Chapter 2 is strictly valid only for systems in harmonic steady-state (forced response), thus system transients occurring as the free

response of the system result in estimation error [39, 34]. If estimating the spectra via a DFT, the steady-state assumption arises due to the Fourier Transform being performed only along $s = j\omega$. If estimating the spectra via a CZT, the steady-state assumption arises due to the CZT being performed only along a spiral in the z-coordinates. Common practice for mitigating the impact of system transients is to apply a window function that de-emphasizes the initial response; since the intent of windowing is to smooth the discontinuities, nearly all window functions will provide some transient mitigation. Another common mitigation strategy is to provide excitations sufficient to overwhelm the impact of transients. Since the excitation generally contains multiples of the lowest frequency of interest, and the free-response frequency is likely higher in frequency, the diminishing contribution of the free-response is assured; although quantification is not apparent. The second predominant source of time-variance is the exogenous disturbance, n, introduced in Figure 2.1. Prior analysis has assumed that the disturbance is at least weak-sense stationary; since the signal serves as a generalized entry point for disturbances, the validity of that assumption should be tested.

As discussed in Chapter 2 the spectral estimation approach is to segment the time-series, perform FRE on each segment, and merge the segmented FREs into a single estimate. Each segmented time-series is treated as an independent and identically distributed (IID) realization of the underlying signal, as discussed in Section 3.1. As with window functions in general, there are numerous methods for segmenting and windowing [35]. Bartlett's method uses rectangular windows on each segment, with no overlap between successive time-series segments (as in the smooth error estimations of Equation (3.11)). Welch's method uses Hann windows on each segment with 50 % overlap between successive segments (the overlapping portion of the segments are not strictly IID and a correction factor is applied [7]). It must be noted that by using shorter segments, the timescale for detecting and quantifying time variance is reduced by a factor $\propto L^{-1}$; the rough FRE instances are still subject to time-variance.

The typical construct required for the analysis of multi-window methods will be used to expose time variations in the estimates. Additional processing steps could be applied to explicitly test the time-invariance hypothesis and eliminate segments from the ensemble. A simple method of merging the segments could also employ an inverse-variance weighted mean to take the ensemble mean.

The expected value of the combined ensemble, $\bar{\Phi}$, is taken as a simple mean of the ensemble estimates, Equation (3.30).

$$\bar{\Phi} := \mathrm{E}_L[\tilde{\Phi}_l] \approx \frac{1}{L} \sum_{l=1}^{L} \tilde{\Phi}_l \qquad (3.30)$$

The variance of the rough spectra ensemble, $\mathrm{Var}_L[\hat{\Phi}[\Omega_E]]$ in Equation (3.31), indicates the magnitude of the time-variance of the estimation; this is distinct from the variance of the rough spectra estimates themselves.

$$\mathrm{Var}_L[\hat{\Phi}[\Omega_E]] := \mathrm{E}_L[(\tilde{\Phi}_l[\Omega_E] - \bar{\Phi}[\Omega_E])^2] \approx \frac{1}{L} \sum_{l=1}^{L} (\tilde{\Phi}_l[\Omega_E] - \bar{\Phi}[\Omega_E])^2 \qquad (3.31)$$

The estimation of time-variance is partitioned into the excitation and null frequency sets. The rough spectra variances at the excited frequencies of z indicates time-variance arising in either the disturbance or in the system itself; rough spectra variance in the null frequencies is limited to the time-variance in the disturbance, $\mathrm{Var}[\hat{\Phi}[\Omega_N]]$ in Equation (3.32).

$$\mathrm{Var}_L[\hat{\Phi}[\Omega_N]] := \mathrm{E}_L[(\tilde{\Phi}_l[\Omega_N]|_{\Omega_E} - \bar{\Phi}[\Omega_N])^2] \approx \frac{1}{L} \sum_{l=1}^{L} (\tilde{\Phi}_l[\Omega_N]|_{\omega_E} - \bar{\Phi}[\Omega_E])^2 \qquad (3.32)$$

Relative error associated with time-variance is defined as $\hat{\varepsilon}_t[\Phi_{zz}]$ in Equation (3.33).

$$\hat{\varepsilon}_t[\Phi_{zz}[\Omega_E]] = \frac{\sqrt{\mathrm{Var}_L[\tilde{\Phi}_{zz}[\Omega_E]]}}{\bar{\Phi}_{zz}[\Omega_E]} \qquad (3.33)$$

The variance is normalized by the input spectra; this is convenient in order to later combine each of the error contributions to form a total error estimate.

3.3   Total Uncertainty and Propagation

The prior section provided the quantification of uncertainty for three distinct uncertainty sources; disturbance, spectral leakage, and time-variance. Here, those sources

are combined to provide a total uncertainty estimate.

Uncertainty due to disturbance on the system output, captured in the null of the signal z, is depicted as $\grave{\Theta}_d$ in Equation (3.34).

$$\grave{\Theta}_d[\Omega_E] \mathrel{\hat{=}} \sqrt{\frac{\tilde{\Phi}_{nn}[\Omega_E]}{\tilde{\Phi}_{uu}[\Omega_E]}} \mathrel{\hat{=}} \sqrt{\frac{\tilde{\Phi}_{zz}[\Omega_N]|_{\Omega_E}}{\tilde{\Phi}_{uu}[\Omega_E]}} \tag{3.34}$$

As mentioned earlier, while the disturbance signal itself is unknown, the magnitude of its spectra can be estimated from z. The system has been modeled with a single exogenous disturbance, n, however Equation (3.34) captures all signal content in the null frequencies and attributes it to uncertainty. If an input disturbance were modeled at the plant input, such as $z = n + G(s)(u + r)$ where r is a GWN, the contribution in the null would be due to $n + G(s)r$.

Uncertainty due to spectral leakage can usually be adequately avoided through proper excitation definition and window function selection. The uncertainty due to leakage can also be easily approximated.

The FRF estimation uncertainty associated with spectral leakage relies upon the approximations of the window functions from Table 3.1, and is given as $\tilde{\varepsilon}_w$ in Equation (3.35).

$$\grave{\Theta}_w[\Omega_E] = |W| \, \grave{\Theta}_d[\Omega_E] \tag{3.35}$$

The rough FRF estimate uncertainty combines the uncertainty due to disturbances and leakage; each rough FRF uncertainty estimate, denoted for the lth segment as $\grave{\Theta}_l$ in Equation (3.36).

$$\grave{\Theta}_l[\Omega_E] = (1 + |W|) \, \grave{\Theta}_d[\Omega_E] \tag{3.36}$$

The variance of the L samples of rough estimates is the basis for estimating the contribution of the time-variance to estimation uncertainty. For capturing sources of estimation uncertainty, it is convenient to evaluate the variance of the rough spectra of the measured output z at the excitation frequencies, Equation (3.37).

$$\varepsilon_t = \hat{\varepsilon}_t[\Phi_{zz}[\Omega_E]] \tag{3.37}$$

The smooth FRF estimate uncertainty for L rough estimates combines Equation (3.36) and Equation (3.37) as $\grave{\Theta}_{u\rightarrow z}[\Omega_E]$ in Equation (3.38).

$$\grave{G}[\Omega_E] \doteq \grave{\Theta}_{u\rightarrow z}[\Omega_E] = \left[(1 - \frac{1}{\sqrt{L}})\varepsilon_t + \frac{1}{\sqrt{L}}\right] \; \mathrm{E}_L[\grave{\Theta}_l[\Omega_E]] \tag{3.38}$$

The form of Equation (3.38) indicates that if the response is time-invariant, $\hat{\varepsilon}_t = 0$, then the smooth estimate tends: $\grave{\Theta}_{u\rightarrow z} \rightarrow \frac{1}{\sqrt{L}}\mathrm{E}_L[\grave{\Theta}_l]$. If the response has rough estimates with variance on the order of the expected value, $\hat{\varepsilon}_t = 1$, the smooth estimates tend to the expected value of the rough estimates: $\grave{\Theta}_{u\rightarrow z} \rightarrow \mathrm{E}_L[\grave{\Theta}_l]$.

The uncertainty estimate in Equation (3.38) captures uncertainties due to disturbances, spectral leakage, and time variance.

The nominal FRF estimate ideally describes the response from u to y. Estimation of uncertainty used the spectral power of the disturbance signal, n, for a significant portion of the total uncertainty. Because the disturbances are uncorrelated with the excitation signal, u, the phase relationship remains unknown. In Equation (3.39) the magnitude of $\Theta_{u\rightarrow y}$ is approximated by removing the disturbance spectral magnitude from $\Theta_{u\rightarrow z}$; the phase of $\Theta_{u\rightarrow z}$ is preserved.

$$\left|\Theta_{u\rightarrow y}[\Omega_E]\right| \approx \left|\Theta_{u\rightarrow z}[\Omega_E]\right| - (1 + |W|) \left|\grave{\Theta}_d[\Omega_E]\right|$$
$$\angle\Theta_{u\rightarrow y}[\Omega_E] \approx \angle\Theta_{u\rightarrow z}[\Omega_E] \tag{3.39}$$

The modification in Equation (3.39) is impractical for responses with low output SNR and estimates with significant leakage. In the extreme, removing the null power from z as in Equation (3.39) can result in a negative magnitude of the FRF. Because the examples in this study rely on relatively short excitations (sometimes with significant leakage) and low output SNR to illustrate the estimation of uncertainty, the modification in Equation (3.39) will not be used.

Mean-square coherence of a smooth estimate, $\hat{\gamma}^2$, is often regarded as a single quantitative assessment of estimation quality. Coherence is sensitive to noise contamination, certain nonlinearities, and process noise (unknown or unmeasured plant input that is uncorrelated with the measured plant input) [1, 7]. However, while coherence is sensitive to many sources of estimation error, coherence does not provide insight into the root

source of coherence loss nor does coherence equally capture all sources of error. Furthermore, the coherence of the rough estimates, as in Equation (2.33), and the smooth estimates, as in Equation (3.40), are not similar nor are they sensitive to the same sources of uncertainty.

$$\hat{\gamma}^2_{u \to z}[\omega] := \frac{|\hat{\Phi}_{u \to z}[\omega]|^2}{\hat{\Phi}_{uu}[\omega] \; \hat{\Phi}_{zz}[\omega]} \qquad 0 \le \hat{\gamma}^2_{u \to z}[\omega] \le 1 \qquad (3.40)$$

Throughout this study mean-square coherence is often plotted, for example, along with gain and phase in a Bode plot of an estimated response. This is done merely to maintain prior conventions and for qualitative comparison with the uncertainty estimates.

Another potential source of error and uncertainty stems from the linearity assumption required from Chapter 2.

3.4 Nonlinearities

The frequency response estimation of Chapter 2, and the stability definition in Chapter 4, are predicated on the systems being linear. The nature of nonlinearities in the response function is such that, rather than attempting to quantify the associated uncertainty, nonlinearities should either be avoided or accepted as an inherent characteristic of the real-world response.

Nonlinearities are amplitude dependent, and therefor constant amplitude excitations are generally inadequate to uncover the presence of nonlinearities in the response. It is often advantageous for estimation to define excitations with a low peak factor; however, these excitations also are least likely to uncover the presence of nonlinearities (particularly for small amplitude nonlinearities such as freeplay and deadband). In the presence of nonlinearities a spectra-based frequency response estimate will estimate the first-harmonic of the nonlinear describing function response.

Some results using describing functions (DF) for particular common nonlinearities are presented here. Describing functions are quasi-linear approximations to nonlinear responses based on minimization of the mean square error [40, 41]. The approach to devising appropriate formulations of DFs are motivated by Fourier series expansions of

the nonlinear equations. Describing functions for different nonlinearities are typically found in tables detailing both the parameterization and the type of input required. Different DFs are produced based on the type of input signal; for example, DFs for single sine wave inputs differ from those derived for Gaussian white noise inputs.

A common second-order servo mechanism will be used as the basis for evaluating nonlinearities and DFs. Servo mechanisms are ubiquitous in mechanical systems and have been thoroughly studied. Testing of servos intended for the remote control hobby market has shown a number of nonlinear characteristics [42]. The nonlinearities can be regarded as manifesting at a lower and upper dynamic performance limit; the servo response is predominantly linear between those performance extremes. The lower dynamic performance limit observed for all the servos tested was freeplay. Freeplay in this class of servos is usually a result of gear backlash along with the internal servo controller deadband (deadband is often introduced to prevent limit-cycle oscillations when the inertia load is not know *a priori*). Freeplay is parametrized as a peak-to-peak deflection, y_{fp}, and was estimated to range from 0.25° to more than 2.0° during testing of a wide variety of servos. Servo responses, at their upper dynamic performance limits, potentially encounter numerous limitations; these can range from deflection limits (y_{limit}), rate limits ($\dot{y}_{limit}$), and power limits, as well as limitations introduced within the servo controller itself.

Equation (3.41) depicts a second-order servo model with natural frequency, ω_n, and damping ratio, ζ, in the continuous domain.

$$\frac{y}{u} = \frac{\omega_n^2}{s^2 + 2\zeta\omega_n s + \omega_n^2} \tag{3.41}$$

Parameterization of the servo was estimated from a series of static and dynamic tests designed to identify both the dominant linear response and nonlinearities [42]. The Hitec HS-225BB servo model is used here to simply depict the effect of nonlinearities in the response. This servo model will be used later for excitation refinement and for application in both the aircraft model example and flight test results in Chapter 5. Both the linear and nonlinear parameters for a particular servo, the Hitec HS-225BB, are provided in Table 3.2.

Table 3.2: Model parameters estimated from static and dynamic testing for a Hitec HS-225BB servo.

Parameter	Symbol	Value
Bandwidth (-6 dB) [Hz]	ω_n	6.0
Damping [-]	ζ	0.8
Time Delay [sec]	t_{delay}	0.040
Freeplay [deg]	y_{fp}	1.0
Rate Limit [deg/sec]	$\dot{y}_{limit}$	560.0

Simulation of the nonlinear servo model is conducted with a simple Euler integration scheme with an update rate of 50 Hz ($\Delta t = 0.020$ seconds). The servo simulation incorporating a second-order linear model with rate limiting, deflection limiting, and freeplay is shown in Algorithm 1.

Algorithm 1: Nonlinear servo mechanism simulation.

---

input : $u \in \mathbb{R}^N$

output: $y \in \mathbb{R}^N$

$\dot{y} \in \mathbb{R}^N$

$y[1] = u[1]$

$\dot{y}[1] = 0$

for $n \leftarrow 2$ **to** N **do**

$\qquad \ddot{y} = -2\zeta\omega_n \; \dot{y}[n-1] - \omega_n^2 \; (y[n-1] - u[n])$

$\qquad \dot{y}[n] = \dot{y}[n-1] + \ddot{y} \; \Delta t$

$\qquad$ **if** $|\dot{y}[n]| > \dot{y}_{limit}$ **then** $\qquad\qquad\qquad\qquad$ // Rate limit

$\qquad\qquad \dot{y}[n] \leftarrow \mathrm{sgn}(\dot{y}[n]) \; \dot{y}_{limit}$

$\qquad$ **end**

$\qquad y[n] = y[n-1] + \dot{y} \; \Delta t$

$\qquad$ **if** $|y[n]| > y_{limit}$ **then** $\qquad\qquad\qquad\qquad$ // Deflection limit

$\qquad\qquad y[n] \leftarrow \mathrm{sgn}(y[n]) \; y_{limit}$

$\qquad\qquad \dot{y}[n] = (y[n] - y[n-1])/\Delta t$

$\qquad$ **end**

$\qquad$ **if** $y[n] > y[n-1]$ **then** $\qquad\qquad\qquad\qquad$ // Freeplay

$\qquad\qquad \max(y[n-1], y[n] - \frac{1}{2}y_{fp})$

$\qquad$ **else if** $y[n] < y[n-1]$ **then**

$\qquad\qquad \min(y[n-1], y[n] + \frac{1}{2}y_{fp})$

$\qquad$ **end**

end

The upper dynamic limit this particular servo encounters is a rate limit; the deflection limit is avoided in practice by constraining the servo command signal (the actual servo deflection limit is approximately $\pm$ 90 deg, however applications herein only require $\pm$ 30 deg). Time delay is implemented in the simulation as a simple zero-order hold (not shown in Algorithm 1).

DFs that are frequency-invariant, exhibiting only sensitivity due to the commanded

amplitude, are said to be "simple nonlinearities"; freeplay and deflection limits fall into this category [40]. Many "simple nonlinearities" are specified in terms of a common saturation function, Equation (3.42), where the input amplitude, A, and a limit, δ, normalize the function.

$$\text{sat}(\gamma) := \frac{2}{\pi} \left(\sin^{-1}(\gamma) + \gamma \sqrt{1 - (\gamma)^2} \right)$$
$$\text{where: } \gamma := \frac{\delta}{A} \tag{3.42}$$

The saturation function is depicted in Figure 3.3.
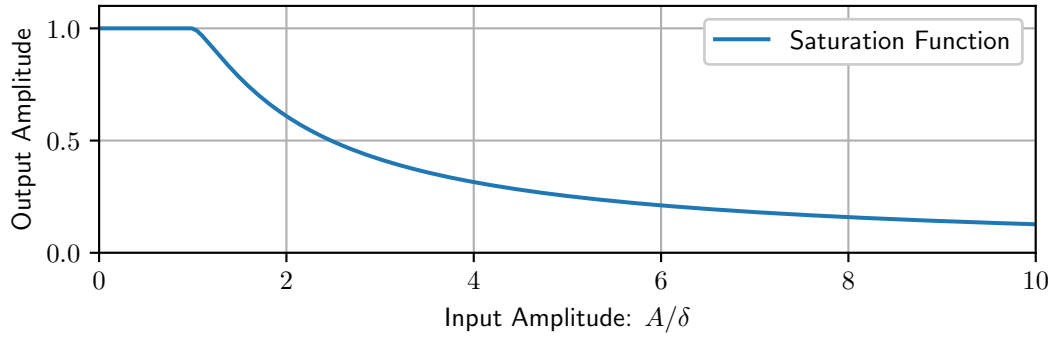
Figure 3.3: Normalized saturation function.

Describing functions that also exhibit variations in frequency are "complex nonlinearities"; rate limits and power limits fall into this category [40, 43, 44]. The describing function approximation of rate limit is scaled by an onset frequency, ω_{onset} that relates the rate limit and input amplitude as: $\omega_{onset} = \dot{y}_{limit}/A$. Equations for the DFs used in the servo model are provided in Table 3.3.

Table 3.3: Describing functions.

Name	Reference	Equation
Deflection saturation	[41, B.7]	$n = \text{sat}(\frac{y_{limit}}{A})$
Time delay	[41, B.33]	$n = \exp(-j\omega t_{delay})$
Freeplay	[41, B.48]	$n = \frac{1}{2}[1 + \text{sat}(\frac{1 - y_{fb}}{A})] - j\frac{1}{\pi}[2\frac{y_{fb}}{A} - \frac{y_{fb}^2}{A}]$
Rate limit	[43]	$n = \frac{4\ \omega_{onset}}{\omega\ \pi} \exp\left(-j\cos^{-1}(\frac{\pi\ \omega_{onset}}{2\ \omega})\right)$

The combined DF approximation for the example servo model is depicted in Figure 3.4.
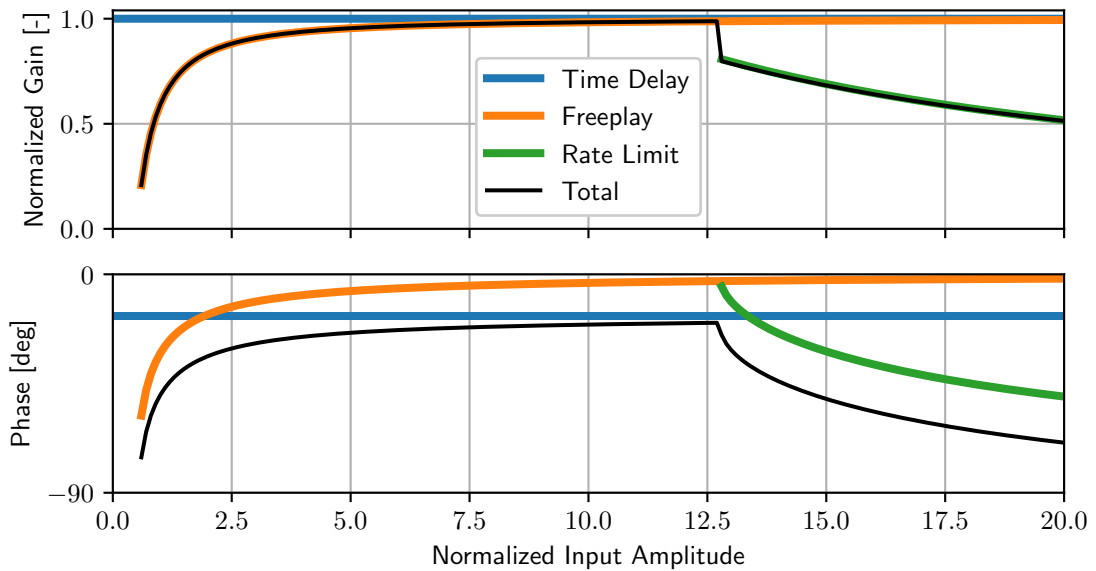
Figure 3.4: Constituent components of the servo describing function.

Freeplay dominates the DF response at low amplitudes. An excitation amplitude of approximately 5 deg is required to reduce the nonlinear residual error to less than 5%; this is despite the fact that the freeplay magnitude is 1°. The rate limit becomes

significant at an amplitude of 12.5°, where a significant jump is apparent. A means to quantify the estimation error due to nonlinearities is not readily apparent, instead a framework for avoiding nonlinearities along with an application example is presented in Section 3.5.

As mentioned earlier it may be desirable to avoid nonlinear characteristics in the response estimates, however, this may not always be the case. For a typical system identification objective, the goal would be to estimate the linear response and any nonlinearities within the response. Thus, for the simple servo example the objective would be to estimate all the parameters in Table 3.2: ω_n, ζ, t_{delay}, y_{fp}, and $\dot{y}_{limit}$. However, for estimation of stability margins the estimated response that represents the best linear approximation to the actual response (including linear and nonlinear components) may be more appropriate. In the proceeding, it is assumed that the desire will be to avoid any low amplitude nonlinearities (freeplay in the servo model).

3.5 Excitation Refinement

With the challenges introduced by nonlinearities and time-variance, the excitation definitions are revisited. A framework for *in situ* excitation modification is presented, along with an example using a simple servo mechanism model. The excitation refinement is separated into two phases. First, an excitation refinement phase modifies the excitation amplitudes to avoid nonlinearities and ensure sufficient system response. During this phase, the characteristics of the disturbance environment are estimated and projected to predict the final estimation error. The focus of the refinement is to establish a good selection of excitation parameters for the final excitation; since multiple excitations will be used, the emphasis is on reducing the time duration of each excitation in the refinement.

A single cost-function for excitation refinement is not apparent, rather a rule-based set of criteria is demonstrated via example. Specifics of the rules based criteria will vary by application and likely rely upon pertinent heuristics and "rules-of-thumb". There are several potential metrics that can be employed during the refinement phase. Signal-to-Noise ratio, via the Null frequency evaluation, allows for isolation of the extraneous disturbances which should be largely invariant to nonlinearities. Coherence may be a

valuable metric in some applications, for the following example the coherence is not employed as a metric (based on the results from Section 3.4).

Some additional results using the servo model of Section 3.4 is presented in Section 3.5.1. These results provide some context and motivation for the approach to excitation refinement in Section 3.5.2.

3.5.1 Nonlinear Servo Model Response

The refinement example makes use of the nonlinear servo mechanism described in Section 3.4; the specific system is defined in Equation (3.41) and Table 3.2. Both input and output disturbances are introduced as zero-mean additive GWN, with input standard deviation, σ_u, and output standard deviation σ_y.

The nonlinear system was simulated with excitation amplitude varying from 0.5 degrees to over 20 degrees in order to cover the low and high amplitude nonlinearities. The FRE was computed for each amplitude. The FRE magnitude and coherence at three frequencies (1.1, 3.1, and 5.1 Hz) and the complete range of input amplitudes are highlighted in Figure 3.5.
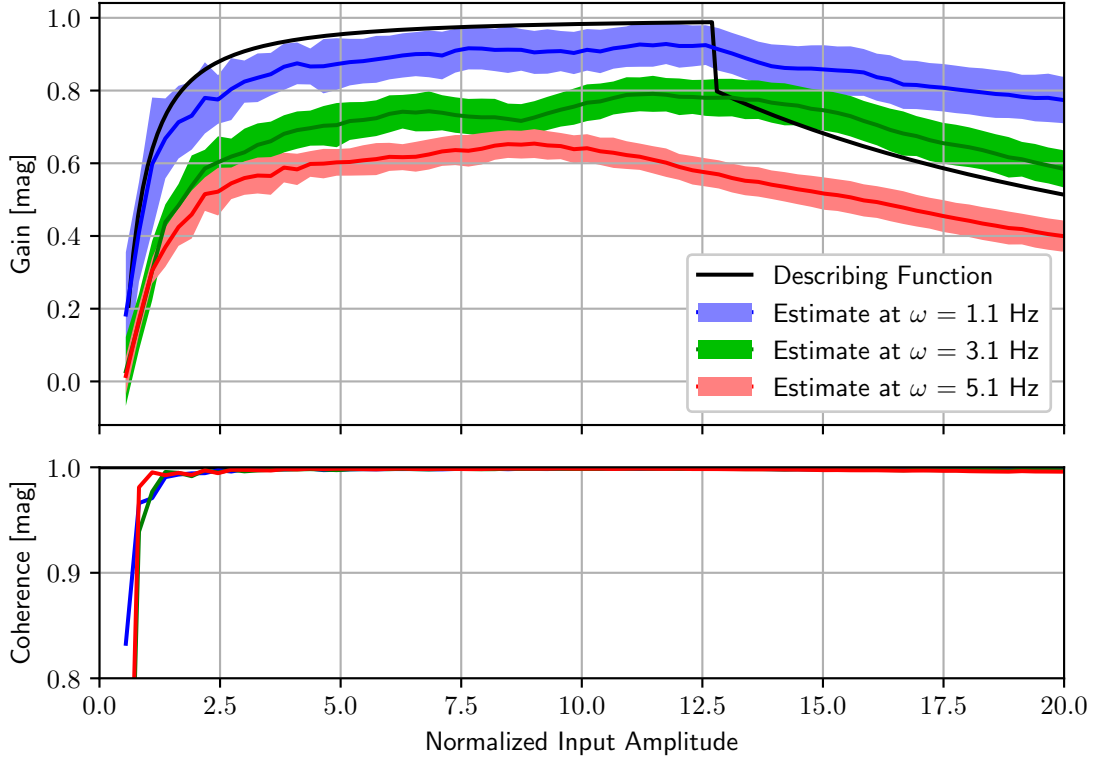
Figure 3.5: Servo model using describing functions and estimated response function gain with respect to amplitude at 3 representative frequencies.

The DF approximation and estimated frequency response are presented in Figure 3.5. The servo model is excited, and the response function is estimated at each command amplitude. The input signal for the FRE is a multisine, rather than a single sine wave input as in the DF specification. The multisine contains a range of sine wave frequencies and a range of amplitudes in the time-domain, making a direct comparison between the DF and FRE imprecise. In Figure 3.5 the amplitude of the multisine has been scaled by: A/A_{pf}, where A_{pf} is the peak factor of the multisine excitation. Similarly, the scale of the rate limit of the DF was taken as: y_{limit}/A_{pf}. The FRE has been normalized at each amplitude.

The servo model has significant nonlinearities at both small and large amplitude commands (as indicated by the DF). The uncertainty estimates are fairly minimal and

relatively consistent with changes in amplitude and consistent at the 3 frequencies depicted in Figure 3.5.

Note that the estimated coherence in Figure 3.5 is near unity despite the presence of significant nonlinearities. This result further confirms that coherence is not a satisfactory metric for many commonly encountered set of nonlinearities. Regarding testing for nonlinearities, Pintelon specifically notes that [2, Section 4.1]:

> Another popular test is to check the coherence. This method does not allow separation of noise disturbances from nonlinearity problems and it fails completely for periodic excitations.

The estimation error and estimation uncertainty are shown in Figure 3.6. The error is computed as the MSE with respect to the underlying linear model (i.e., the linear second-order servo model characterized by only ω and ζ). It is clear that for nonlinear systems, the estimated uncertainty does not capture the true error; however, this is an expected result. The FRE produces an estimate that approximates a linear representation (the first harmonic of a describing function) of the nonlinear system, rather than the underlying linear model. Furthermore, the amplitude of the excitation time-series is not constant, as would be the case for a single frequency sine wave or a frequency sweep, therefor the FRE is estimating a describing function acting at a range of amplitudes.
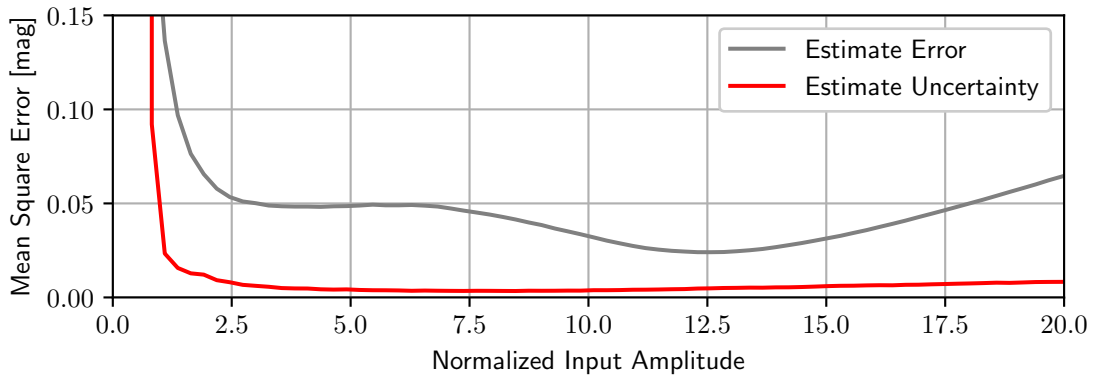
Figure 3.6: Servo model estimation error and predicted uncertainty with respect to the underlying linear model dynamics.

In Figure 3.6 it is also clear that the minimum MSE of 2.2% occurs at a normalized

input amplitude of 12.5 deg (corresponding to an excitation amplitude of 23.0 deg). A fairly wide range of normalized input amplitudes results in MSE less than 5%; ranging from 3.0 to 18.0 degrees (excitation amplitude of 6.0 to 32.5).

3.5.2 Excitation Refinement Example

The goal of excitation refinement is to ensure the excitation avoids the nonlinear performance extremes. Some knowledge of the system application is required to determine an approach to excitation refinement. This example assumes that small amplitude excitations are desirable and that avoiding small amplitude nonlinearities is also desirable. The exact characteristics of the linear and nonlinear models are assumed unknown, however, sufficient prior knowledge is assumed in order to provide an initial amplitude. So, for this example, it may be known that the system has freeplay, but the freeplay amplitude is unknown; similarly, a rate (or power) limit can be expected although the nature and limit of the nonlinearity are unknown.

The approach to excitation refinement here will start with a small amplitude and increase the amplitude until an additional amplitude increase would result in negligible improvement in the final estimate. An initial refinement excitation is defined in Table 3.4.

Table 3.4: Refinement phase excitation and FRE definition.

Parameter	Symbol	Value
Frequency Step	$\Delta\omega_{Refine}$	0.4 Hz
Window Function		Rectangular
Duration Time	t_{Refine}	5 sec
Minimum Frequency	ω_{min}	0.2 Hz
Maximum Frequency	ω_{max}	15 Hz
Initial Amplitude	a_i	0.40 deg

Some limited prior knowledge of the system were required to specify the refinement excitation frequency range of interest (ω_{min} and ω_{max}) and frequency resolution ($\Delta\omega_{Refine}$). The refinement excitation is restricted to one cycle of the excitation, and only a single segment of the spectra is estimated with a rectangular window function. The duration of the excitation, t_{Refine}, is a result of first establishing a frequency step size and applying Equation (3.27) to compute the duration of a single bin. The minimum frequency then follows directly from a single cycle of the excitation. A multisine excitation, with a Schroeder phase distribution, is used for the first iteration of refinement. The initial refinement excitation amplitude, a_i, is constant at all frequencies; the excitation peak factor is 2.0 deg.

Based on the response characteristics in Section 3.5.1 the freeplay nonlinearity would be expected to have a significant impact on the FRE.

A simple gradient descent, using only first-order estimates, is employed with a simple step size scheme to adjust the excitation amplitudes. The cost function for each iteration is computed simply as $1/\sum|\Theta_{u\rightarrow z}|$, where the summation is taken across all the frequencies in the estimate. At small amplitudes, where freeplay has a significant impact, increasing the input amplitude will result in greater total system gain (as shown in Figure 3.5); thus, a decrease in the reciprocal of the total gain: $1/\sum|\Theta_{u\rightarrow z}|$. The final estimation goals are tabulated in Table 3.5.

Table 3.5: Final estimation goals definition.

Parameter	Symbol	Value
Relative Error	ε_{Goal}	5.0%
Frequency Step	$\Delta\omega_{Final}$	0.2 Hz
Window Function		Hann

The Final objective is to achieve a relative error of less than 5%. The final excitation must also achieve less than 5% spectral leakage, and will use a "Hann" window function and tighter frequency resolution than the refinement phase.

After each iteration of the refinement the frequency response is estimated along

with critical metrics such as gain, SNR, uncertainty, and coherence. Several stopping criteria were defined for this example based on the final estimation objectives. First, if the estimated uncertainty reached a level sufficient to achieve the final estimation goal, the refinement was halted. Second, if the estimated uncertainty started to increase significantly, the refinement was halted. Finally, if the predicted duration of the final phase excitation was changing less than the duration of the refinement excitation, this indicated that the refinement was yielding diminishing returns and the refinement was halted. Additional stopping criteria could leverage the SNR estimate, coherence estimate, and the estimated gain depending on the particulars of the application.

In this example, for each refinement iteration, the amplitude of excitation was increased by 0.25 deg at each frequency that showed an estimated gain increase. The excitation was decreased by 0.125 deg for each excitation frequency that showed a gain decrease and the SNR was sufficiently high (a threshold of SNR = 9 was used). The Schroeder multisine phases were re-computed between each refinement iteration.

The stopping criteria in this example was achieved in 5 iterations; having reached diminishing returns on the final excitation duration. The uncertainty estimate for each iteration is depicted in Figure 3.7.
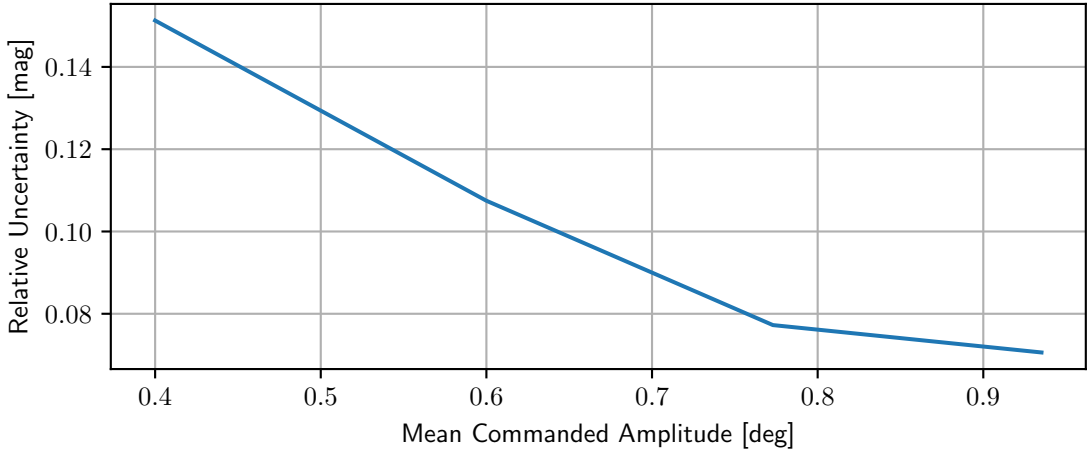
Figure 3.7: Refinement phase estimated uncertainty.

The last refinement excitation had a mean amplitude of 0.95 degrees; recall that these are the amplitudes of the constituent sine waves in the excitation, not the amplitude of

the multisine time-series. The RMS of the last refinement excitation was 3.5 degrees, with peaks up to 7.7 degrees. While both the RMS and peaks of the excitation are well above the freeplay value, there are commanded amplitudes within the excitation that are still less than the freeplay value.

After the refinement phase, a final excitation is defined using projections from the final refinement iteration. The time duration for the final excitation is computed as Equation (3.43).

$$t_{Unc} = t_{Refine} \frac{\Delta\omega_{Refine}}{\Delta\omega_{Final}} (\frac{\tilde{\tilde{\varepsilon}}_{Refine}}{\varepsilon_{Goal}})^2 \tag{3.43}$$

The ratio of step size $\Delta\omega$ between the refinement and final excitations linearly scales the required time duration. The ratio of the estimation uncertainty from the last refinement phase FRE, ε_{Refine}, and the objective uncertainty, ε_{Goal}, is squared; indicating the relative importance of uncertainty on the final excitation duration.

The time duration required to meet the desired leakage objective is computed via Equation (3.44). The equation for the leakage power, Table 3.1 for the "Hann" window, was used to compute the number of required bins, b.

$$t_{Leakage} = \frac{4\pi \ b}{\Delta\omega_{Final}} \tag{3.44}$$

The total excitation duration required was determined by the uncertainty goal; whereas, the time required for the leakage objective was determined by the minimum duration in each rough segment. Combining the required duration for leakage and uncertainty into an integer number of excitation cycles, R, and number of segments, L, yields a minimal time duration to meet both objectives, t_{Final}, Table 3.6.

Table 3.6:   Final phase derived excitation and FRE parameters.

Description	Symbol	Value
Required Duration for Uncertainty	t_{Unc}	≥ 31.1 sec
Required Duration for Leakage	$t_{Leakage}$	≥ 19.4 sec
Number of Cycles	R	4
Number of Rough Segments	L	2
Duration Time	t_{Final}	40 sec

This resulted in 2 segments in the FRE, with 4 cycles of the lowest frequency in each segment (two 10 second bins), for a final total excitation time of 40 seconds. The time histories of the excitation signal and measured response for the iterations of the refinement phase and the final phase are shown in Figure 3.8.
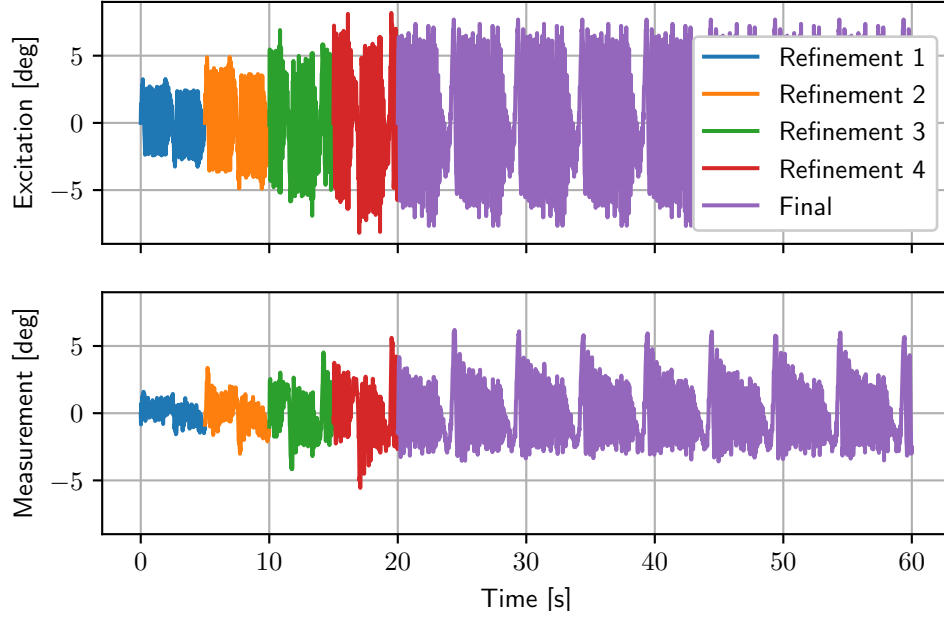
Figure 3.8: Time histories of four iterations of refinement phase and the final phase excitation and response.

Each iteration of the refinement required 5 seconds of excitation, for a total time of 20 seconds. The final excitation required 40 seconds to achieve the desired uncertainty. The refinement consumed 33% of the total time required for the estimation.

The estimation error and uncertainty estimates for each iteration of the refinement and each segment of the final estimation are shown in Figure 3.9.
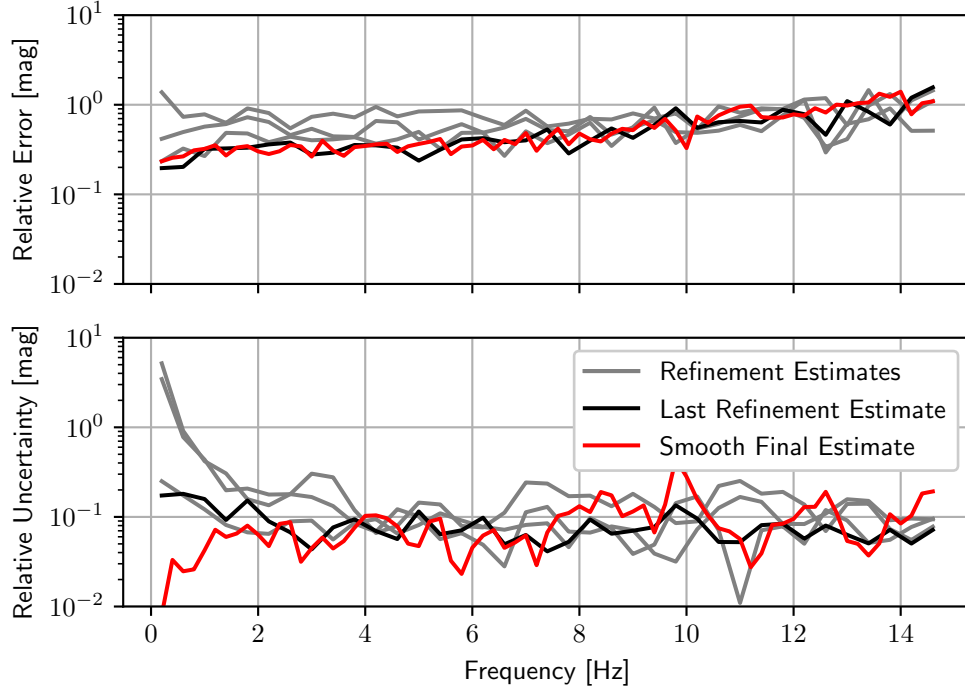
Figure 3.9: Relative Error and Uncertainty spectral magnitude for four iterations of refinement phase and two segments of the final phase estimates.

The estimation error is taken with respect to the nominal linear model that underlies the system. The uncertainty estimate is significantly lower than the estimate error, particularly for the final phase estimates, due to the linear FRE approximating a nonlinear system. This result is similar to what was depicted in Figure 3.6. The relative uncertainty estimate also shows a clear reduction in uncertainty at low frequencies with successive increases in excitation amplitude during refinement. The relative uncertainty of the final rough estimates also shows a reduction in uncertainty as a result of

This example of excitation refinement illustrates use of estimation metrics in a rule-based refinement strategy, where the goal was to reduce the impact of freeplay without encountering saturation. While the final estimation has been improved by refinement for some metrics, the specifics of final application of such a technique are highly dependent upon prior knowledge of the system and the objective of the estimation activity.

3.6 Open-Loop MIMO FRE Example Revisited

The Example used in Section 2.4 will be expanded to incorporate uncertainty quantification and propagation. Estimation of the nominal system, $\hat{\Theta}_{u \to z}[\Omega_E] \,\hat{=}\, G(s)$, and the magnitude of the disturbance, $\hat{\Theta}_{u \to z}[\Omega_N] \,\hat{=}\, N(s)$, was shown in Section 2.4. The disturbance estimation will be propagated, along with the other sources of estimation error, to the total estimation of uncertainty. The objective is to show that the uncertainty estimate provides a tight over-bound of the estimation error.

The nominal FRF, $\bar{G}$, is estimated as the expected value of the L rough estimate, $\bar{\Theta}_{u \to z}$.

$$\bar{G}[\Omega_E] \,\hat{=}\, \mathrm{E}_L[\bar{\Theta}_{u \to z}[\Omega_E]] \tag{3.45}$$

Three sources of potential uncertainty are quantified as real valued magnitudes, $\dot{\Theta}_d$, $\dot{\Theta}_w$, and ε_t in Equation (3.46); representing the uncertainty due to disturbances, spectral leakage, and time-variance.

$$\dot{G}[\Omega_E] \,\hat{=}\, \mathrm{E}_L[\dot{\Theta}_{u \to z}[\Omega_E]] = \left[(1 - \frac{1}{\sqrt{L}})\varepsilon_t[\Omega_E] + \frac{1}{\sqrt{L}}\right] \ \mathrm{E}_L[(\dot{\Theta}_d[\Omega_E] + \dot{\Theta}_w[\Omega_E])] \tag{3.46}$$

As in the prior example, estimation of the system again only uses the time-series u and z. The FRF estimate is then: $\hat{G}[\Omega_E] = \bar{G}[\Omega_E] + \Delta \circ \dot{G}[\Omega_E]$, where Δ is a complex-valued matrix with all elements having magnitude less than unity; as introduced in Equation (3.19). The elements of the perturbation are bounded to have magnitude less than one for all frequencies. Element-wise multiplication (denoted by: $\circ$) allows $\hat{G}$ to be defined in the entire range of estimated uncertainty.

A rectangular window function and three non-overlapping segments were used in the estimation. Segments are aligned to the three repeated excitations, thus segments equate to one normalized bin width. Power leakage was approximated via the Dirichlet approximation to be approximately 31%; thus uncertainty due to disturbances are amplified by 1.31 due to leakage. The excitation-to-null leakage was estimated with the input spectra of the excitation and null frequencies, as in Equation (3.25), to be approximately zero; $\hat{\Theta}_{leakage} \ll 0.01\%$.

Time-variance should also be near zero for this system as both extraneous inputs, the excitation and disturbance source, m, are IID and both the plant and disturbance models are time-invariant. The time-variance of the measurement time-series, estimated as $\text{Var}_L[\Phi_{zz}[\Omega_N]]$, in the excitation frequency set to have a mean value (the expected value here is the mean over all input-output pairs and all frequencies), $\text{E}[\text{Var}_L[\Phi_{zz}[\Omega_N]]] \ll 0.01\%$.

The objective is for the estimated uncertainty to be larger than the magnitude of the estimation error, $\grave{G} > |G_{err}|$, thus ensuring the estimation is conservative. The estimated uncertainty should also provide an approximation of the error itself, $\grave{G} \approx |G_{err}|$.

The number of segments, L, in the estimation reduces the total uncertainty estimation as a result of treating them as independent measures, $\propto \frac{1}{\sqrt{L}}$. With only three data points, corresponding to the three segments in the FRE, the variance estimates should be treated with caution.

The final source of uncertainty is the disturbance itself, which was depicted previously in Section 2.4. The results of the FRE are depicted in Figure 3.10 through Figure 3.13.
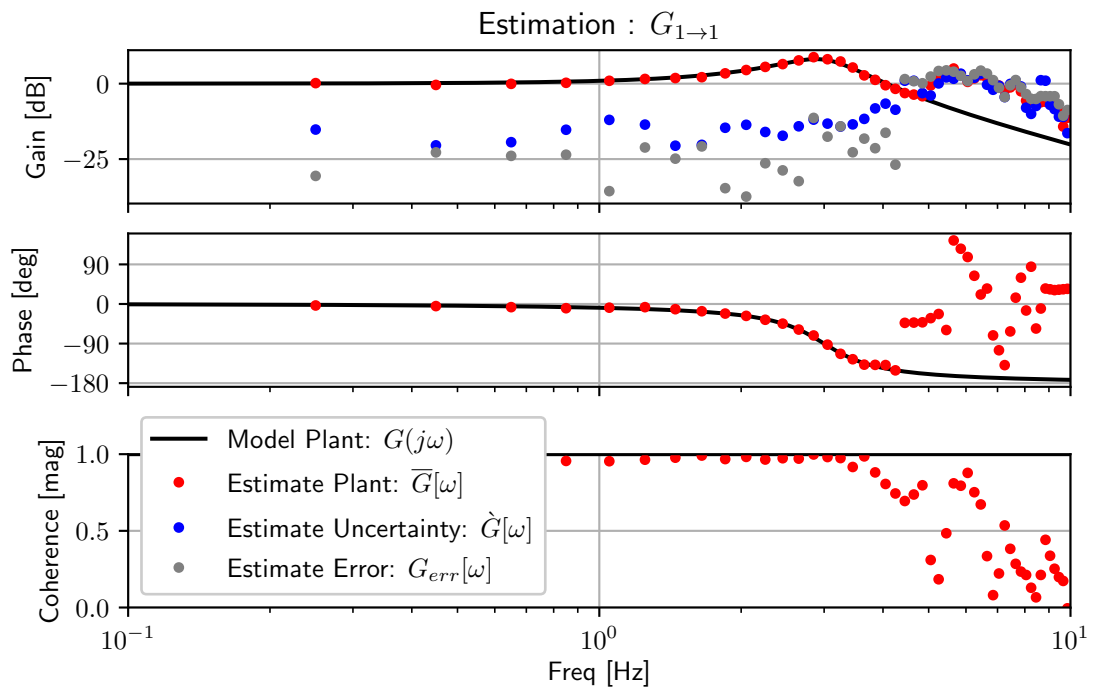
Figure 3.10: Bode plot of the FRE for u_1 to z_1 showing the plant model response and plant estimation as well as the estimation error and uncertainty estimation.
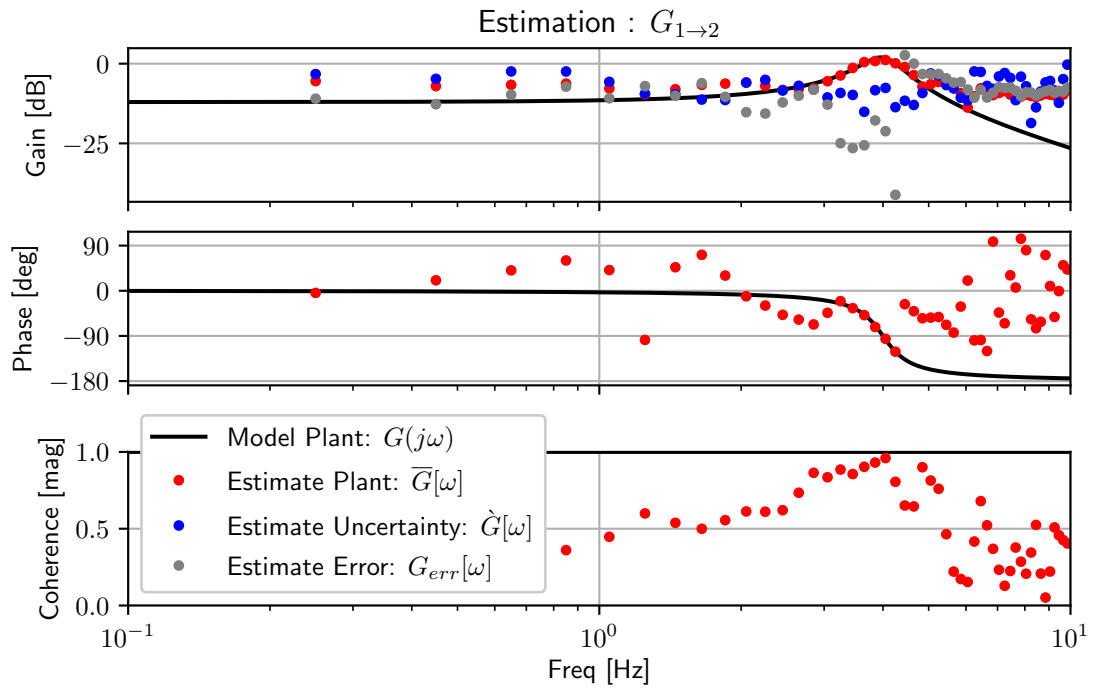
Figure 3.11: Bode plot of the FRE for u_1 to z_2 showing the plant model response and plant estimation as well as the estimation error and uncertainty estimation.
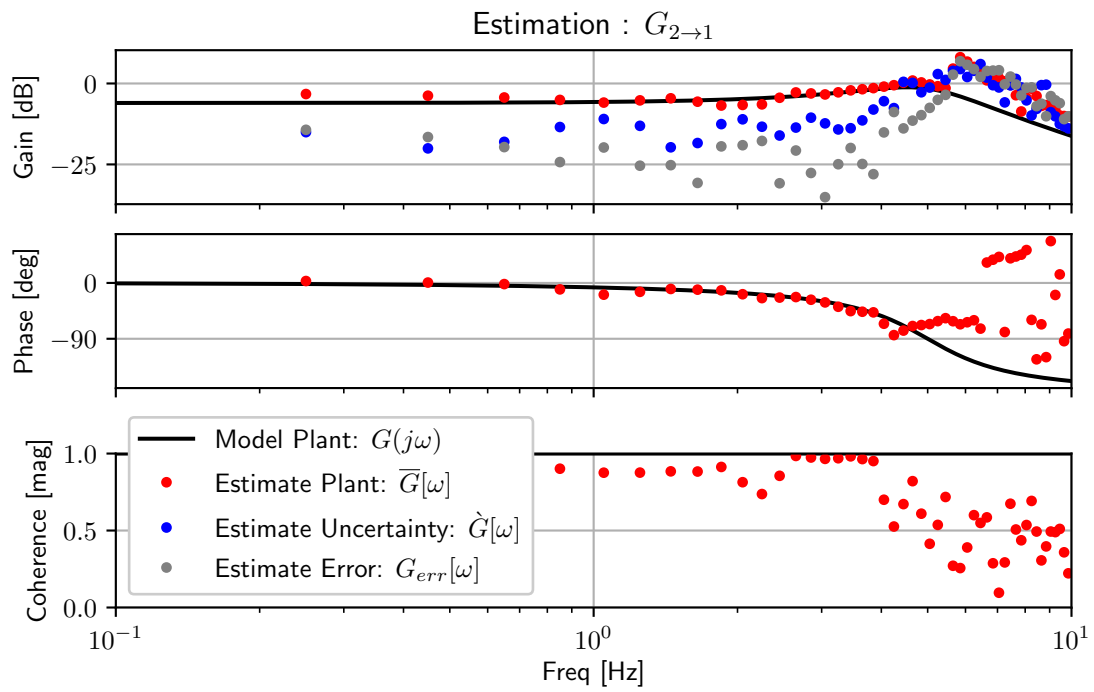
Figure 3.12: Bode plot of the FRE for u_2 to z_1 showing the plant model response and plant estimation as well as the estimation error and uncertainty estimation.
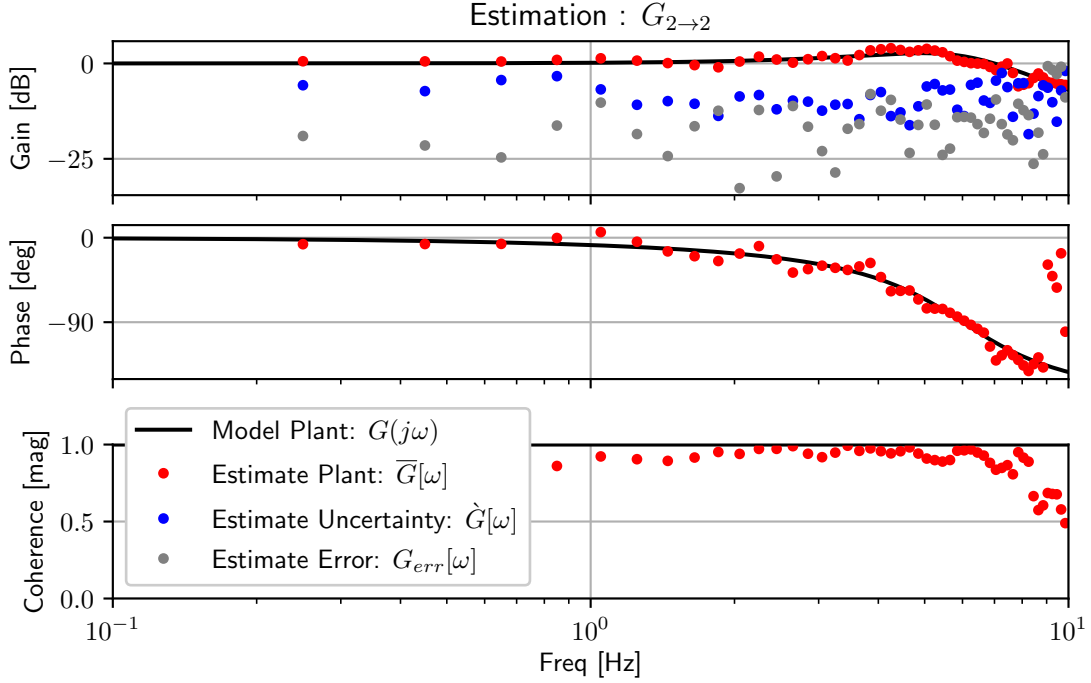
Figure 3.13: Bode plot of the FRE for u_2 to z_2 showing the plant model response and plant estimation as well as the estimation error and uncertainty estimation.

The plant model, G, and nominal estimate, $\bar{G}$, are unchanged from Figure 2.6 through Figure 2.9. The magnitude of uncertainty, G_{err}, can be compared visually to the magnitude of the estimation error, $\grave{G}$. In almost all instances, the uncertainty estimate is larger than the estimation error; in this particular example, the uncertainty over-bounded the error in 68.5% of the total estimated points.

As noted earlier mean-square coherence, γ^2, can be sensitive to time-variance, non-linearities, and uncorrelated disturbances making it a tempting metric for uncertainty. However, the uncertainty derived from only the non-coherent spectra frequently under-estimates the estimation error. In this particular example, the non-coherent response over-bounds the error in 50.5% of the total estimated points. The estimation error, estimated uncertainty, and non-coherent response magnitudes are compared in Figure 3.14 through Figure 3.17.
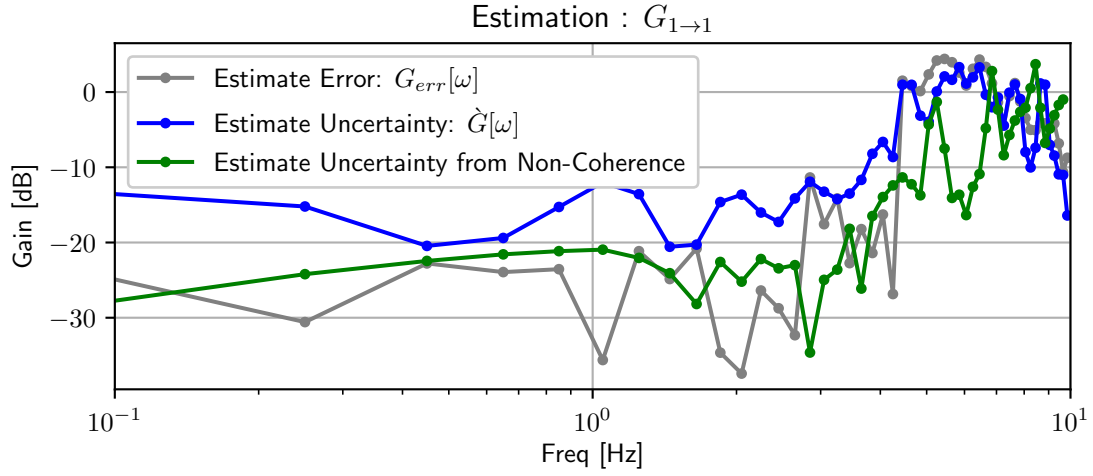
Figure 3.14: Magnitude plot of the FRE for u_1 to z_1 showing the magnitude of the estimation error, estimation uncertainty, and uncertainty estimate from non-coherent response.
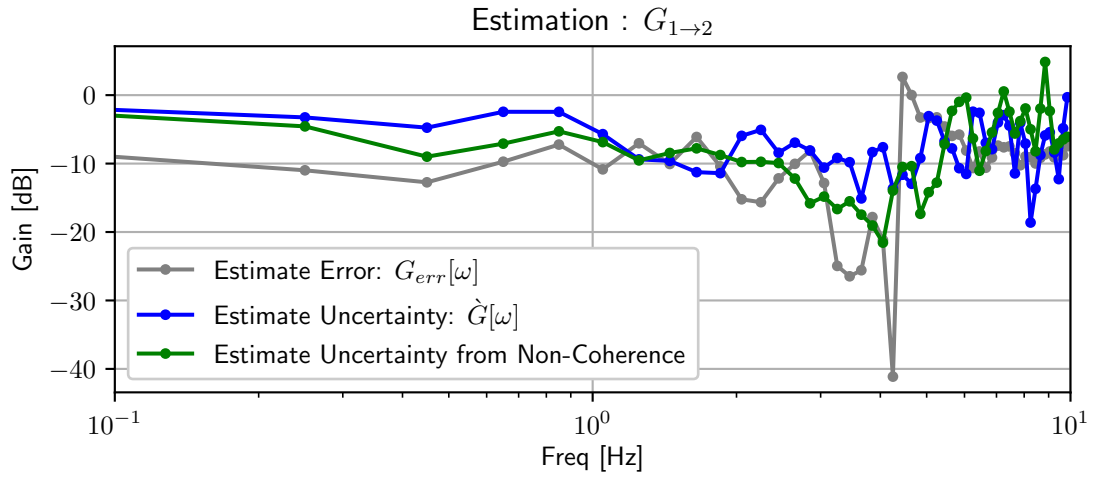
Figure 3.15: Magnitude plot of the FRE for u_1 to z_2 showing the magnitude of the estimation error, estimation uncertainty, and uncertainty estimate from non-coherent response.
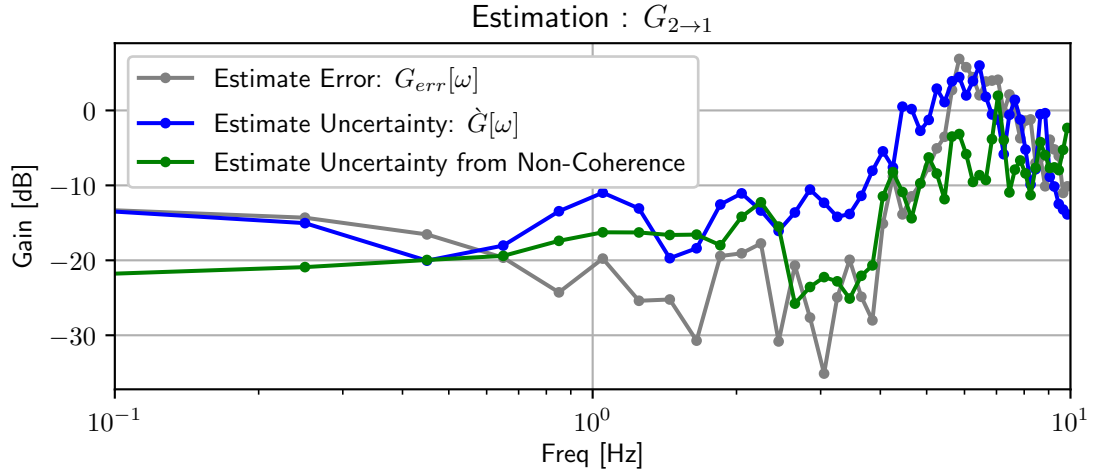
Figure 3.16: Magnitude plot of the FRE for u_2 to z_1 showing the magnitude of the estimation error, estimation uncertainty, and uncertainty estimate from non-coherent response.
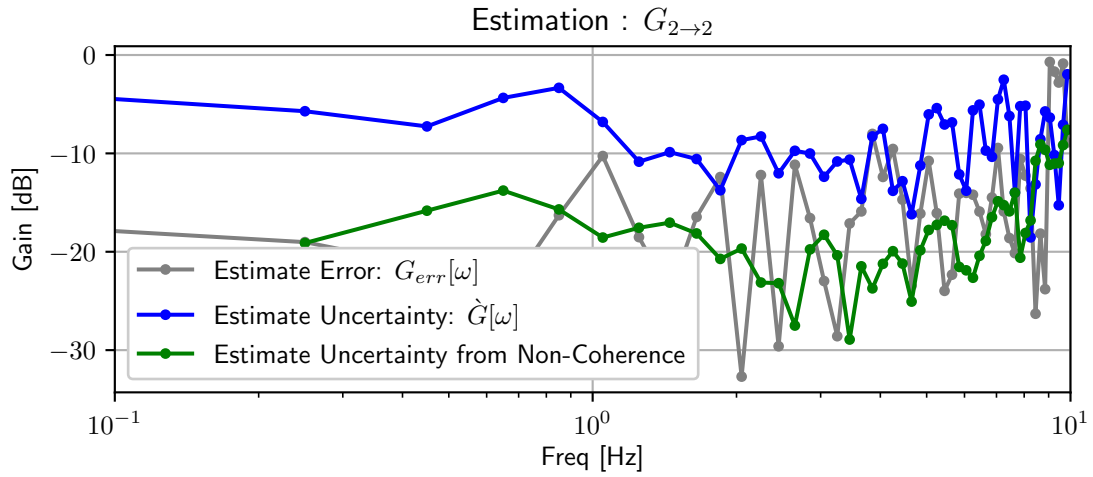
Figure 3.17: Magnitude plot of the FRE for u_2 to z_2 showing the magnitude of the estimation error, estimation uncertainty, and uncertainty estimate from non-coherent response.

Chapter 4

Stability

The generic system block diagram, Figure 1.1, is repeated here as Figure 4.1.
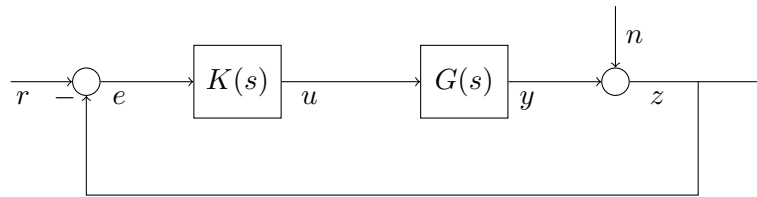
Figure 4.1: System Block Diagram.

Recall that the controller, $K(s)$, and plant, $G(s)$, are presented as linear time-invariant systems and may be MIMO; therefore, signals may be multivariate. The reference input (r), measured output (z), error (e), and control command (u), will be considered measurable signals.

Definitions for commonly used loop transfer functions are defined in Table 4.1, based on the block diagram in Figure 4.1.

Table 4.1: Loop transfer function definitions.

Loop Function Name	Loop Function Equation
Output Loop Transfer Functions	$L_o(s) = G(s)K(s)$
Output Sensitivity Function	$S_o(s) = (I + L_o(s))^{-1}$
Output Complimentary Sensitivity Function	$T_o(s) = (I + L_o(s))^{-1} L_o(s)$
Input Loop Transfer Functions	$L_i(s) = K(s)G(s)$
Input Sensitivity Function	$S_i(s) = (I + L_i(s))^{-1}$
Input Complimentary Sensitivity Function	$T_i(s) = (I + L_i(s))^{-1} L_i(s)$

In general, assured stability requires that the conditions on both the input and output loop transfer functions; L_i and L_o are satisfied. For this 1 degree-of-freedom (1DOF) system, useful excitation injection locations will be at u and at e; and FRE will yield the output and input complementary sensitivity functions, T_o and T_i.

The system equations for the block diagram in Figure 4.1 are shown in Equation (4.1) for output signals z, u, and e along with the input signals n and r.

$$\begin{bmatrix} z \\ u \\ e \end{bmatrix} = \begin{bmatrix} S_o(s) & T_o(s) \\ -S_i(s)K(s) & S_i(s)K(s) \\ -S_o(s) & S_o(s) \end{bmatrix} \begin{bmatrix} n \\ r \end{bmatrix} \tag{4.1}$$

Additional expressions, incorporating an additional excitation signal as an input prior to the plant, introduces additional internal systems: S_oG and T_i. Baring pole-zero cancellations in the right-half plane, if one of the internal systems is stable, then all the internal systems are stable [11].

The notation here will be that loop-functions are composed of a nominal and an uncertain component, as in: $\hat{T} = \bar{T} + \Delta \circ W_T$. This form aligns with the nominal and uncertain components of the FRE. The input and output signal both have C channels. The nominal component, $\bar{T}$, of the loop-functions will be estimated as a complex-valued frequency response matrix at each evaluated frequency: $\bar{T} \in \mathbb{C}^{C \times C}$. The uncertain component is partitioned into a real-valued frequency response, $W_T \in \mathbb{R}^{C \times C}$, representing the magnitude of the estimated uncertainty and a complex-valued perturbation matrix at each evaluated frequency, $\Delta \in \mathbb{C}^{C \times C}$ in Equation (4.2).

$$\boldsymbol{\Delta} := \{\Delta_{i \to o} : |\Delta_{i \to o}| \leq 1 \quad \forall \omega,$$
$$(i, o) \in \{1, 2, \ldots, C\}\} \tag{4.2}$$

Input and output sensitivity functions are related to the complementary sensitivity functions via the property that $S + T = I$; therefor, S_o and S_i are easily obtained: $\bar{S} = I - \bar{T}$ and $W_S = -W_T$. Stability conditions originate in terms of the loop functions, L_o or L_i. For MIMO systems, the stability criteria and resulting margins can be specified in terms of sensitivity function, S_o or S_i. For SISO systems, a transformation from S to L is required for both the nominal and uncertainty components.

Multivariate nominal stability (NS) will first be stated for only the nominal system with, $\hat{L} = \bar{L}$. Multivariate robust stability (RS) will expand upon the NS to incorporate the estimation uncertainty, $\hat{L} = \bar{L} + \Delta \circ W_L$, with both an unstructured and structured perturbation as RS_U and RS_S. Finally, stability in a SISO framework will be briefly stated. The desire here is to establish stability margins with common criteria for NS, RS_U, and RS_S.

4.1 Multivariate Nominal Stability

The Nyquist Stability Theorem (NST), stated in Theorem B.3, forms the basis of the NS criteria. The NST can be summarized to state that a closed-loop system is stable, if and only if, $\det(I + L)$ makes counter-clockwise encirclements of the origin the "correct" number of times (the number of unstable poles of L) and does not pass through the origin.

Determination of the number of unstable poles of L and determination of encirclements is challenging with frequency response function data. The NST criteria are generally applied with parametric system models, where pole determination and interpolation can be easily and accurately applied.

Several alternatives to NST include the Routh-Hurwitz stability criteria, Small Gain Theory (SGT), and bound-input bound-output (BIBO) stability theory. SGT is defined as Theorem B.4 and BIBO is defined as Theorem B.2. Application of Routh-Hurwitz and BIBO stability in the frequency-domain necessitates the determination of system poles, similar to NST, and are otherwise no more amenable to assessment with estimated

non-parametric responses. Direct application of SGT can be easily assessed as $||L|| < 1$, the criteria requires L is stable. The SGT is very conservative to the point of diminishing utility. An application of BIBO stability and SGT in the time domain will be addressed to provide an addition stability assessment.

Assessment of multivariate NS here will follow from the NST criteria, Theorem B.3, and focus on the quantifiable criteria that $\det(I + L) \neq 0$. The NS criteria are defined along a particular path: $s = j\omega$. Further necessary conditions for the NST criteria will be assumed; the number of encirclements of $\det(I + L)$ is correct and there are no internal systems with pole-zero cancellations in the right-half plane.

The NS criteria in the frequency domain are stated as Equation (4.3) with the conditions for encirclements and no pole-zero cancellation.

$$
\begin{aligned}
\text{NS} \quad &\Leftrightarrow \quad \det\big(I + \bar{L}(j\omega)\big) \neq 0, \quad \forall\, \omega \\
\text{and:} \quad &\det\big(I + \bar{L}(j\omega)\big) \text{ has ``correct'' encirclements} \\
\text{and:} \quad &\text{Internal systems do not contain pole-zero cancelations}
\end{aligned}
\tag{4.3}
$$

The prior conditions on "correct" encirclements and no internal pole-zero cancellations will be partially supported by checking that signals in the system do not grow over the duration of system excitation. Internal pole-zero cancellations are generally not perfect with realized systems, it is more likely that the observed system would indicate a near pole-zero cancellation; in practice the prior condition on internal system pole-zero cancelations can be neglected.

Observation of growth in any of the output signals, z, u, and e in Equation (4.1), would indicate an unstable system. Several simple tests are possible to determine if the output response is bounded. Generally, inspection of the output response in the time-domain is sufficient. The PSD of the output signals can also be inspected on a segment-by-segment basis (or on a sliding or accumulating basis) in the frequency domain to indicate unstable responses and highlight specific unstable modal frequencies.

Checking for growth in the time-domain is somewhat analogous to a BIBO or SGT type argument. However, here the argument is limited to assessing the response to a particular input; in the context of system estimation, this includes an excitation input. Extrapolation to any input, as required for BIBO or SGT assessment, is not assured. Adequacy of the excitation to yield FRE results throughout the frequency range of

interest provides some assurance that any unstable system modes have been adequately excited. Observed growth in response magnitude is sufficient to indicate violation of the NS criteria. Observed boundedness of the time-domain response is a necessary condition but does not fully address the two untested conditions of Equation (4.3); namely, internal pole-zero cancelations and that the "correct" number of encirclements are satisfied. Satisfaction of these two conditions will be revisited following discussion of the assessment of robust stability (RS).

The frequency-dependent stability margin, κ_{NS}, for NS is stated as the distance to violation of the determinant condition of Equation (4.3), Equation (4.4).

$$\kappa_{\mathrm{NS}}(j\omega) := \underline{\sigma}(I + \bar{L}(j\omega)), \quad \forall\, \omega \tag{4.4}$$

The NS margin requires a prior assumption that the nominal system is stable; as noted earlier, proving NS is impractical with the estimated FRF. The minimum singular value $\underline{\sigma}$ is used as the induced norm measure to the singularity condition of $(I + \bar{L})$, noting that $\det(I + L) = 0$ if and only if a singular value of $(I + L)$ equals zero. The minimum value of $\kappa_{\mathrm{NS}}(j\omega)$ for all frequencies provides a scalar stability margin metric.

The FRE of closed-loop systems naturally results in the estimation of T or S, additional transformations are required to yield an estimate of L, as will be discussed in Section 4.4. The stability margin of the nominal loop function $\bar{L}$ can be rewritten in terms of the nominal sensitivity function $\bar{S}$, Equation (4.5).

$$\kappa_{\mathrm{NS}}(j\omega) = \frac{1}{\bar{\sigma}(\bar{S}(j\omega))}, \quad \forall\, \omega \tag{4.5}$$

The derivation of Equation (4.5) makes use of a property of singular values of a matrix inverse, Definition B.5, which can be stated here as: $\underline{\sigma}(I + \bar{L}) = 1/\bar{\sigma}(\bar{S})$. Nominal stability is assumed if κ_{NS} is sufficiently greater than zero and the system does not grow unbounded.

4.2 Multivariate Robust Stability

Robust stability analysis follows a similar approach as used for nominal stability. RS is based on the NST, as was the case for NS, and includes a prior condition that NS is

satisfied, Equation (4.6).

$$\text{RS} \iff \det\left(I + \hat{L}(j\omega)\right) \neq 0, \quad \forall \, \omega, \quad \text{NS}$$

$$\text{and:} \quad \det\left(I + \hat{L}(j\omega)\right) \text{ has "correct" number of encirclements} \tag{4.6}$$

The RS criteria is stated with the full range of systems: $\hat{L} = \bar{L} + \Delta \circ W_L$, with $\hat{L} \in \mathbb{C}^{C \times C}$ at an evaluated frequency. The RS criteria requires that all potential systems within the estimated uncertainty have the "correct" number of encirclements, as was the case for NS.

The RS margin is stated as simply avoidance of a potential singularity at $I + L$. The frequency-dependent stability margin, κ_{RS}, for RS is stated as the distance to violation of the determinant condition of Equation (4.6), Equation (4.7).

$$\kappa_{\text{RS}}(j\omega) := \underline{\sigma}(I + \hat{L}(j\omega)), \quad \forall \, \omega, \quad \Delta \in \mathbf{\Delta} \tag{4.7}$$

The RS condition is satisfied if κ_{RS} is sufficiently greater than zero, and if NS and the criteria for the "correct" number of encirclements is satisfied. As in the case of κ_{NS}, the loop-function dependency can be replaced with the loop-sensitivity function, Equation (4.8).

$$\kappa_{\text{RS}}(j\omega) = \frac{1}{\bar{\sigma}(\hat{S}(j\omega))}, \quad \forall \, \omega, \quad \Delta \in \mathbf{\Delta} \tag{4.8}$$

The RS margin is stated for the full range of systems in the estimate: $\hat{S} = \bar{S} + \Delta \circ W_S$, with estimates $\hat{S} \in \mathbb{C}^{C \times C}$ and $W_S \in \mathbb{R}^{C \times C}$ at any evaluated frequency. The perturbation matrix, Δ, is bounded to have magnitude less than unity at any set of evaluated frequencies as defined in Equation (4.2).

A conservative approach for estimation of the RS margin using an unstructured perturbation is presented first, followed by a less conservative structured approach. The unstructured robust margin, $\kappa_{\text{RS}_\text{U}}$, is derived as a worst-case condition, Equation (4.9).

$$\kappa_{\text{RS}_\text{U}}(j\omega) = \frac{1}{\bar{\sigma}(\bar{S}(j\omega)) + C \, \bar{\sigma}(W_S(j\omega))}, \quad \forall \, \omega, \quad \Delta \in \mathbf{\Delta} \tag{4.9}$$

The derivation of Equation (4.9) makes use of Fan's Theorem for singular value addition, Definition B.6. Note that Fan's Theorem introduces conservatism, namely:

$\bar{\sigma}(\bar{S}) + \bar{\sigma}(\Delta \circ W_S) \geq \bar{\sigma}(\bar{S} + \Delta \circ W_S)$. The final step of the derivation uses the magnitude bound definition for Δ and applies it in the worst-case direction, as $\bar{\sigma}(\Delta) = C$; this also introduces conservatism, $C \ \bar{\sigma}(W_S) \geq \bar{\sigma}(\Delta \circ W_S)$).

A less conservative RS margin follows directly from Equation (4.8). The structured RS margin, $\kappa_{\text{RS}_\text{S}}$ in Equation (4.10), preserves the structure of the nominal and uncertain components of the system.

$$\kappa_{\text{RS}_\text{S}}(j\omega) = \frac{1}{\bar{\sigma}(\bar{S}(j\omega) + \Delta \circ W_S(j\omega))}, \quad \forall \, \omega \tag{4.10}$$

The structured RS margin is solved numerically by maximizing $\bar{\sigma}(\hat{S})$ at each evaluated frequency, which is equivalent to minimizing $\kappa_{\text{RS}_\text{S}}$. The optimization is stated in Equation (4.11).

$$\begin{aligned} \text{Maximize:} \quad & \frac{1}{\kappa_{\text{RS}_\text{S}}} = \bar{\sigma}(\bar{S}(j\omega) + \Delta(j\omega) \circ W_S(j\omega)) \\ \text{Subject to:} \quad & -1 \leq |\Delta(j\omega)| \leq 1 \end{aligned} \tag{4.11}$$

Simple bounds on Δ are realized as a limit on the magnitude, $-1 \leq |\Delta| \leq 1$, and allowing the angle of the perturbation to change unconstrained, $-\infty \leq \angle\Delta \leq \infty$. The optimization yields the structured margin, $\kappa_{\text{RS}_\text{S}}$, and the corresponding worst-case perturbation matrix, Δ_{wc}, at each evaluated frequency. For examples in this study, the optimization is solved via the "L-BFGS-B" algorithm [45].

The NS and RS margins have the relation; $\kappa_{\text{RS}_\text{U}} \leq \kappa_{\text{RS}_\text{S}} \leq \kappa_{\text{NS}}$.

Definition of the RS margins has neglected the requirement that the loop function contains the "correct" number of encirclements, Equation (4.6). Unfortunately, this is a challenging criterion to assess numerically or to devise a usable stability metric using estimated frequency responses. Satisfaction of a minimum robust stability margin ensures that any change in the number of encirclements of the origin would need to occur outside the radius of the margin. Satisfaction of the NS condition and sufficient RS margin precludes the possibility of a change in the number of encirclements within the range of the estimate. A notable exception are cases in which a nonlinearity results in limited growth in the time domain; limit-cycle oscillations (LCO) are a common example of limited growth with such nonlinear responses. These nonlinearities can not be assessed adequately with the stability criteria for LTI systems as presented here.

4.3   SISO Stability

The SISO stability here is limited to assessment of a SISO vector margin. The MIMO stability conditions were specified in terms of the loop-function, $\bar{L}$ and W_L, the stability margin were derived in terms of only the sensitivity function, $\bar{S}$ and W_S, without significant compromises. As noted previously, the FRE will result in estimates of $\bar{T}$ and W_T, which can be trivially transformed into $\bar{S}$ and W_S. The nominal loop function is easily obtained from the nominal sensitivity function: $\bar{L} = \bar{S}^{-1} - I$; however, estimation of W_L, such that the bound condition on Δ is preserved, is not straightforward.

The SISO NS and RS criteria and margin definitions are analogous to the MIMO cases; again NST criteria are the basis. The stability criteria for SISO analysis is based on the condition that: $\bar{L} \neq -1 + 0j$ for each loop function input and output pair, i and o, Equation (4.12).

$$\text{NS} \iff \bar{L}_{i \to o}(j\omega) \neq -1 + 0j, \quad \forall\, \omega$$
$$\forall\, (i,o) \in \{1, 2, \dots, C\} \tag{4.12}$$
$$\text{and:} \quad \bar{L}_{i \to o}(j\omega) \text{ has the "correct" encirclements of } -1 + 0j$$

The vector margin for the nominal system stability focuses on the quantifiable magnitude of the vector from $-1 + 0j$ to $\bar{L}$ in the complex plane as a measure of "distance" to the condition $\bar{L} = -1 + 0j$. The SISO margins are assessed independently for each input and output pair, Equation (4.13).

$$\kappa_{NS_{i \to o}}(j\omega) := |\bar{L}_{i \to o}(j\omega) - -1 + 0j|$$
$$\forall\, \omega, \quad (i,o) \in \{1, 2, \dots, C\} \tag{4.13}$$

If the nominal loop-function $\bar{L}$ is known, the vector margin is directly computed from the definition in Equation (4.13). As stated previously, the sensitivity function is readily accessible from estimates; the vector margin is then determined by transforming the nominal sensitivity function to the nominal loop function: $\bar{L} = \bar{S}^{-1} - I$.

The RS condition for loop-at-a-time stability assessment requires the nominal and uncertain loop function estimates, $\bar{L}$ and W_L. The RS condition is similar to the prior MIMO RS condition, Equation (4.14).

$$\text{RS} \quad \Leftrightarrow \hat{L}_{i \to o}(j\omega) \neq \text{-}1 + 0j, \quad \forall \, \omega, \, \Delta \in \boldsymbol{\Delta}, \text{NS}$$

$$\forall \, (i,o) \in \{1, 2, \ldots, C\} \tag{4.14}$$

$$\text{and:} \quad \hat{L}_{i \to o}(s) \text{ has the ``correct'' encirclements of -}1 + 0j$$

The SISO stability margin for the uncertain system, κ_{RS}, is the "distance" measure to the condition $\hat{L} = \text{-}1 + 0j$, for each input and output pair, Equation (4.15).

$$\kappa_{RS_{i \to o}}(j\omega) := |\hat{L}_{i \to o}(j\omega) - \text{-}1 + 0j|$$

$$\forall \, \omega, \quad (i,o) \in \{1, 2, \ldots, C\} \tag{4.15}$$

The robust margin is computed with the worst-case perturbation, Δ_{wc}. However, the transformation to yield W_L requires a nonlinear transformation. Several approaches to achieve this nonlinear transformation were compared by Lichter [26], including an analytic stochastic approach as well as Monte Carlo and unscented transform sampling approaches. These approaches appear to be useful in determining a scalar stability margin, such as gain or phase margins; application to yield vector margins at all the evaluated frequencies yields erratic behavior, particularly as $\hat{L}$ nears the singularity at $\text{-}1 + 0j$.

The intent here will be to present the SISO NS vector margin and the particular perturbation attained via the MIMO structured RS margin analysis. This worst-case condition allows determination of the critical input-output pair that is driving the MIMO structured RS margin.

4.4   Estimation for Stability

The stability analysis presented is largely predicated on knowledge of the loop transfer functions: $L_o(s)$ and $L_i(s)$. Loop function estimates for a closed-loop MIMO system are derived for both the input and output loop functions. Here the derivations are provided only for the 1DOF controller architecture; an extension to a 2DOF controller architecture is straightforward and a specific example using a 2DOF controller is provided in Chapter 5.

The derivation and results of Section 4.4.1 apply an excitation at u and estimates the input stability margins. The derivation and results of Section 4.4.2 apply an excitation

at e; the output stability margins are estimated. An example, using an excitation at u, is presented in Section 4.5.

4.4.1   Control Excitation for Input Stability

For multi-input multi-output (MIMO) stability analysis, the desired form of the return difference matrix (RDM) at signal u is the inverse of the input sensitivity function, $S_i^{-1} = I + L_i$.

The RDM at signal u is determined by adding an excitation, u_{ex}, after signal u, shown in Figure 4.2, and evaluating the return response back to u.
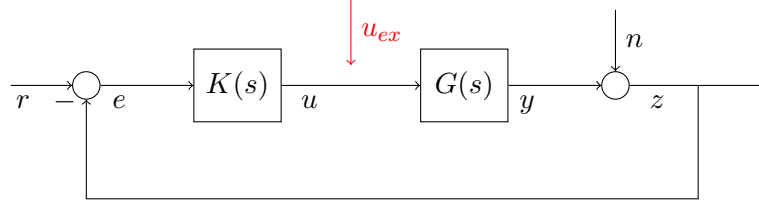
Figure 4.2: System block diagram with excitation injection at signal u_{ex}.

Signals u_{ex}, u, r, e, and z are available measures; signals n and y are not measured, and systems K and G are unknown. Equation (4.16) depicts the response of u from the excitation, u_{ex}, and external inputs, n and r.

$$u = K(s)[r - n] - K(s)G(s)[u + u_{ex}] \qquad (4.16)$$

The closed-loop response function is provided in Equation (4.17).

$$u = (I + K(s)G(s))^{-1}K(s)[r - n] - (I + K(s)G(s))^{-1}K(s)G(s)u_{ex} \qquad (4.17)$$

The external input signal, r, could be measured and accounted in Equation (4.17); however it is coupled with the controller, $K(s)$, which is assumed unknown. The external input signal may generally be correlated as well, further motivating its inclusion as uncertainty. Therefore, the external inputs r and n will be combined in the uncertain components. It follows that additional disturbances, such as disturbances acting at the plant input and within the plant itself, can be accommodated without loss of generality.

The channels of u_{ex} are composed by multichannel excitations at frequencies Ω_E. At the null frequencies, all the response power is originating from signals r and n. From Equation (4.17), if the response is evaluated only at the null frequencies, the power content of u_{ex} is zero (any estimated power would be the result of numerical error and spectral leakage). The resulting equation lumps together the two sources of disturbance and the loop sensitivity function, Equation (4.18).

$$u_N = (I + K(s)G(s))^{-1}K(s)[r - n] \tag{4.18}$$

The time-series of the null input, u_N, is not measured, however its auto-spectra, $\Phi_{uu}(\Omega_N)$, can be estimated at the null frequencies.

Equation (4.17) can then be written with the input complementary sensitivity function, Equation (4.19).

$$u = -T_i(s)\ u_{ex} + u_N \tag{4.19}$$

Inspection of Equation (4.19) shows a clear partition into components associated with the excitation return and null components.

Equation (4.20) partitions Equation (4.19) into an estimated nominal component, $\bar{T}_i$, and an estimated uncertain component, W_{T_i}, that captures both the "best" estimate and the estimation error. Perturbations of the uncertainty are complex, $\Delta \in \mathbb{C}^{C \times C}$, constrained to $||\Delta||_{max} \leq 1$.

$$\hat{T}_i(s) = \bar{T}_i(s) + \Delta(s) \circ W_{T_i}(s) \tag{4.20}$$

Equation (4.21) shows the response function; here the response is computed with input u_{ex} and output u, where $\Phi_{u_{ex} \to u}$ represents the cross-spectra from u_{ex} to u.

$$\bar{T}_i(s) \mathrel{\hat{=}} \mathrm{E}_L[\hat{\Theta}_{u_{ex} \to u}[\Omega_E]] = \mathrm{E}_L\left[\frac{\hat{\Phi}_{u_{ex} \to u}[\Omega_E]}{\hat{\Phi}_{u_{ex}u_{ex}}[\Omega_E]}\right] \tag{4.21}$$

The resulting square, complex-valued transfer matrix has dimensions corresponding to the number of excitation channels, C, as: $\bar{T}_i[\omega] \in \mathbb{C}^{C \times C}$ for all evaluated frequencies $\omega \in \Omega_E$. The uncertainty is estimated using the spectra of u_{ex} and u in both the excited frequency set and the null set, Equation (4.22).

$$W_{T_i}(s) \,\hat{=}\, \left[(1 - \frac{1}{\sqrt{L}})\varepsilon_t + \frac{1}{\sqrt{L}}\right] \mathrm{E}_L[\dot{\Theta}_d + \dot{\Theta}_w] \qquad (4.22)$$

$$\text{where: } \varepsilon_t = \frac{\sqrt{\mathrm{Var}_L[\tilde{\Phi}_{uu}[\Omega_E]]}}{\bar{\Phi}_{uu}[\Omega_E]}$$

$$\text{and: } \dot{\Theta}_d = \sqrt{\frac{\tilde{\Phi}_{uu}[\Omega_N]|_{\Omega_E}}{\tilde{\Phi}_{u_{ex}u_{ex}}[\Omega_E]}}$$

$$\text{and: } \dot{\Theta}_w = |W| \; \dot{\Theta}_d$$

The uncertainty matrix is real-valued, representing the magnitude of the uncertainty, $W_{T_i}[\omega] \in \mathbb{R}^{C \times C}$ for all evaluated frequencies $\omega \in \Omega_E$. Leakage in Equation (4.22) is accounted by the approximation of the window function, $|W|$.

Estimation of the sensitivity function estimate follows a similar approach as described for the complementary sensitivity function estimate, Equation (4.23).

$$\hat{S}_i(s) = \bar{S}_i(s) + \Delta(s) \circ W_{S_i}(s) \qquad (4.23)$$

The sensitivity function can be computed via a simple relation from the complementary sensitivity function, by noting that $S_i = I - T_i$. Alternatively, the sensitivity function can be estimated more directly by noting that $\Theta_{u_{ex} \to [u_{ex}+u]} = I + \Theta_{u_{ex} \to u}$, in Equation (4.24).

$$\bar{S}_i(s) \,\hat{=}\, \mathrm{E}_L[\hat{\Theta}_{u_{ex} \to [u+u_{ex}]}[\Omega_E]] \qquad (4.24)$$

The magnitude of the sensitivity function uncertainty is the same as the magnitude of the complementary sensitivity function uncertainty, Equation (4.25).

$$|W_{S_i}(s)| = |W_{T_i}(s)| \qquad (4.25)$$

Again, the nominal estimate is a complex-valued matrix, $\bar{S}_i \in \mathbb{C}^{C \times C}$, and the uncertainty estimate is a real-valued matrix, $W_{S_i} \in \mathbb{R}^{C \times C}$, for all evaluated frequencies.

Following estimation of $\bar{S}_i(s)$ and $W_{S_i}(s)$, the MIMO NS and RS margins can be readily computed: Equation (4.5), Equation (4.8), and Equation (4.10). SISO vector margins for the nominal system computed from Equation (4.13); and application of the

worst-case MIMO result is computed from Equation (4.15).

The complementary sensitivity function and sensitivity function estimates can be rederived in terms of the Signal-to-Noise-Ratio (SNR) of the signals. An alternative form for determining uncertainty can utilize the SNR estimate directly, as discussed Chapter 2, rather than the input-output form presented here. The SNR approach lends itself well to treating the estimation error as a multiplicative output uncertainty.

4.4.2 Reference Command Excitation for Output Stability

Estimation of the closed-loop response follows a similar derivation as the previous stability analysis. For the closed-loop response, the desired system is the output complementary sensitivity function (Table 4.1). The reference input is augmented with an excitation signal, r_{ex}, as shown in Figure 4.3.
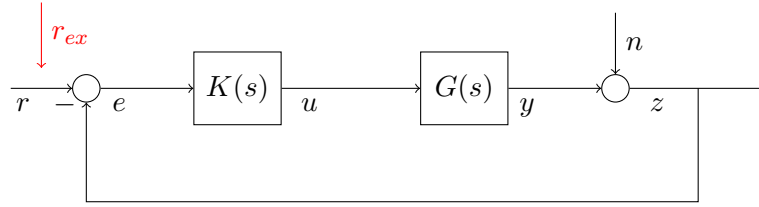
Figure 4.3: System block diagram with excitation injection at signal r

Estimation of the desired system can be realized through expanding the closed-loop response at the measured output signal, z, shown in Equation (4.26).

$$z = (I + G(s)K(s))^{-1}[n + G(s)K(s)\ r] + (I + G(s)K(s))^{-1}G(s)K(s)\ r_{ex} \qquad (4.26)$$

Grouping the disturbance signal, n, and the reference input, r, into an uncorrelated null signal is shown in Equation (4.27).

$$z_N = (I + G(s)K(s))^{-1}[n + G(s)K(s)\ r] \qquad (4.27)$$

The desired form of the complementary sensitivity function is again: $\hat{T} = \bar{T} + \Delta \circ W_T$.

The nominal component is estimated from the constituent spectra of r_{ex} and z in the excited frequency set, Ω_E, as: $\bar{T}_o$ in Equation (4.28).

$$\bar{T}_o(s) \mathrel{\hat{=}} \mathrm{E}_L[\hat{\Theta}_{r_{ex} \to z}[\Omega_E]] \tag{4.28}$$

The uncertain component is estimated from the constituent spectra of r_{ex} in the excited frequency set and z in both the excited frequency set and the null frequency set, Ω_N as: W_{T_o} in Equation (4.29).

$$W_{T_o}(s) \mathrel{\hat{=}} \left[(1 - \frac{1}{\sqrt{L}})\varepsilon_t + \frac{1}{\sqrt{L}}\right] \mathrm{E}_L[\grave{\Theta}_d + \grave{\Theta}_w] \tag{4.29}$$

$$\text{where: } \varepsilon_t = \frac{\sqrt{\mathrm{Var}_L[\tilde{\Phi}_{zz}[\Omega_E]]}}{\bar{\bar{\Phi}}_{zz}[\Omega_E]}$$

$$\text{and: } \grave{\Theta}_d = \sqrt{\frac{\tilde{\Phi}_{zz}[\Omega_N]|_{\Omega_E}}{\tilde{\Phi}_{r_{ex}r_{ex}}[\Omega_E]}}$$

$$\text{and: } \grave{\Theta}_w = |W| \; \grave{\Theta}_d$$

Transformation of $\hat{T}_o$ to $\hat{S}_o$ and stability assessment follows as in Section 4.4.1.

The sensitivity function can be computed via a simple relation from the complementary sensitivity function, by noting $S_o = I - T_o$. Alternatively, the sensitivity function can be estimated more directly by noting that $\Theta_{r_{ex} \to [r_{ex}+z]} = I + \Theta_{r_{ex} \to z}$, in Equation (4.30).

$$\bar{S}_o(s) \mathrel{\hat{=}} \mathrm{E}_L[\hat{\Theta}_{r_{ex} \to [z+r_{ex}]}[\Omega_E]] \tag{4.30}$$

The magnitude of the sensitivity function uncertainty is the same as the magnitude of the complementary sensitivity function uncertainty, Equation (4.31).

$$|W_{S_o}(s)| = |W_{T_o}(s)| \tag{4.31}$$

As in the input case, the output complementary sensitivity function and output sensitivity function estimates can be specified in terms of the Signal-to-Noise-Ratio (SNR) of the signals.

4.5 Closed-Loop MIMO FRE Example

The MIMO example problem of Section 2.4 and Section 3.6 is further developed with a compensator, $K(s)$, in a closed-loop system depicted in Figure 4.4. The compensator operates on the error, e, between a reference command, r, and the measured output, z.
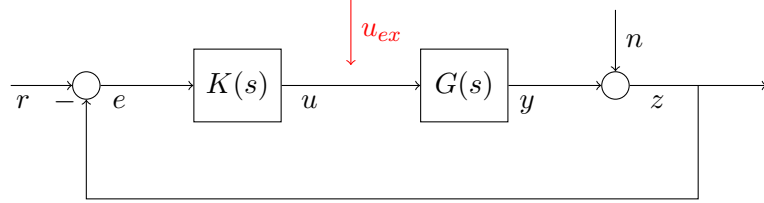
Figure 4.4: System block diagram with excitation injection at signal u.

An excitation signal, u_{ex}, is depicted in Figure 4.4 as injecting onto the control command signal, u.

The compensator is defined as a block matrix in Equation (4.32) along with the block element transfer function and parameterization in Table 4.2.

$$\begin{bmatrix} u_1 \\ u_2 \end{bmatrix} = \begin{bmatrix} K_{11}(s) & K_{12}(s) \\ K_{21}(s) & K_{22}(s) \end{bmatrix} \begin{bmatrix} e_1 \\ e_2 \end{bmatrix} \tag{4.32}$$

Table 4.2:   Controller system definitions.

Component	Parameterization	Transfer Function
$K_{11}(s)$	$k = 0.75$ $\tau = 0.053$ sec	$k\, \dfrac{1}{\tau s + 1}$
$K_{12}(s)$	$k = 0.25$ $\tau = 0.053$ sec	$k\, \dfrac{1}{\tau s + 1}$
$K_{21}(s)$	$k = 0.25$ $\tau = 0.053$ sec	$k\, \dfrac{1}{\tau s + 1}$
$K_{22}(s)$	$k = 0.50$ $\tau = 0.053$ sec	$k\, \dfrac{1}{\tau s + 1}$

The gains of the compensator were selected to bring the Nyquist plot of L_{11} close to the critical point; no other performance or stability criteria were used to tune the compensators. The first-order filters, characterized by τ in Table 4.2, have a cutoff at 3 Hz to attenuate high-frequency content; namely, the low damped disturbance at 6 Hz.

The excitation definition from Section 3.6 is again used for this example. The derivations of Section 4.4.1 are directly applicable for this example.

First, the estimate of the complementary sensitivity function, T_i, is compared to the model in Figure 4.5 through Figure 4.8.
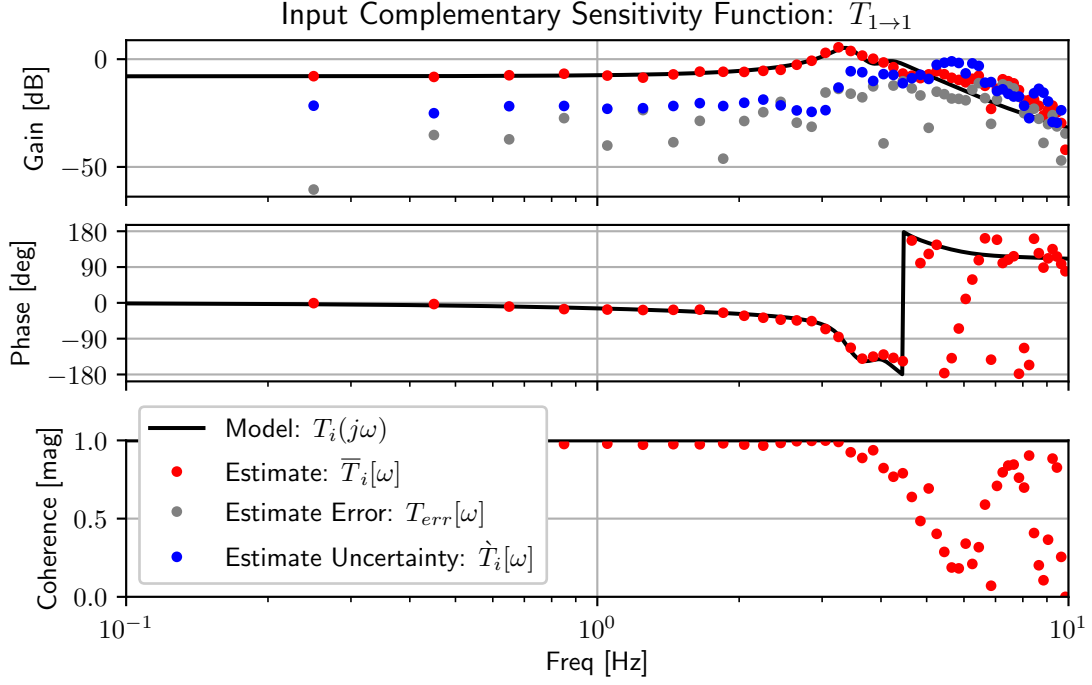
Figure 4.5: Bode plot of T_i for $u_{ex}[1]$ to $u[1]$ with the linear model, nominal estimate, estimate error, and estimated uncertainty.
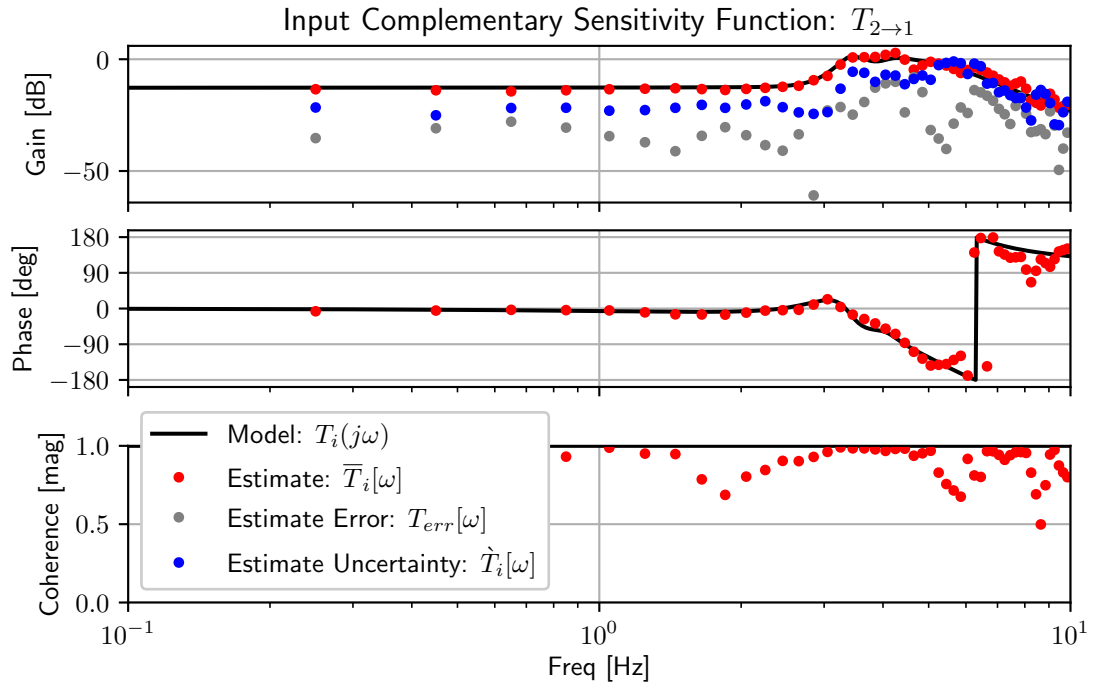
Figure 4.6: Bode plot of T_i for $u_{ex}[2]$ to $u[1]$ with the linear model, nominal estimate, estimate error, and estimated uncertainty.
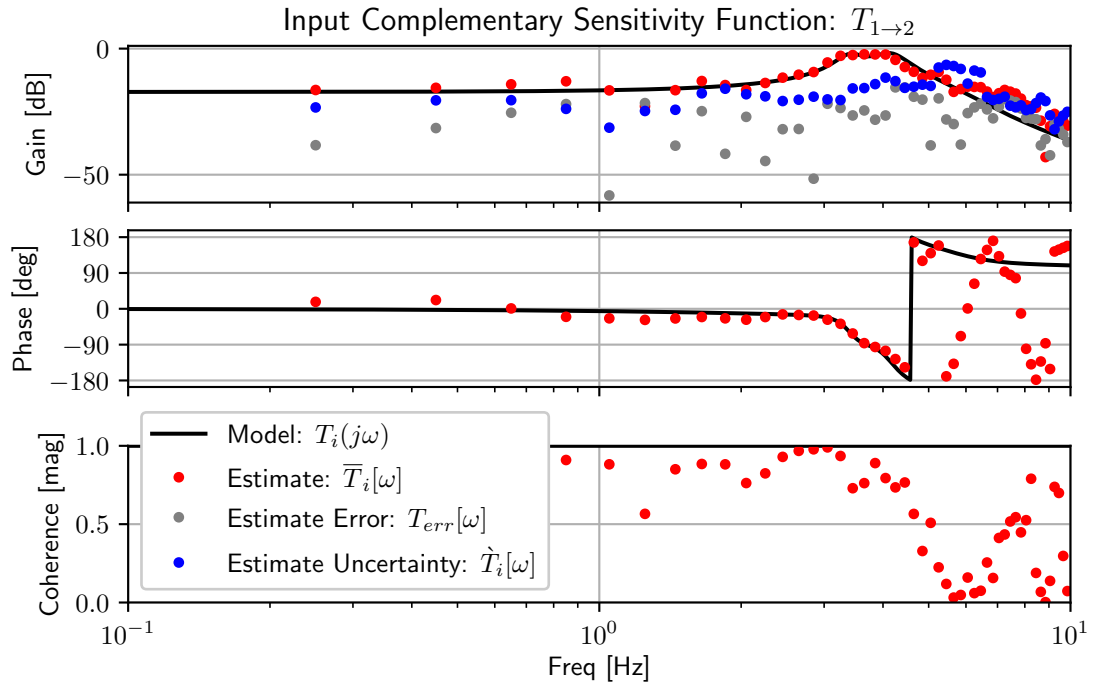
Figure 4.7: Bode plot of T_i for $u_{ex}[1]$ to $u[2]$ with the linear model, nominal estimate, estimate error, and estimated uncertainty.
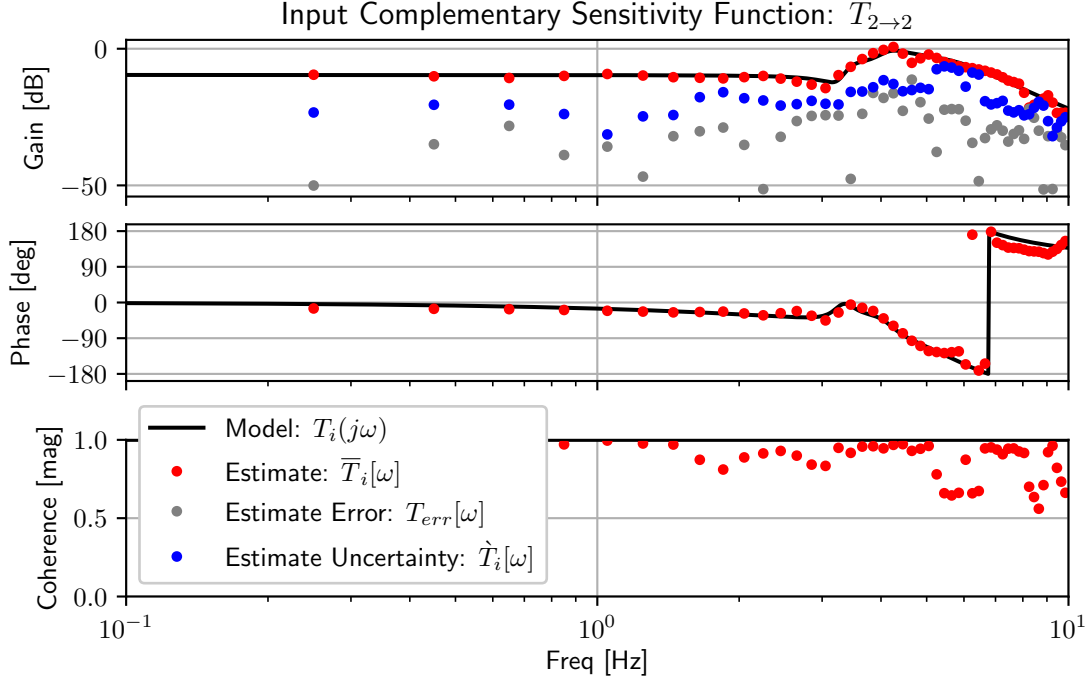
Figure 4.8: Bode plot of T_i for $u_{ex}[2]$ to $u[2]$ with the linear model, nominal estimate, estimate error, and estimated uncertainty.

Again, the nominal estimates generally follow the linear model. The low-damped disturbance at 6 Hz is now apparent in all four figures as a result of the cross-coupling introduced by closure of the feedback loop (the 6 Hz disturbance originates with z_2 and is apparent in the spectra of u_1 and u_2). The erratic appearance of the phase angle is due to high sensitivity in the angle computation at small gain values (in some instances this results in incorrect "unwrapping" of the phase angle).

The estimation error and uncertainty are isolated from Figure 4.5 to highlight the comparison in Figure 4.9. The uncertainty in Figure 4.9 generally over bounds the estimation error, and is conservative in 74.5% of cases amongst the 4 input-output pairs.
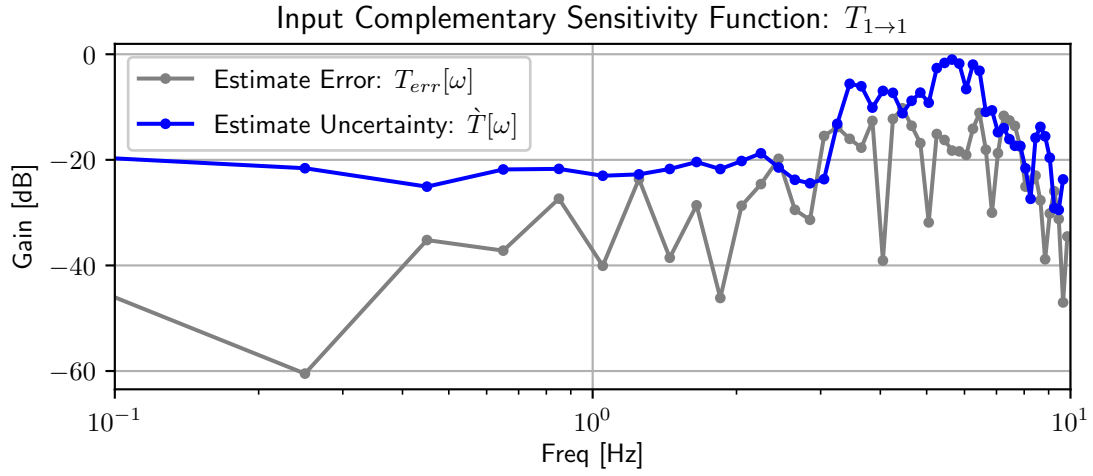
Figure 4.9: Gain plot of T_i for $u_{ex}[1]$ to $u[1]$ highlighting the estimation error and uncertainty estimate.

The sensitivity function $\hat{S}_i$ is computed from $\hat{T}_i$ with the simple relations: $\bar{S}_i = I - \bar{T}_i$ and $|W_{S_i}| = |W_{T_i}|$. The MIMO stability margins are depicted for the linear model and estimated system in Figure 4.10.
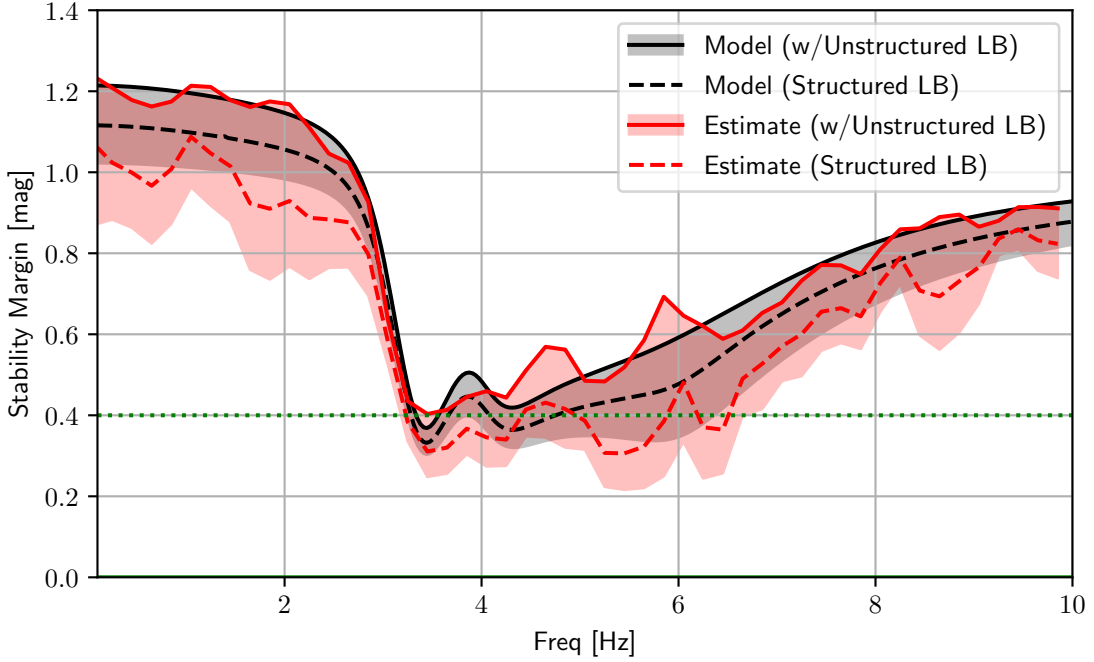
Figure 4.10: MIMO stability margin plot of $\hat{S}_i$, nominal estimate stability margin with structured stability margin lower bounds; κ_{NS} depicted as solid lines, $\kappa_{\mathrm{RS_U}}$ is the lower bound of the shaded regions, and $\kappa_{\mathrm{RS_S}}$ is depicted as the dashed lines.

In general, the estimated nominal system follows the linear model's nominal margin. The model has a minimum NS margin of 0.37 at 3.45 Hz; the estimate has a minimum of 0.40 at 3.45 Hz. The unstructured and structured robust margin of the estimate is slightly lower than linear model robust margin nearly everywhere. The most significant difference is in the low frequency range, below about 3 Hz, where the unstructured and structured uncertainty is larger than that of the linear model. The linear model has both unstructured and structured minimum margins at 3.45 Hz (0.30 and 0.33), the estimate has minimum margins at 5.45 Hz (0.21 and 0.31).

The SISO vector margins for the linear model and estimate for the first input-output pair is shown in Figure 4.11.
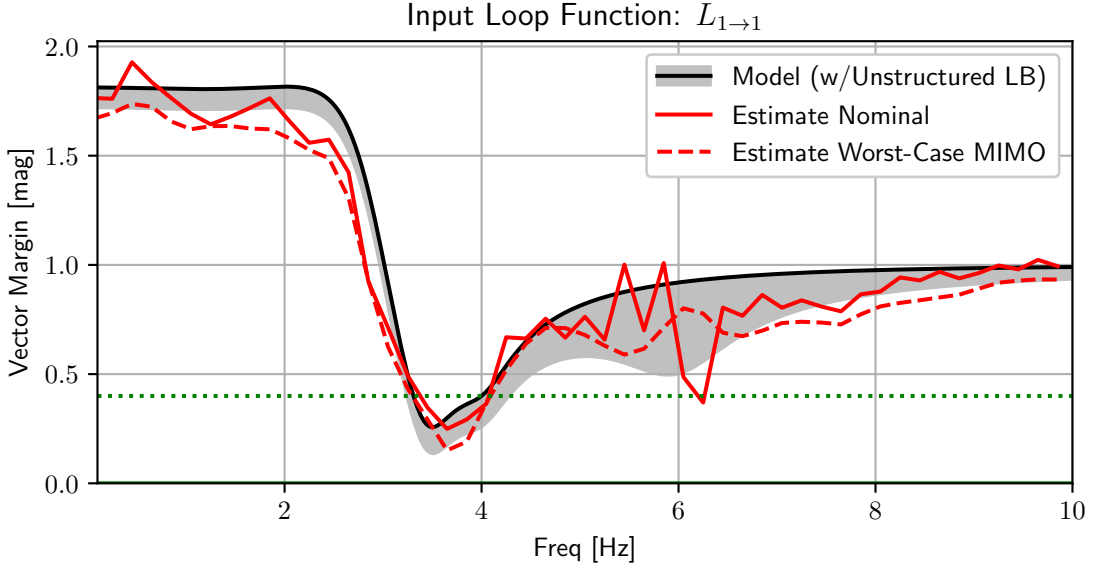
Figure 4.11: Vector Margin plot of L_i for $u_{ex}[1]$ to $u[1]$ with the linear model with nominal and lower uncertainty bound and the nominal estimated model and worst-case perturbation that yielded $\kappa_{\mathrm{RS_S}}$.

The estimated vector margins are generally more sensitive to disturbances, showing more significant variation than the MIMO margin estimates. The estimates yield a minimum nominal vector margin of 0.25 at 3.65 Hz. In this case, the estimated system indicates that the MIMO worst-case perturbation yields a vector margin of 0.15 at 3.65 Hz. Inspection of the three other vector margin plots reveals that this is the critical loop that results in both the minimum vector margins.

This series of examples has focused specifically on capturing disturbances originating at the plant output, n. The only prior knowledge incorporated in these examples was to establish the frequency range of interest for the excitation generation. The disturbance and plant models were specified such that the disturbances dominated the response models at a wide range of frequencies and in multiple channels. This example shows that the disturbances in the system are captured and appropriately propagated to robust stability margin assessment of a closed-loop multivariate system.

Chapter 5

Application for Aircraft Stability Assessment

The FRE method and stability estimation techniques are demonstrated for a small, fixed-wing unmanned aerial vehicle (UAV). In Section 5.1 the linear aircraft model is described. The aircraft response is simulated with a multisine excitation and the frequency response functions are estimated along with the stability margins. The results from the FRE are compared to analytic results from the linear plant and controller.

Section 5.2 describes the flight experimentation, then provides some results and findings based on the experiments.

The test aircraft is based on a small hobby airframe known as an UltraStick 25e (formerly produced by E-flite as model EFL4025). Table 5.1 contains a brief summary of aircraft characteristics.

Table 5.1: General dimensions and properties of the UltraStick 25e.

Properties	Value
Wing Span	1.27 m
Wing Reference Area	0.31 m^2
Mass	1.96 kg
Actuation Bandwidth	6 Hz
Propulsion Bandwidth	2 Hz

The particular UltraStick 25e used in this study is named Thor. This particular airframe was also employed in the context of small aircraft system identification in 2013 and is described by Dorobantu [46]. In the ensuing years, many of the aircraft's flight systems have been replaced. The flight system used in this study was developed specifically for a larger and more complicated aircraft; mAEWing2, which was designed as an aeroelastic research aircraft. Thor was modified to be a flight system test bed for the mAEWing2 aircraft in order to test the hardware and software architecture. The general hardware and software architecture for mAEWing2 has been previously documented [42, 47]. A complete description of the aircraft flight systems is unnecessary, since there is no effort in this study to isolate either the plant or controller model from the closed-loop response. Rather, the plant model is only used to determine the excitation frequency range and is otherwise treated as an unknown.

A simplified block diagram of the aircraft system is shown in Figure 5.1.
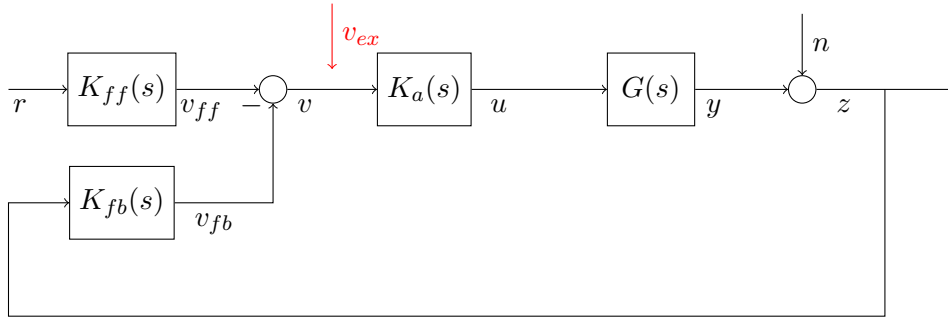
Figure 5.1: System block diagram, 2DOF, with excitation injection at signal v

The plant model, G, will be a linear model in Section 5.1 and a physical aircraft in Section 5.2. The control system is modeled as a 2DOF system, with independent linear models for the reference signal ($v_{\text{ff}} = K_{\text{ff}}\, r$) and feedback signal ($v_{\text{fb}} = K_{\text{fb}}\, z$). A linear control allocation mixer, K_a, distributes the virtual control commands (such as: "roll rate", "pitch rate", etc.), v, to the physical commands (such as: "elevator deflection", "rudder deflection", etc.).

The control system can be written as: $u = K_a(K_{\text{ff}}\, r - K_{\text{fb}}\, z)$. An excitation signal, v_{ex}, is applied to the virtual command, v, which results in the excited control system equation Equation (5.1).

$$u = K_a(K_{\text{ff}} \ r - K_{\text{fb}} \ z + v_{ex}) \hspace{2cm} (5.1)$$

The loop function that arises at the virtual command, v, from the 2DOF control architecture will be referred to as the "allocator loop". Previously, Table 4.1 distinguished loop functions as "input" and "output"; Table 5.2 augments those definitions with definitions pertaining to the allocator loop.

Table 5.2:   Allocator Loop transfer function definitions.

Loop Function Name	Loop Function Equation
Allocator Loop Transfer Functions	$L_a(s) = K_a(s)G(s)K_{\text{fb}}(s)$
Allocator Sensitivity Function	$S_a(s) = (I + L_a(s))^{-1}$
Allocator Complimentary Sensitivity Function	$T_a(s) = (I + L_a(s))^{-1} \ L_a(s)$

As is often the case, the allocator in this study does not contain any dynamics. Therefore, the stability results derived from the "allocator loop" are closely related to the stability of the "output loop". In this particular example, u contains commands for 7 effectors, whereas there are only 3 signals in the virtual command (associated with roll, pitch, and yaw). The reduction in signal dimension (from 7 to 3) is advantageous for designing the excitation signal and for assessing the stability. For example, since the left and right ailerons are always commanded to be equal and opposite, there is no benefit to evaluate the loop functions for the left and right ailerons independently. The allocator does not contain any dynamics, so the distinction between the "allocator loop" and the "output loop" is negligible in terms of stability margin estimates.

5.1   Aircraft Stability Estimation — Linear Model

The aircraft linear plant model is used to provide a means of comparing estimation results back to the model definitions in the frequency-domain. This model presents the FRE with a slightly larger input-output dimension than previously shown (3×3 versus 2×2 used in the prior MIMO examples) and many more states in the plant model (47 versus 8).

As mentioned, the aircraft model and simulation have been developed and revised over several years. A summary of the response characteristics are provided to the extent that the detail provides insight into the excitation definition, and interpretation of the results. The dynamic modes of the bare airframe (inertia and aerodynamic) are tabulated in Table 5.3.

Table 5.3: UltraStick 25e linear bare airframe dynamic modes.

Mode Name	Pole	Natural Frequency	Damping
Phugoid	$-0.1638 \pm 0.642j$	0.105 Hz (0.662 rad/sec)	0.2472
Short Period	$-11.67 \pm 10.05j$	2.449 (15.39 rad/sec)	0.7577
Dutch Roll	$-1.856 \pm 5.27j$	0.889 Hz (5.587 rad/sec)	0.3322

The bare airframe also contains two additional real-valued poles at -6.184 and -16.05 that are principally in the lateral-directional dynamics (there are 3 additional poles with near zero magnitude). The complete state space model of the UltraStick25e plant are provided in Appendix C.

The control surfaces are actuated by HiTec HS-225BB servos. This servo was used in Section 3.4 to illustrate the impact of nonlinear response on the FRE, Table 3.2. Only the linear components of the response have been modeled, Table 5.4. The control surface actuation models are the same for all 6 surface: elevator, rudder, left and right ailerons, and left and right flaps. Note that the control surface actuation has higher bandwidth than the flight dynamics modes. The motor model is approximated as a first order model with a time constant of 79.6 milliseconds (i.e., 2 Hz). The effector models are all augmented with a time delay, $\tau_d = 0.050$ sec, modeled as: $e^{-\tau_d s}$.

Table 5.4: Actuation models for linear UltraStick25e model.

Effectors	Parameterization	Transfer Function
Control Surfaces	$\omega_n = 6.0$ Hz $\quad \zeta = 0.8$	$\dfrac{\omega_n^2}{s^2 + 2\zeta\omega_n + \omega_n^2}$
Propulsion	$\tau = 79.6$ ms	$\dfrac{1}{\tau s + 1}$

The sensor models for the UltraStick 25e are split into inertial sensors and air data

sensors. The inertial sensors measure the rotation rates of the aircraft, p, q, r, and estimate the orientation of the aircraft, ϕ, θ, ψ. Inertial sensors are all modeled with a 3.18 millisecond time constant (cutoff frequency of 50 Hz). Air data sensors are modeled with a time constant of 79.6 milliseconds (cutoff frequency of 2 Hz). The sensor models are also augmented with a pure time delay, $\tau_d = 0.050$ sec, modeled as: $e^{-\tau_d s}$.

Table 5.5:   Sensor models for linear UltraStick25e model.

Sensors	Parameterization	Transfer Function
$[p, q, r]$	$\tau = 3.18$ ms	$\dfrac{1}{\tau s + 1}$
$[\phi, \theta, \psi]$	$\tau = 3.18$ ms	$\dfrac{1}{\tau s + 1}$
$[\alpha, \beta, h]$	$\tau = 79.6$ ms	$\dfrac{1}{\tau s + 1}$

The control surfaces on this particular aircraft are not instrumented, so the actuation commands are recorded but the actual surface position (or propeller rotation rate) is not measured.

The aircraft control system is modeled in several parts. The controller operates on a 50 Hz frame rate. As noted earlier, there is a control allocation mixer that takes virtual control commands (roll rate, pitch rate, and yaw rate) and produces the individual actuator commands. An "inner-loop" controller takes the commanded bank angle (r_ϕ), attitude angle (r_θ), and yaw rate (r_r) commands as reference and produced the associated virtual control commands. The "inner-loop" takes the measured bank angle (z_ϕ), attitude angle (z_θ), and yaw rate (z_r) as feedback signals. The roll and pitch controller are 2DOF PID (proportional, integral, derivative) controllers, Equation (5.2).

$$v = k_p(b\ r - z) + \frac{k_i}{s}(r - z) + \frac{k_d\ s}{\tau_f s + 1}(c\ r - z) \tag{5.2}$$

The yaw controller is a simple first order lag to damp the yaw response, Equation (5.3).

$$v = \frac{1}{\tau s + 1} \tag{5.3}$$

Parameterization of the "inner-loop" controller is tabulated in Table 5.6.

Table 5.6:   UltraStick25e inner-loop controller definition.

Controller	Parameterization		
Bank (Roll)	$k_p = 0.64$	$k_i = 0.20$	$k_d = 0.07$
	$\tau_f = 0.02$ sec	b $= 1$	c $= 0$
Attitude (Pitch)	$k_p = 0.90$	$k_i = 0.30$	$k_d = 0.08$
	$\tau_f = 0.02$ sec	b $= 1$	c $= 0$
Yaw	$\tau_f = 5.72$		

The general 2DOF PID controller separates into a feed-forward transfer function and feedback transfer function, Equation (5.4).

$$v = K_{\text{ff}} \, r - K_{\text{fb}} \, z$$

$$K_{\text{ff}} = b \, k_p + \frac{k_i}{s} + \frac{c \, k_d \, s}{\tau_f s + 1} \tag{5.4}$$

$$K_{\text{fb}} = k_p + \frac{k_i}{s} + \frac{k_d \, s}{\tau_f s + 1}$$

The control allocation mixer is a static matrix, generated as the Moore-Penrose pseudo-inverse of the corresponding bare airframe static control effectiveness matrix, Equation (5.5).

$$u = K_a \, v$$

$$K_a = \begin{bmatrix} 0.0000 & -0.0468 & 0.3159 & -0.3159 & 0.1335 & -0.1335 \\ -0.4390 & 0.0000 & 0.0000 & 0.0000 & 0.0000 & 0.0000 \\ 0.0000 & -0.6239 & 0.0000 & 0.0000 & 0.0000 & 0.0000 \end{bmatrix}^T \tag{5.5}$$

$$\text{where: } v = [v_p, v_q, v_r]$$
$$\text{and: } u = [\delta_e, \delta_r, \delta_{aL}, \delta_{aR}, \delta_{fL}, \delta_{fR}]^T$$

The allocation matrix indicates that pitch commands allocate to the elevator, yaw commands allocate to the rudder, and roll commands allocate to the ailerons, flaps, and

rudder.

The preceding linear model is sufficient for comparison with the estimated frequency responses. Additional details of the control system implementation used on-board the aircraft will be discussed in Section 5.2.

The closed-loop linear model is excited with a multisine injected at v_{ex} with individual channels associated with roll, pitch, and yaw rotation rate commands. The three-channel multisine frequencies and phases are the same as defined in Table 2.1; where the frequency range of the excitation is 0.10 Hz to 10.10 Hz in 0.2 Hz increments. The individual excitation components all have an amplitude of 0.0144 rad/sec, which yields channel peaks near 0.1049 rad/sec (6.0 deg/sec).

Disturbances are introduced in the linear model as signal n in terms of the rotation rates, inertial orientation, and relative aerodynamics angles. Rotation rate (p, q, and r) disturbances have a standard deviation of 0.0698 rad/sec (4.0 deg/sec). Aircraft orientation (ϕ, θ, and ψ) disturbances have a standard deviation of 0.008727 rad (0.5 deg). Relative aerodynamic angle (angle-of-attack, α, and angle-of-sideslip, β) disturbances have a standard deviation of 0.008727 rad (0.5 deg).

Estimation of the complimentary sensitivity function is compared to the linear model in Figure 5.2 and Figure 5.3. Three segments of 20 seconds each (rectangular, non-overlapping windows) were used in the estimate. The estimate is generally within the estimated uncertainty range in the roll axis return function, $v_{ex}[1] \rightarrow v[1]$. The estimate is also generally within the estimated uncertainty range in the yaw axis to roll axis return function, $v_{ex}[3] \rightarrow v[1]$.
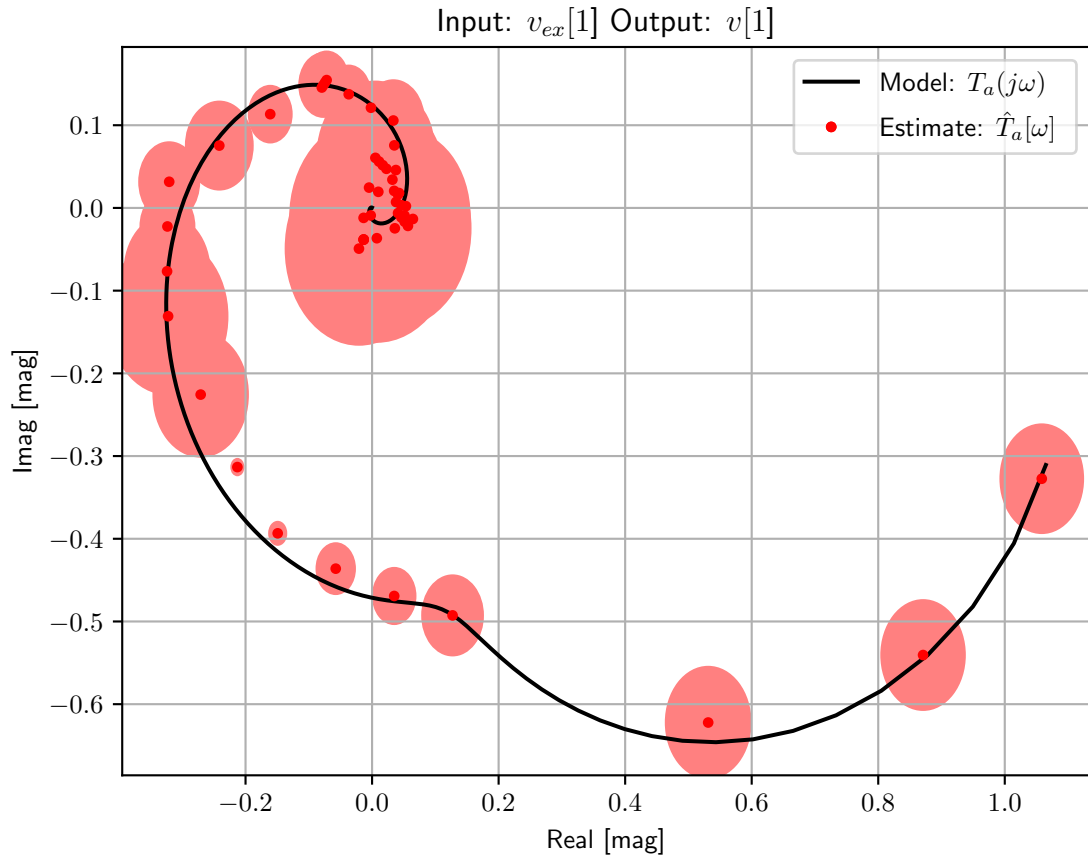
Figure 5.2: Nyquist plot of T_a for $v_{ex}[1]$ to $v[1]$ with the linear model, nominal estimate and estimated uncertainty region.
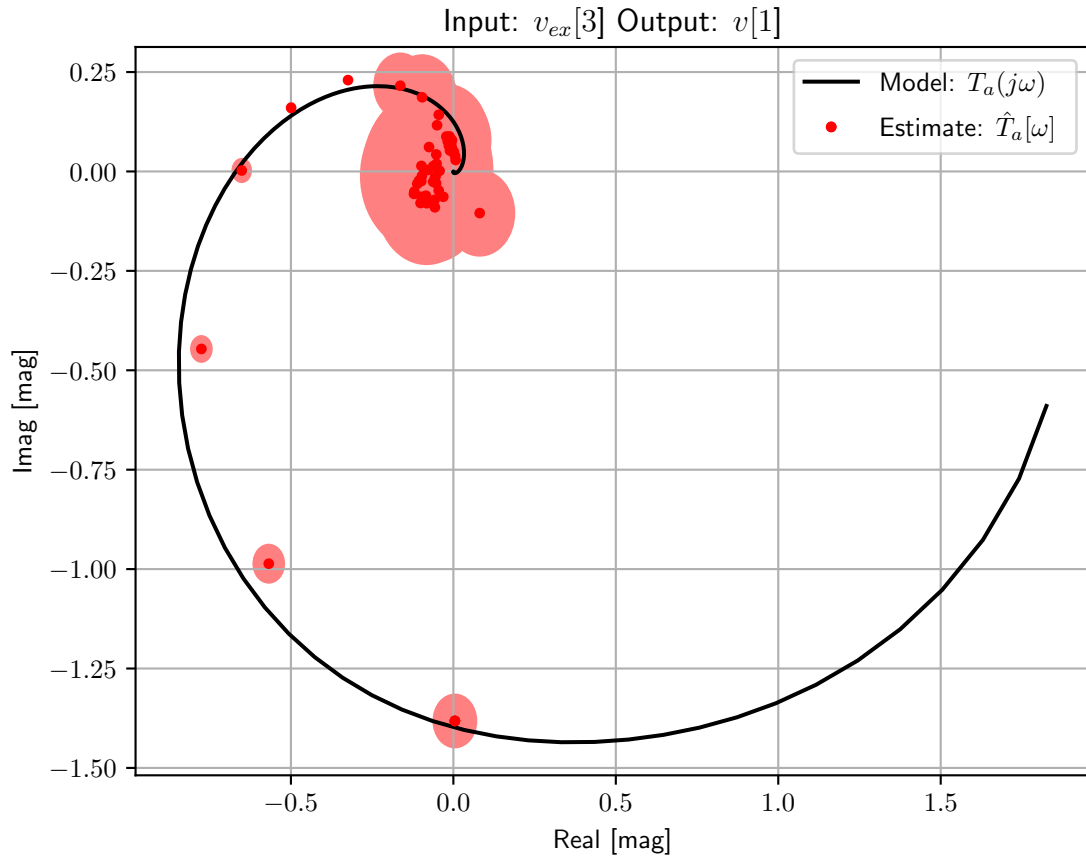
Figure 5.3: Nyquist plot of T_a for $v_{ex}[3]$ to $v[1]$ with the linear model, nominal estimate and estimated uncertainty region.

The estimates of the NS and RS margins using S_a are shown in Figure 5.4.
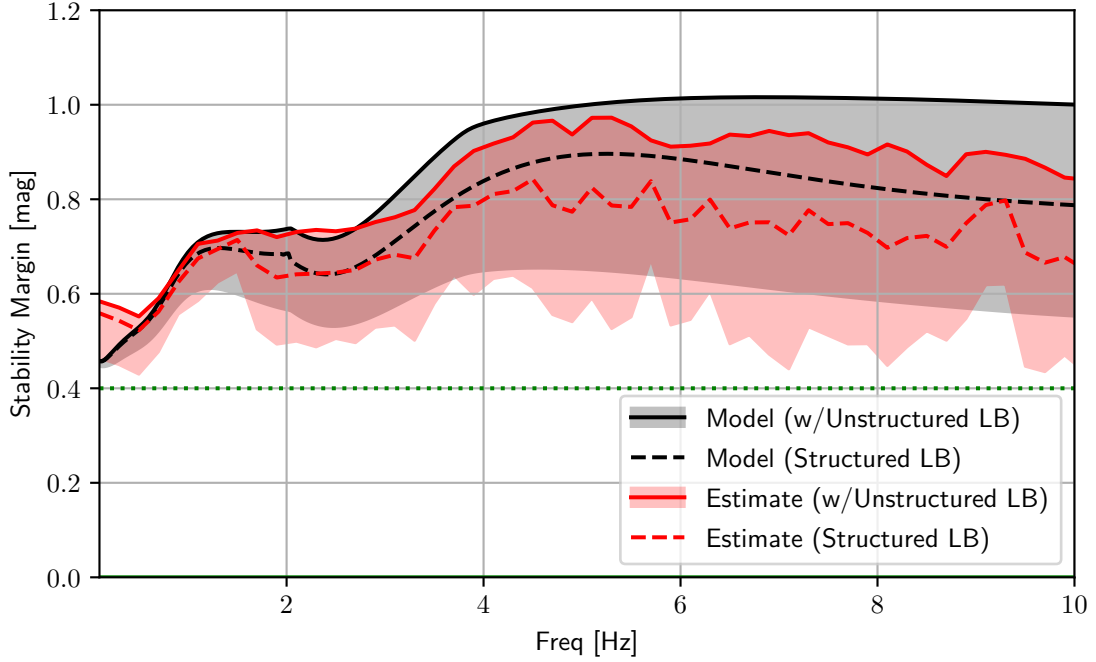
Figure 5.4: UltraStick 25e aircraft MIMO stability margins using the sensitivity function, S_a; κ_{NS} depicted as solid lines, $\kappa_{\mathrm{RS}_\mathrm{U}}$ is the lower bound of the shaded regions, and $\kappa_{\mathrm{RS}_\mathrm{S}}$ is depicted as the dashed lines.

The nominal margin estimate matches the linear model fairly well and contains the linear model margins within the uncertainty bounds of the estimate at all frequencies. The unstructured and structured RS margins also compare well at all frequencies. The NS and RS margins are all greater than 0.4, which is a typical control system design objective.

5.2   Aircraft Stability Estimation — Flight Data

A series of flight tests were conducted with a UltraStick 25e as described in Section 5.1.

The flight tests were conducted with an additional guidance-loop control law to provide guidance commands into r. The guidance controllers are all 2DOF PID controllers, Equation (5.2), with parameters listed in Table 5.7.

Table 5.7:   UltraStick25e guidance-loop controller definition.

Controller	Parameterization		
Heading	$k_p = 0.75$	$k_i = 0.15$	$k_d = 0.00$
		b = 1	c = 0
Altitude	$k_p = 0.011$	$k_i = 0.00$	$k_d = 0.01$
	$\tau_f = 0.20$ sec	b = 1	c = 0
Airspeed	$k_p = 0.20$	$k_i = 0.075$	$k_d = 0.0$
		b = 1	c = 0

The guidance law maintains the aircraft in a large loiter circle (with 200 meter radius) and attempts to hold airspeed and altitude (17 m/s and 75 meters above ground level). The airspeed hold controller uses the measured airspeed, V, from the aircraft's pitot static system as feedback to compute a throttle command, δ_t. The altitude hold controller uses the measured barometric altitude, h, from the aircraft's pitot static system as feedback to compute a reference attitude command for the inner-loop controller, r_θ.

The heading controller computes a desired bank angle, r_ϕ for the inner-loop controller, based on the current heading ψ and a targeted heading, ψ_{target}. The targeted heading consists of the path's local heading, ψ_{path}, and a cross track error to the local path, d_x: $\psi_{\text{target}} = \psi_{\text{path}} + k_x \ d_x$, where $k_x = \frac{\pi}{4}$, and d_x is a distance normalized with the loiter circle radius and limited to be less than unity: $|d_x| \leq 1$. The gains for the heading controller were specified for application to the mAEWing2 aircraft; and were deemed sufficient for testing with Thor.

Four flight test segments from Thor flight #128 will be used for this study [48]. The range of times in the flight data and the excitation amplitudes are tabulated in Table 5.8.

Table 5.8:   Thor flight #128 test segments.

Test #	Time Range	Excitation Amplitude
Test 1	714.4 to 746.4 seconds	4 deg/sec
Test 2	847.3 to 879.3 seconds	4 deg/sec
Test 3	794.3 to 826.3 seconds	8 deg/sec
Test 4	921.4 to 953.4 seconds	8 deg/sec

Tests were conducted with two multisine excitation amplitudes; yielding channel peak amplitudes of 4 and 8 deg/sec. Each excitation in this series consists of 3 repeats of a 10 second multisine excitation for a total duration of 30 seconds. The excitation definitions were generated as an optimal multisine, rather than the Schroeder multisines used previously, for the flight test, spanning the frequency range from 0.1 Hz to 10 Hz, in approximately 0.2 Hz increments. Each channel of excitation contained 17 frequency components, Table 5.9.

Table 5.9: Optimal multisine excitation definition used for flight testing with Thor.

Roll		Pitch		Yaw	
Frequency	**Phase**	**Frequency**	**Phase**	**Frequency**	**Phase**
[Hz]	**[deg]**	**[Hz]**	**[deg]**	**[Hz]**	**[deg]**
0.10	353.756	0.30	6.708	0.50	355.903
0.69	312.150	0.89	336.847	1.09	338.036
1.29	220.329	1.49	152.080	1.68	200.831
1.88	95.401	2.08	6.216	2.28	354.093
2.48	224.842	2.67	131.959	2.87	112.929
3.07	265.284	3.27	160.448	3.47	140.611
3.66	338.757	3.86	162.577	4.06	177.917
4.26	304.622	4.46	57.808	4.65	112.396
4.85	156.661	5.05	275.891	5.25	324.769
5.45	15.095	5.64	97.250	5.84	143.524
6.04	124.419	6.24	159.478	6.44	204.211
6.63	112.446	6.83	157.886	7.03	186.814
7.23	139.757	7.43	122.907	7.62	184.220
7.82	91.377	8.02	36.834	8.22	76.128
8.42	303.593	8.61	226.413	8.81	292.564
9.01	83.271	9.21	355.592	9.41	90.306
9.60	202.445	9.80	74.086	10.00	130.969

The exact excitation definitions are provided in the configuration data along with the full flight data log [48]. Estimation of the frequency response used three segments aligned with the three repetitions of the excitation and a rectangular, non-overlapping window.

The estimated nominal stability margins for the four flight test segments are compared to the linear model of Section 5.1 in Figure 5.5.
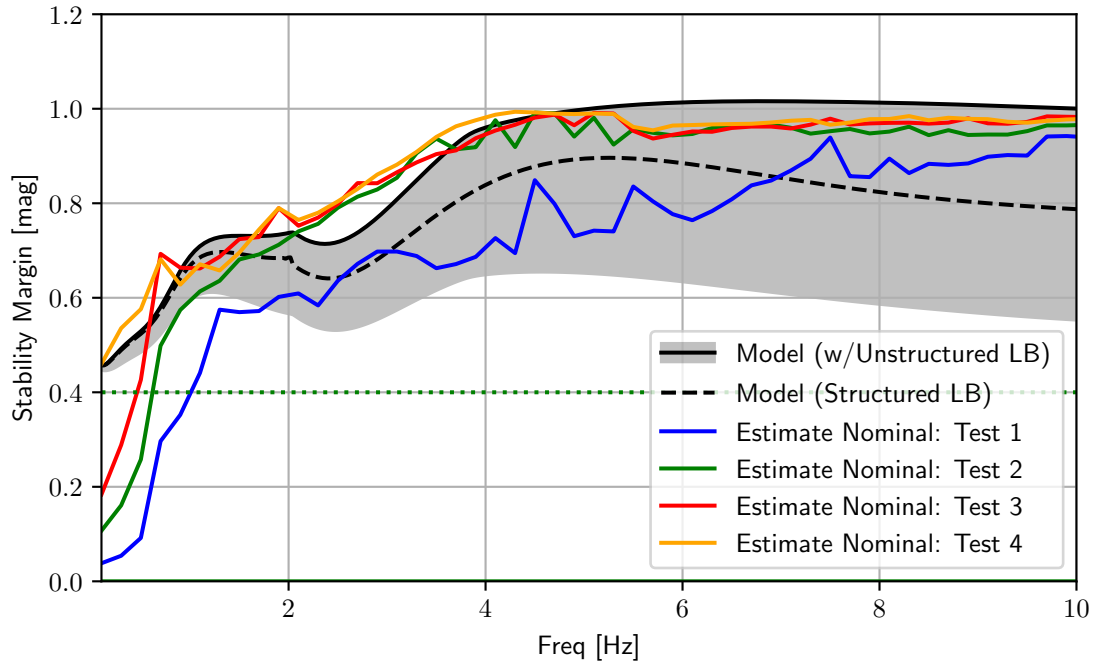
Figure 5.5: MIMO stability margin plot of nominal estimated stability margins with linear model nominal stability margin with unstructured and structured lower bound; κ_{NS} depicted as solid lines and $\kappa_{\mathrm{RS_U}}$ is the lower bound of the shaded regions.

The MIMO NS margins for Test 2, 3, and 4 generally agree with the linear model for frequencies above 1 Hz. The larger excitation amplitude of Test 3 and Test 4 appears to have resulted in slightly higher estimate for κ_{NS} at low frequencies and a slightly smoother estimate at higher frequencies. The margin estimates for Test 1 appear to indicate a significantly lower estimate for κ_{NS} at all frequencies.

The estimated nominal stability margins with structured lower bounds for the four flight test segments are compared in Figure 5.6.
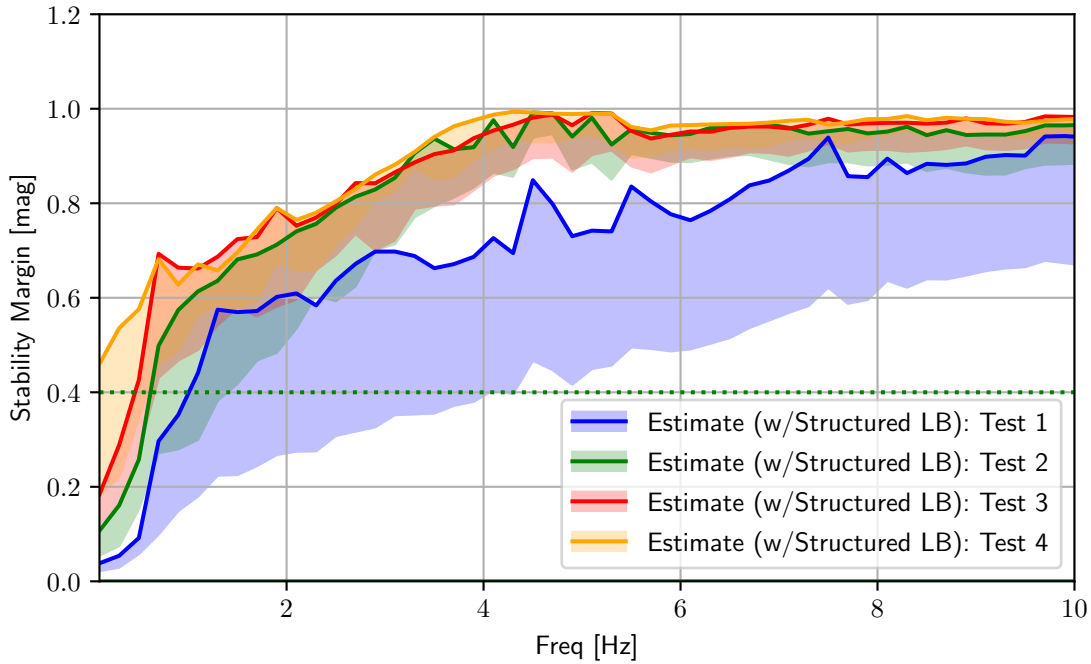
Figure 5.6: MIMO stability margin plot of nominal estimated stability margins with structured lower bounds; κ_{NS} depicted as solid lines and $\kappa_{\mathrm{RS_S}}$ is the lower bound of the shaded regions.

The MIMO NS and structured RS margins for Test 2, 3, and 4 are again in general agreement. The larger amplitude excitation in Test 3 and 4 indicates a slightly reduced uncertainty range than the smaller amplitude excitation used in Test 2. Test 1 clearly indicates a larger uncertainty range than the other three tests, particularly at frequencies above 1 Hz.

The degradation in Test 1 is diagnosed further via inspection of the uncertainty sources within the estimates.

Inspection of the PSD of the spectra of the reference signals r in both the excited and null frequency sets reveals a significant difference in spectral power during Test 1, particularly in the roll channel, Figure 5.7.
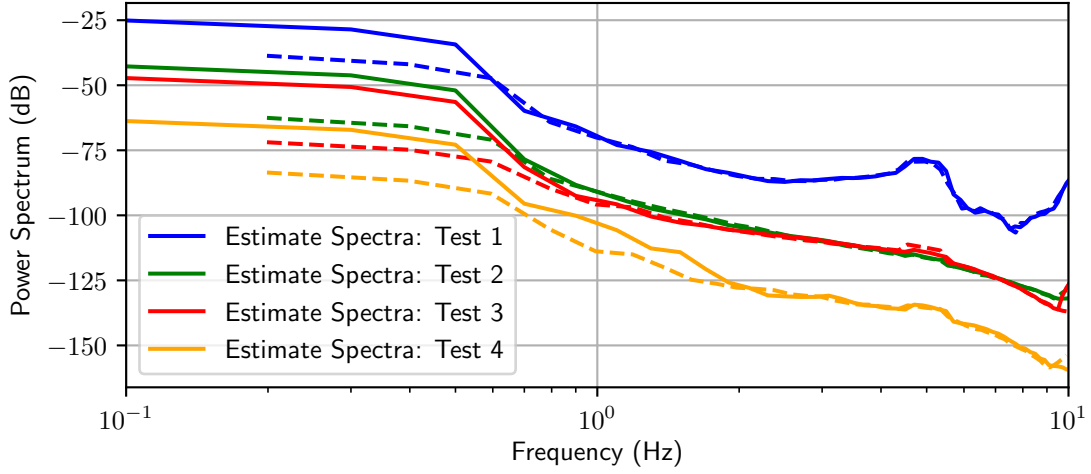
Figure 5.7: Spectrum of the roll channel of r_ϕ in the excited frequencies (solid lines) and the null frequencies (dashed lines).

Note that the spectra in the excited and null frequency sets in Figure 5.7 are nearly the same. A small deviation between the excited and null spectra at frequencies below 0.4 Hz is evident in all 4 tests. This indicates that the reference input, r_ϕ, that originates from the guidance-loop controller, is not correlated with the excitation signal at frequencies above 0.7 Hz.

Inspection of the PSD of the feedback signals, v_{fb}, for the inner-loop roll, pitch, and yaw channels with the excited and null frequency set also reveals a difference in the spectra for Test 1 in the roll channel. The difference is apparent across the majority of frequencies, with the exception of a band of frequencies between 0.7 Hz and 2 Hz. The spectra of the roll channel feedback signal is depicted in Figure 5.8 for all four tests.
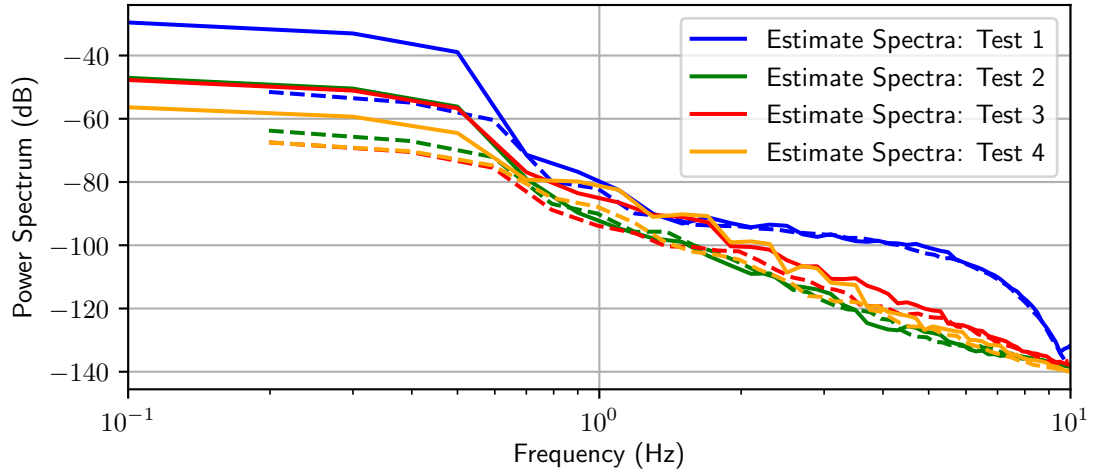
Figure 5.8: Spectrum of the roll channel of v_{fb} in the excited frequencies (solid lines) and the null frequencies (dashed lines).

All four tests show a difference between the spectra of the excited frequencies and the null frequencies below 0.7 Hz; this is similar to the spectra of the reference signals depicted in Figure 5.7.

Together Figure 5.7 and Figure 5.8 point to a roll axis disturbance. This disturbance can be further inspected by evaluating the system outputs, z, particularly in the null frequencies, to isolate the disturbance entering at the plant output. Comparison of spectra of the output signal associated with roll rate, p, with the null frequencies for all four tests are shown in Figure 5.9.
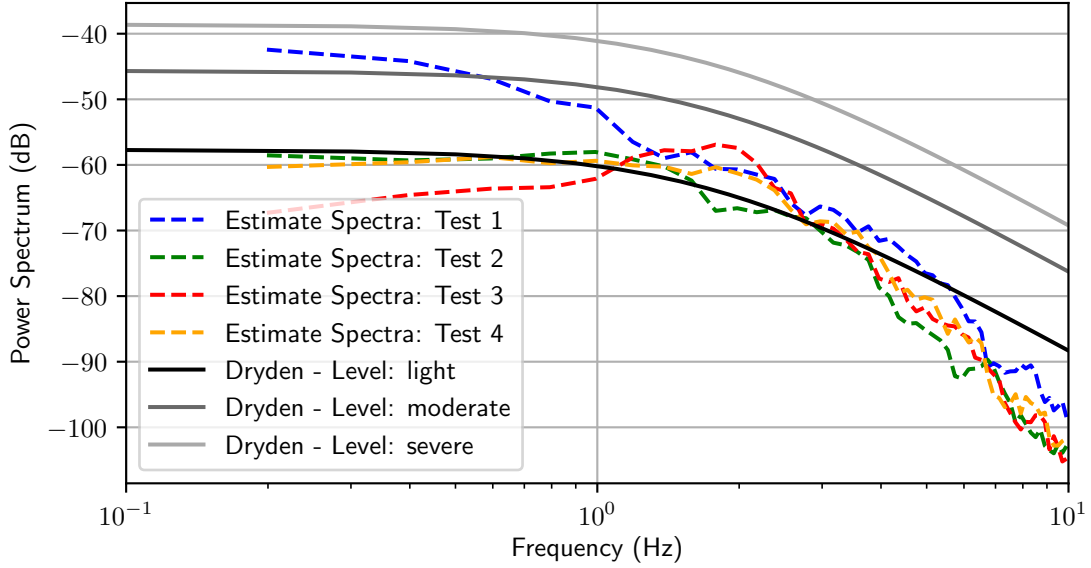
Figure 5.9: Spectrum of the roll channel of z in the null frequency, $\Phi_{zz}[\Omega_N]$ along with Dryden turbulence spectra for light, moderate, and severe levels.

Dryden turbulence model spectra magnitudes (scaled for the aircraft model and flight condition) are included in Figure 5.9 for reference [22]. Figure 5.9 shows that Test 1 was subject to a large low frequency disturbance that exceeded a gust equating to "moderate" turbulence. Figure 5.9 is not intended to indicate that the turbulence levels are measurable from the system outputs in the null frequencies; the output response in the null is subject to feedback in the null frequencies as disturbance rejection for the controller. However, the turbulence scale does provide context for comparing relative magnitudes.

The degraded stability assessment of Test 1 appears to be attributable to a significant gust encounter. Note that the aircraft stability margins themselves are not impacted by the presence of disturbances, rather the estimate of the stability margins are impacted. The impact is apparent in the uncertainty estimate of the MIMO robust stability margins in Figure 5.6. Reduction of the MIMO stability margins is also attributable to the presence of the disturbance; margins are computed as the reciprocal of the maximum singular value of the estimated sensitivity function; for example: $\kappa = \frac{1}{\bar{\sigma}(\hat{S})}$. This results in biased stability margin estimates, here it is always conservative such that an increase

in uncertainty, W_S, results in variation in $\bar{S}$ or $\hat{S}$ that will lead to reduced margin estimates. Note that the FRE are unbiased estimates, only the MIMO stability estimates become biased. Thus, in the example of Test 1 with Thor, the reduced stability margin estimates are appropriate.

Chapter 6

Conclusion and Future Work

This study is focused on the estimation of robust stability margins purely from *in situ* measurements using non-parametric spectral methods and minimal a prori knowledge. The critical novel development here is the estimation of disturbance spectral power via the null frequency set Chapter 2. Estimation of the disturbance spectral power was shown to allow for isolation and quantification of several sources of uncertainty in Chapter 3. Application of stability assessment using the estimated nominal and uncertain components of the FRF were demonstrated by adapting existing MIMO robust stability methods.

The developed methods and results were demonstrated via a MIMO example. Estimation of a plant system and disturbances were shown in Section 2.4. The same example was then used to demonstrate the uncertainty estimation by comparing to estimation error in Section 3.6. Finally, a control system was defined for the example system and a stability assessment was shown in Section 4.5 for the closed-loop system. These examples and the FRE approach used for the analysis, were intentionally specified to highlight disturbances and the resulting uncertainty. Because the emphasis was to highlight uncertainty, well established spectral estimation methods to improve nominal estimation were avoided. The examples used rather short excitations and a non-overlapping rectangular window function; significant estimation improvement can be obtained with a longer excitation and overlapping window function.

Application to real-time has not been explicitly demonstrated. However, the DFT

implementation used throughout has an equivalent recursive implementation which produces identical results [34]. Spectral estimation in real-time is easily achieved on modest hardware [34]. The nominal and unstructured robust stability margin computations rely upon the calculation of the singular values of a small matrix ($C \times C$) for each frequency in the estimate; this is also easily achieved on modest hardware. The structured robust stability analysis is more computationally intensive, though with modest hardware a solution in near real-time (within several seconds of excitation completion) should be achievable.

In addition to adopting more refined and established spectral estimation methods, the techniques here can be further developed. Uncertainty here was specified with an implicit Gaussian distribution, a hypothesis test would be appropriate to both validate the distribution and provide appropriate statistical metrics. Linear interpolation was used to bring the spectral estimates to the common excitation frequency basis; parametric methods could be applied with relative ease. Non-parametric spectral methods were used as the basis for the FRE; however, the spectra were estimated on a sparse frequency basis (number of frequencies $\ll$ number of time samples). In this case, the DFT (Equation (2.14)) can be interpreted as an over-determined system and employ alternative estimation methods. For the problems addressed here, the system input is always the excitation, and in this particular case the DFT is a maximum likelihood estimate [2]. Reframing the DFT as an estimation problem may seem a simple matter of semantics. However, when cast into an estimation framework, it becomes apparent that additional underlying stochastic information is available; in the form of a Fischer information matrix or Cramér-Rao bounds. This is not the case when the DFT is computed on a "full-resolution" frequency basis; and is therefor generally not considered in the context of spectral estimation.

References

[1] Julius S. Bendat and Allan G. Piersol. *Random Data*. Wiley Series in Probability and Statistics. John Wiley & Sons, Inc., Hoboken, NJ, USA, jan 2010.

[2] Rik Pintelon and Johan Schoukens. *System Identification*. John Wiley & Sons, Inc., Hoboken, NJ, USA, 2 edition, mar 2012.

[3] Alan V. Oppenheim and George C. Verghese. *Signals, Systems & Inference*. Pearson, 2015.

[4] K. Deergha Rao. *Signals and systems*. Springer International Publishing, apr 2018.

[5] Lennart Ljung. *System Identification*. John Wiley & Sons, Inc., Hoboken, NJ, USA, dec 1999.

[6] Urban Forssell and Lennart Ljung. Closed-loop identification revisited. *Automatica*, 35(7):1215–1241, jul 1999.

[7] Mark B. Tischler and Robert K. Remple. *Aircraft and Rotorcraft System Identification*. American Institute of Aeronautics and Astronautics, aug 2006.

[8] Mark B. Tischler and Robert K. Remple. Aircraft and Rotorcraft System Identification, Second Edition. *Aircraft and Rotorcraft System Identification, Second Edition*, aug 2012.

[9] Vladislav Klein and Eugene A. Morelli. *Aircraft System Identification: Theory and Practice*. American Institute of Aeronautics and Astronautics, Reston ,VA, jan 2006.

[10] Eugene A. Morelli and Vladislav. Klein. *Aircraft System Identification: Theory and Practice, 2nd ed.* Sunflyte, Williamsburg, VA, 2nd edition, 2016.

[11] Sigurd Skogestad and Ian Postlethwaite. *Multivariable Feedback Control—Analysis and Design.* John Wiley & Sons Ltd, Chichester, England, 2nd edition, 2007.

[12] J. T. Bosworth and J. C. West. Real-Time Open-Loop Frequency Response Analysis of Flight Test Data. *AIAA Paper*, apr 1986.

[13] Joseph Gera and John T Bosworth. Dynamic Stability and Handling Qualities Tests on a Highly Augmented, Statically Unstable Airplane. Technical report, NASA, aug 1987.

[14] Robert Clarke, John J. Burken, John T. Bosworth, and Jeffery E. Bauer. X-29 Flight Control System : Lessons Learned. *Nasa TM 4598*, 1994.

[15] John J. Burken. Flight-Determined Stability Analysis of Multiple-Input-Multiple-Output Control Systems. *NASA TM 4416*, 1992.

[16] John J. Burken. Flight-determined multivariable stability analysis and comparison of a control system. *Journal of Guidance, Control, and Dynamics*, 16(6):1026–1031, nov 1993.

[17] John T. Bosworth and John J. Burken. Tailored excitation for multivariable stability-margin measurement applied to the X-31A nonlinear simulation. *NASA Technical Memorandum*, 3190(113085), aug 1997.

[18] Piero Miotto and James D. Paduano. Application of real structured singular values to flight control law validation. *Journal of Guidance, Control, and Dynamics*, 19(6):1239–1245, nov 1996.

[19] Dwight L. Balough. Determination of X-36 stability margins using real-time frequency response techniques. In *23rd Atmospheric Flight Mechanics Conference*, pages 105–115. American Institute of Aeronautics and Astronautics Inc, AIAA, 1998.

[20] Ethan Baumann. Tailored Excitation for Frequency Response Measurement Applied to the X-43A Flight Vehicle. *NASA TM 214609*, 2007.

[21] Eugene A. Morelli. Multiple input design for real-time parameter estimation in the frequency domain. In *IFAC Proceedings Volumes (IFAC-PapersOnline)*, 2003.

[22] Christopher D. Regan. In-flight stability analysis of the X-48B aircraft. In *AIAA Atmospheric Flight Mechanics Conference and Exhibit*, 2008.

[23] Rick Lind and Marty Brenner. Robust aeroservoelastic stability analysis : flight test applications. *Automatica*, 37(5):797–799, 1999.

[24] Martin J. Brenner. Aeroservoelastic Uncertainty Model Identification from Flight Data. Technical Report July, NASA Dryden Flight Research Center, 2001.

[25] Rick Lind. Flight testing with the flutterometer. *Journal of Aircraft*, 40(3):574–579, 2003.

[26] Matthew Lichter, Alec Bateman, and Gary Balas. Flight Test Evaluation of a Run-Time Stability Margin Estimation Tool. In *AIAA Guidance, Navigation, and Control Conference*, Reston, Virigina, aug 2009. American Institute of Aeronautics and Astronautics.

[27] Jared Grauer and Eugene Morelli. Method for Real-Time Frequency Response and Uncertainty Estimation. *Journal of Guidance, Control, and Dynamics*, 37(1):336–344, jan 2014.

[28] Jared A Grauer and Matthew J Boucher. Frequency-domain deconvolution for flight dynamics applications. In *2018 Atmospheric Flight Mechanics Conference*, jun 2018.

[29] Jared Grauer and Matthew Boucher. Identification of Aeroelastic Models for the X-56A Longitudinal Dynamics Using Multisine Inputs and Output Error in the Frequency Domain. *Aerospace*, 6(2):24, feb 2019.

[30] Jared A Grauer. Aerodynamic Parameter Estimation Using Reconstructed Turbulence Measurements. In *AIAA Scitech 2020 Forum*, Reston, Virginia, jan 2020. American Institute of Aeronautics and Astronautics.

[31] Jared A. Grauer and Matthew Boucher. Aircraft System Identification from Multisine Inputs and Frequency Responses. In *AIAA Scitech 2020 Forum*, Reston, Virginia, jan 2020. American Institute of Aeronautics and Astronautics.

[32] Eugene A. Morelli and Kevin Cunningham. Aircraft Dynamic Modeling in Turbulence, aug 2012.

[33] M. R. Schroeder. Synthesis of Low-Peak-Factor Signals and Binary Sequences with Low Autocorrelation. *IEEE Transactions on Information Theory*, 16(1):85–89, 1970.

[34] Eugene A Morelli and Jared A Grauer. Practical aspects of frequency-domain approaches for aircraft system identification. *Journal of Aircraft*, 57(2):268–291, 2020.

[35] Fredric J. Harris. On the Use of Windows for Harmonic Analysis with the Discrete Fourier Transform. *Proceedings of the IEEE*, 66(1):51–83, 1978.

[36] Alan V. Oppenheim, Alan S. Willsky, and Syed H. Nawab. *Signals and Systems*. Prentice Hall, Upper Saddle River, N.J., 2 edition, 1997.

[37] Giovanni Betta, Consolatina Liguori, and Antonio Pietrosanto. Propagation of uncertainty in a discrete Fourier transform algorithm. *Measurement: Journal of the International Measurement Confederation*, 27(4):231–239, jun 2000.

[38] J. M. Forniés-Marquina, J. Letosa, M. García-Gracia, and J. M. Artacho. Error propagation for the transformation of time domain into frequency domain. *IEEE Transactions on Magnetics*, 33(2 PART 2):1456–1459, 1997.

[39] Matthew S. Holzel and Eugene A. Morelli. Real-time frequency response estimation from flight data. *Journal of Guidance, Control, and Dynamics*, 35(5):1406–1417, sep 2012.

[40] Dunstan Graham and Duane McRuer. *Analysis of Nonlinear Control Systems*. John Wiley & Sons, 1961.

[41] Arthur Gelb and Wallace E. Vander Velde. *Multiple-input describing functions and nonlinear system design*. McGraw-Hill, New York, 1968.

[42] Christopher D. Regan. mAEWing2: Conceptual design and system test. *AIAA Atmospheric Flight Mechanics Conference, 2017*, 2017.

[43] Holger Duda. Effects of Rate Limiting in Flight Control Systems - A New PIO Criterion. *1995 Guidance, Navigation, and Control Conference*, 1995.

[44] David H. Klyde, Duane T. McRuer, and Thomas T. Myers. Pilot-induced oscillation analysis and prediction with actuator rate limiting. *Journal of Guidance, Control, and Dynamics*, 20(1):81–89, may 1997.

[45] Pauli Virtanen, Ralf Gommers, Travis E. Oliphant, Matt Haberland, Tyler Reddy, David Cournapeau, and Others. SciPy 1.0: fundamental algorithms for scientific computing in Python. *Nature Methods*, 17(3):261–272, 2020, 1907.10121.

[46] Andrei Dorobantu, Will Johnson, F. Adhika Lie, Brian Taylor, Austin Murch, Yew Chai Paw, Demoz Gebre-Egziabher, and Gary Balas. An airborne experimental test platform: From theory to flight. *Proceedings of the American Control Conference*, pages 659–673, 2013.

[47] Christopher D. Regan, Aditya Kotikalpudi, David K. Schmidt, and Peter Seiler. Maewing2: Initial flight test and system identification of a flexible uav. In *AIAA Scitech 2020 Forum*, volume 1 PartF, Reston, Virginia, 2020. American Institute of Aeronautics and Astronautics.

[48] Christopher D. Regan. Thor Flight #128 - Retrieved from the University of Minnesota Digital Conservancy. https://hdl.handle.net/:106755, 2021.

[49] Lawrence R. Rabiner, Ronald W. Schafer, and Charles M. Rader. The Chirp z-Transform Algorithm and Its Application. *Bell System Technical Journal*, 48(5):1249–1292, 1969.

Appendix A

Time-Frequency Transforms

Numerous transforms relate to the time-frequency duality of signals; and several variations of those definitions can be found in literature [3, 36, 4, 1, 2]. An incomplete, but sufficient, set of self-consistent transforms are defined for use in the main text. The Laplace Transform (LT) is presented first, transforming complex-valued time-domain signals to their frequency-domain companions. The Fourier Transform (FT) is presented as equivalent to the Laplace Transform for purely harmonic signals. The Discrete Fourier Transform (DFT) is presented as a finite-length discretization (time-domain and frequency-domain) approximation of the Fourier Transform. The Z-Transform and Chirp Z-Transform (CZT) are similarly defined for the discretization of the Laplace Transform and evaluation along a particular path.

Throughout the description of the transforms, the signal in the time-domain is presented either as a continuous function of time, $x(t)$, or as a time-series, $x[t_n]$. The signals in the frequency-domain are denoted X, with a unique subscript for each transform. Frequency-domain signals are denoted as either a function, $X(\ )$, or a series, $X[\ ]$, of frequency (f as cycles per second or ω as radians per second) in either s-plane coordinates (s) or z-plane coordinates (z).

The time-series data used in the finite and discretized transforms are used to estimate the infinite and continuous transforms, such that: $X(s) \mathrel{\hat{=}} X[\ ]$. The desire is to specify both systems and the characteristics of those systems (control and plant models, sensitivity functions, loop functions, stability margins, etc.) in s coordinates.

Parseval's Theorem is provided in Appendix A.4.

A.1 Laplace Transform

The Laplace transform, $\mathcal{L}$ relates a time-domain function, $x(t) \in \mathbb{R}$, to its frequency-domain function, $X_{\mathcal{L}}(s) \in \mathbb{C}$, with coordinates in $s \in \mathbb{C}$. The coordinates consist of an amplitude, $\sigma \in \mathbb{R}$, and frequency, $\omega \in \mathbb{R}$, such that: $s := \sigma + j\omega$.

$$X_{\mathcal{L}}(s) := \mathcal{L}(x(t)) = \int_{-\infty}^{\infty} x(t) \ e^{-st} \ dt \tag{A.1}$$

A.2 Fourier Transform

A function in time, $x(t)$, is related to its function in frequency, $X_{\mathcal{F}}(\omega)$, by the Fourier Transform, $\mathcal{F}$. The definition here uses the angular frequency, ω (with units of radians per second), rather than the cyclic frequency f (with units of cycles per second), where: $\omega = 2\pi f$. The Fourier transform is defined, Equation (A.2).

$$X_{\mathcal{F}}(j\omega) := \mathcal{F}(x(t)) = \int_{-\infty}^{\infty} x(t) \ e^{-j\omega t} \ dt \tag{A.2}$$

The Fourier transform, $\mathcal{F}$, is equivalent to the Laplace transform, $\mathcal{L}$, for s taken along the $j\omega$ coordinate (i.e., $\sigma = 0$), Equation (A.3).

$$X_{\mathcal{F}}(j\omega) \equiv X_{\mathcal{L}}(s) \qquad \forall s \in \{s = j\omega\} \tag{A.3}$$

An intermediate definition for a finite FT, operating over a finite length time-series (for $t = 0$ to $t = T$), is useful as real-world signals have finite duration. The Finite Fourier Transform approximates the Fourier Transform if the time-series is periodic within the time duration, Equation (A.4).

$$X_{\mathcal{F}+}(j\omega, T) \approx \int_0^T x(t) \ e^{-j\omega t} \ dt \tag{A.4}$$

The Discrete Fourier Transform (DFT) has several variations in definition, though the disctictions are mostly is a matter of semantics. The DFT is defined by first discretizing the finite FT. The key aspects of the discretized FT are that it operates on a discrete, periodic, and finite length discrete time-series, $x[t_n]$, which is sampled at a fixed rate, f_s, and corresponding uniform time increments of Δt. The time-series is

transformed to a frequency-domain series, $X_{\mathcal{D}} \in \mathbb{C}$. The finite FT is discretized for a set of frequencies, ω_m, in Equation (A.5).

$$X_{\mathcal{D}}[\omega_m, T] := \mathcal{D}(x[t_n]) = \Delta t \sum_{n=0}^{N-1} x[t_n]\, e^{-j(\omega_m \Delta t)n} \tag{A.5}$$

The usual selection of frequencies in Equation (A.5) spans the range from zero to the sampling frequency, Equation (A.6).

$$\omega_m = 2\pi \frac{m}{N \Delta t} \qquad m = 0, 1, 2, ..., N - 1 \tag{A.6}$$

For transformation of strictly real-time signals, $x[t_n] \in \mathbb{R}$, the discretized FT components, $X_{\mathcal{D}}[\omega_m, T]$, are symmetric about the Nyquist frequency, $f_{Nyquist} = \frac{f_s}{2}$; only the transform out to $N/2$ are unique.

The DFT itself can then be defined simply in terms of the discretized FT, which simply normalizes $X_{\mathcal{D}}$ by the time increment, Δt, Equation (A.7).

$$X_{\mathcal{DFT}}[\omega_m] := \frac{X_{\mathcal{D}}[\omega_m, T]}{\Delta t} \tag{A.7}$$

The preceding definition for the DFT has been largely influenced by the requirements of the fast Fourier transform (FFT) algorithm. The DFT also has inconsistent definition; in some texts the DFT is strictly defined as $X_{\mathcal{DFT}}$ with frequencies as in Equation (A.6), and in others $X_{\mathcal{D}}$ is defined as the DFT.

For the purpose here, the FT requires an arbitrary set of frequencies, ω_m in Equation (A.5) and here the purpose of Fourier transforms are to estimate the power spectral density (PSD). Evaluation on an arbitrary set of frequencies is particularly useful when evaluating multisine excitations, in which case ω_m can be defined as either the excitation frequency set or the null frequency set. For M frequencies in the DFT and $M << N$ the DFT can also be efficiently computed recursively or partially pre-computed as a matrix (in which the matrix elements are $e^{-j(\omega_m \Delta t)n}$ for each ω_m and n) [34]. The scaling required to produce the PSD will be further addressed in the context of Parseval's theorem, Appendix A.4.

The discretized FT, $\mathcal{D}$, approximates the continuous FT, $\mathcal{F}$, with several conditions. First, the DFT operates on a finite length time series, for the approximation to be valid

the time-function of the FT must be periodic within the sampled length. Second, the sampling rate must be sufficiently fast to resolve the fastest frequencies in the time-function. This is usually specified in terms of the Nyquist frequency such that the fastest frequency in the time-function, $f_{max} << f_{Nyquist}$. Often low-pass filters are applied, both via a circuit's analog stage and digitally, to ensure the time-function, or time-series, is attenuated to prevent aliasing. Third, the sampling increment, Δt, must be applied to properly scale the DFT.

The transformation from the Laplace Transform to the discretized FT is summarized along with the required approximations.

Figure A.1: Block Diagram showing the progressive approximation from Laplace Transform to Discrete Fourier Transform.

Laplace

$$X_{\mathcal{L}}(s) = \int_{-\infty}^{\infty} x(t) \; e^{-st} \; dt$$

$$s = \sigma + j\omega$$

$$s \in \{s = j\omega\}$$

Fourier

$$X_{\mathcal{F}}(j\omega) = \int_{-\infty}^{\infty} x(t) \; e^{-j\omega t} \; dt$$

$$x[t_n] \text{ samples } x(t)$$

DFT

$$X_{\mathcal{DFT}}[\omega_m] = \sum_{n=0}^{N-1} x[t_n] \; e^{-j(\omega_m \Delta t)n}$$

$$m \in \{1, 2, \dots, M\}$$
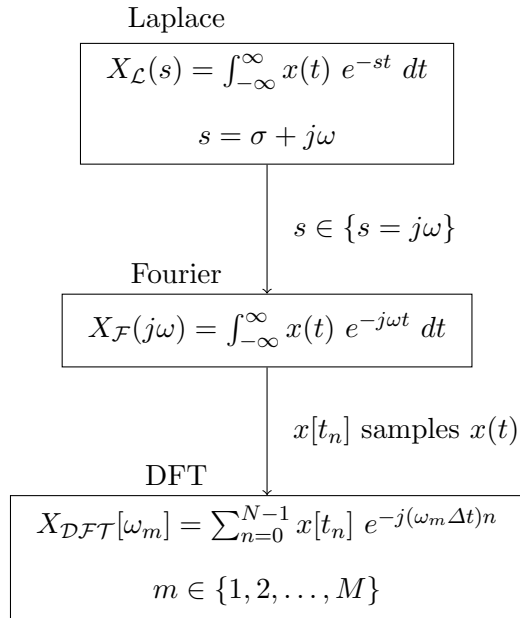
From the preceeding it is apparent that $X_{\mathcal{L}}(s) \approx X_{\mathcal{F}}(j\omega) \approx \Delta t X_{\mathcal{DFT}}[\omega_m]$ for $x[t_n] \approx x(t)$, $s = j\omega$, and ω_m sufficiently capturing all frequencies. These conditions are also sufficient for the DFT, $X_{\mathcal{DFT}}$, to estimate the Laplace transform, $X_{\mathcal{L}}$.

$$X_{\mathcal{DFT}}[\omega_m] \hat{=} \frac{1}{\Delta t} \; X_{\mathcal{F}}(j\omega) \hat{=} \frac{1}{\Delta t} \; X_{\mathcal{L}}(s) \tag{A.8}$$

A.3 Z-Transform

The Z-Transform, $\mathcal{Z}$, is a discretization of the Laplace transform. The time-series, $x[t_n]$, is sampled at a fixed rate, f_s, and uniform time increments of Δt, such that $t_n = n\ \Delta t$. The z coordinates are defined, $z = Ae^{j\phi}$, with magnitude, $A \in \mathbb{R}$, and phase $\phi \in \mathbb{R}$.

The bilateral Z-Transform is defined as Equation (A.9).

$$X_{\mathcal{Z}}[z] := \mathcal{Z}(x[t_n]) = \sum_{n=-\infty}^{\infty} x[t_n]\ z^{-n} \tag{A.9}$$

Coordinates in s relate to coordinates in z, as: $z = e^{s\Delta t}$. The bilateral Z-transform, $\mathcal{Z}$, approximates the Laplace transform, $\mathcal{L}$, with a normalized time increment, Δt; $X_{\mathcal{L}}[s] \approx \Delta t\ X_{\mathcal{Z}}[z]$.

The unilateral Z-Transform, $\mathcal{Z}^+$, is defined as Equation (A.10), where $x(s)$ is sampled only for strictly positive times, $t \geq 0$.

$$X_{\mathcal{Z}^+}[z] := \mathcal{Z}^+(x[t_n]) = \sum_{n=0}^{\infty} x[t_n]\ z^{-n} \tag{A.10}$$

The "Chirp Z-Transform" (CZT) is a specification of a finite unilateral Z-Transform defined along a spiral path in z coordinates, Equation (A.11).

$$X_{\mathcal{CZT}}[z_m] \approx \sum_{n=0}^{N-1} x[t_n]\ z_m^{-n} \tag{A.11}$$

Where: $z_m = A\ W^{-m}$ $\qquad m = 0, 1, 2, ..., M - 1$

The "Chirp" coordinates follow a contour in z defined by an initial position, $A \in \mathbb{C}$, and an increment, $W \in \mathbb{C}$. The CZT can be solved efficiently with the "Bluestein" algorithm described in [49]. The CZT is strictly a "one-sided" transform; it computes the transform with only the z coordinates specified in a unilateral Z-Transform.

The CZT approximates the Z-transform, $\mathcal{Z}$, as long as z_m sufficiently approximates the full z-space. For a single frequency sine wave signal; z_m can sufficiently approximate the full z-space with a single coordinate coinciding with the sine wave frequency.

The transformation from the Laplace Transform to the CZT is summarized along with the required approximations.

Figure A.2: Block Diagram showing the progressive approximation from Laplace Transform to Chirp Z-Transform.

Laplace

$$X_{\mathcal{L}}(s) = \int_{-\infty}^{\infty} x(t)\ e^{-st}\ dt$$

$$s = \sigma + j\omega$$

$x[t_n]$ samples $x(t)$
$z \in \{z = e^{s\ dt}\}$

Z-Transform

$$X_{\mathcal{Z}+}[z] = \sum_{n=0}^{N-1} x[t_n]\ z^{-n}$$

$z_m \in \{z = A\ W^{-m}\}$

CZT

$$X_{\mathcal{CZT}}[z_m] = \sum_{n=0}^{N-1} x[t_n]\ z_m^{-n}$$

$$A \in \mathbb{C}, W \in \mathbb{C}$$

$$m \in \{0, 1, \ldots, M-1\}$$
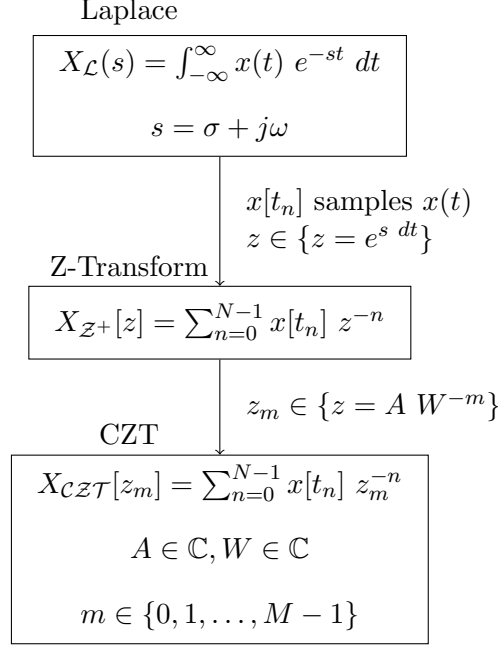
From the preceeding it is apparent that $X_{\mathcal{L}}(s) \approx \Delta t\ X_{\mathcal{Z}}[z] \approx \Delta t\ X_{\mathcal{CZT}}[z_m]$ with the limitations that $x[t_n]$ adequately samples $x(t)$, s is discretized to z, and the path z_m adequately approximates the full domain of z. The estimation is then the reverse with the same criteria, yielding Equation (A.12).

$$X_{\mathcal{CZT}}[z_m] \hat{=} X_{\mathcal{Z}}[z] \hat{=} \frac{1}{\Delta t}\ X_{\mathcal{L}}[s] \tag{A.12}$$

Note that both the DFT and CZT are defined along specified paths in s coordinates (the FT is along $s = j\omega$ and the CZT is along "Chirp" coordinates that describes a spiral in the z Coordinates). For a linear and time-invariant system in harmonic steady-state; the CZT and discretized FT are equivalent.

A.4   Parseval's Theorem

Parseval's theorem specifies that the signal power in the time-domain and frequency-domain are the same. The theorem can be defined in both the continuous domain with

the Fourier transform and in a discrete, finite domain. In either domain Parseval's Theorem provides relations so that the total signal power is preserved.

Theorem A.1 Parseval's Theorem in Continuous, Infinite Domain

If $x(t)$ is a real-valued signal with Fourier transform (FT), $X_{\mathcal{F}}(j\omega)$, then the Total Power of $x(t)$, is given by

$$Total\ Power = \int_{-\infty}^{\infty} |x(t)|^2 dt = \frac{1}{2\pi} \int_{-\infty}^{\infty} |X_{\mathcal{F}}(j\omega)|^2 d\omega \tag{A.13}$$

Theorem A.2 Parseval's Theorem in Discrete, Finite Domain

If $x[t_n]$ is a real-valued discrete time-series with length N and discrete Fourier transform (DFT), $X_{\mathcal{DFT}}[\omega]$, where all the power in the time-series is contained within the frequencies of the DFT, ω; then the Total Power of $x[t_n]$, is given by

$$Total\ Power = \frac{1}{N} \sum_{n=0}^{N-1} |x[t_n]|^2 = \frac{1}{N^2} \sum_{m=1}^{M} |X_{\mathcal{DFT}}[\omega]|^2 \tag{A.14}$$

In the particular case of DFT frequencies selected in the band: $0 < \omega < \omega_{Nyquist}$ contain all the power; the right side of Equation (A.14) can be replaced with Equation (A.15).

$$\frac{2}{N^2} \sum_{m=1}^{M} |X_{\mathcal{DFT}}[\omega_m]|^2 \tag{A.15}$$

A.5 Power Spectrum

Parseval's Theorem is the basis for defining the PSD such that there is equivalence in both the time-domain and frequency-domain. Here only the discrete, finite duration PSD is addressed. For M evaluated frequencies selected strictly in the band: $0 < \omega < \omega_{Nyquist}$, which contain all the power within the time-series, the desired form for the PSD is then: Total Power $= \sum \Phi[\omega_m]$. This results in the PSD for the auto-spectra, Φ_{xx}, and cross-spectra, $\Phi_{x \to y}$, defined in Equation (A.16) and Equation (A.17).

$$\Phi_{xx}[\omega_m] = \frac{2}{N^2} |X_{\mathcal{DFT}}[\omega_m]|^2 \tag{A.16}$$

$$\Phi_{x \to y}[\omega_m] = \frac{2}{N^2} X^*_{\mathcal{DFT}}[\omega_m] \; Y_{\mathcal{DFT}}[\omega_m] \tag{A.17}$$

Furthermore, the DFT can be replaced with the CZT, Equation (A.18) and Equation (A.19), and noting that z_m has corresponding frequencies at ω_m.

$$\Phi_{xx}[\omega_m] = \frac{2}{N^2} |X_{\mathcal{CZT}}[z_m]|^2 \tag{A.18}$$

$$\Phi_{x \to y}[\omega_m] = \frac{2}{N^2} X^*_{\mathcal{CZT}}[z_m] \; Y_{\mathcal{CZT}}[z_m] \tag{A.19}$$

Parseval's Theorem is then restated in terms of the PSD.

Theorem A.3 Parseval's Theorem with PSD

If $x[t_n]$ is a real-valued discrete time-series with length N and power spectral density, $\Phi_{xx}[\omega_m]$, where all the power in the time-series is contained within the frequencies of the PSD, ω_m; then the Total Power of $x[t_n]$, is given by

$$Total \; Power = \frac{1}{N} \sum_{n=0}^{N-1} |x[t_n]|^2 = \sum_{m=1}^{M} \Phi_{xx}[\omega_m] \tag{A.20}$$

Appendix B

Stability Definitions and Theorems

Definition B.1 Stability

[11, Definition 4.4]

A system is (internally) stable if none of its components contain hidden unstable modes and the injection of bounded external signals at any place in the system results in bounded output signals measured anywhere in the system.

Theorem B.2 BIBO Stability

[11, 4]

A system is said to be bounded-input bounded-output (BIBO) stable if and only if every bounded-input sequence produces a bounded-output sequence. The input $x[n]$ is bounded if there exists a fixed positive finite value β_x such that:

$$|x[n]| \leq \beta_x < \infty, \quad \forall n$$

Similarly, the output $y[n]$ is bounded if there exists a fixed positive value β_y such that:

$$|y[n]| \leq \beta_y < \infty, \quad \forall n$$

Theorem B.3 Nyquist Stability Theorem

[11, Theorem 4.7]

Let P_{ol} denote the number of open-loop unstable poles in $L(s)$. The close-loop system with loop transfer function $L(s)$ and negative feedback is stable if and only if the Nyquist plot of $\det(I + L(s))$

    i makes P_{ol} anti-clockwise encirclements of the origin, and

    ii does not pass through the origin.

Theorem B.4 Small Gain Theorem

[11, Theorem 4.10]

Consider a system with a stable loop transfer function $L(s)$. Then the closed-loop system is stable if

$$||L(j\omega)|| < 1, \quad \forall \omega$$

Where $||L||$ denotes any matrix norm satisfying $||AB|| \leq ||A|| \, ||B||$.

Definition B.5 SVD of a Matrix Inverse

[11, Equation A.39]

Let A be a non-singular matrix with $A \in \mathbb{C}^{C \times C}$, then

$$\bar{\sigma}(A^{-1}) = \frac{1}{\underline{\sigma}(A)}$$

Definition B.6 Fan's Theorem

[11, Equation A.48]

Let A and B be complex-valued non-singular matrices with dimension $C \times C$, then

$$\sigma_c(A) - \underline{\sigma}(B) \leq \sigma_c(A + B) \leq \sigma_c(A) + \bar{\sigma}(B)$$
$$c \in \{1, 2, \ldots, C\}$$

Appendix C

UltraStick 25e Aircraft Plant Model Definitions

The linear state-space model for the UltraStick 25e aircraft used in Section 5.1 is provided using conventional state-space notation, Equation (C.1).

$$\dot{x} = Ax + Bu$$
$$y = Cx + Du$$

$$(C.1)$$

The model has been linearized from a nonlinear aircraft simulation in steady-level flight at an airspeed of 17 meters per second. Model inputs, u, are described in Table C.1, model outputs y are described in Table C.2, and the states, x, are described in Table C.3. The state-space matrices, A, B, C, and D are provided in Equation (C.2), Equation (C.3), Equation (C.4), and Equation (C.5).

Table C.1:   Inputs

Name	Description
δ_m	Normalized motor speed command, non-dimensional
δ_e	Elevator Deflection, positive down, rad
δ_r	Rudder Deflection, positive left, rad
δ_{aL}	Left Aileron Deflection, positive down, rad
δ_{aR}	Right Aileron Deflection, positive down, rad
δ_{fL}	Left Flap Deflection, positive down, rad
δ_{fR}	Left Flap Deflection, positive down, rad

Table C.2:   Outputs

Name	Description
ϕ	Bank angle, rad
θ	Attitude angle, rad
ψ	Heading angle, rad
p	Roll rate, rad/sec
q	Pitch rate, rad/sec
r	Yaw rate, rad/sec
a_x	Forward acceleration, m/sec^2
a_y	Right acceleration, m/sec^2
a_z	Down acceleration, m/sec^2
V	Total Velocity, m/sec
α	Angle of attack, rad
β	Angle of sideslip, rad
h	Altitude, m
γ	Flight path angle, rad

Table C.3:   States

Name	Description
ϕ	Bank angle, rad
θ	Attitude angle, rad
ψ	Heading angle, rad
p	Roll rate, rad/sec
q	Pitch rate, rad/sec
r	Yaw rate, rad/sec
u	Forward velocity, m/sec
v	Right velocity, m/sec
w	Down velocity, m/sec
N	North position, m
E	East position, m
D	Down position, m
$\dot{\omega}_m$	Normalized motor acceleration, non-dimensional

$$A = \begin{bmatrix}
0.00 & 0.00 & 0.00 & 1.00 & 0.00 & 0.055111 & 0.00 & 0.00 & 0.00 & 0.00 & 0.00 & 0.00 & 0.00 \\
0.00 & 0.00 & 0.00 & 0.00 & 1.00 & 0.001717 & 0.00 & 0.00 & 0.00 & 0.00 & 0.00 & 0.00 & 0.00 \\
0.00 & 0.00 & 0.00 & 0.00 & -0.001719 & 1.001516 & 0.00 & 0.00 & 0.00 & 0.00 & 0.00 & 0.00 & 0.00 \\
0.00 & 0.00 & 0.00 & -16.093282 & -0.139332 & 3.367333 & 0.064160 & -2.823361 & 0.003413 & 0.00 & 0.00 & 0.00 & -0.012838 \\
0.00 & 0.00 & 0.00 & 0.00 & -15.807373 & 1.243550 & 1.048367 & 0.00 & -7.404696 & 0.00 & 0.00 & 0.00 & -0.013146 \\
0.00 & 0.00 & 0.00 & 0.514002 & -0.711687 & -2.775022 & 0.005846 & 1.701517 & 0.00 & 0.00 & 0.00 & 0.00 & -0.001170 \\
0.00 & -9.790694 & 0.00 & 0.00 & -0.891229 & 0.00 & -0.594529 & 0.00 & 0.808056 & 0.00 & 0.00 & 0.00 & 0.012599 \\
9.790680 & 0.00 & 0.00 & 0.896756 & 0.00 & -16.818943 & 0.001974 & -0.872591 & 0.00 & 0.00 & 0.00 & 0.00 & 0.00 \\
0.016809 & -0.539576 & 0.00 & 15.718590 & 0.00 & -0.736914 & 0.00 & -7.559804 & 0.00 & 0.00 & 0.00 & 0.00 & 0.00 \\
0.395312 & 0.00 & -7.183054 & 0.00 & 0.00 & 0.00 & -0.904935 & -0.422532 & -0.050597 & 0.00 & 0.00 & 0.00 & 0.00 \\
0.847959 & 0.00 & -15.407911 & 0.00 & 0.00 & 0.00 & 0.421978 & -0.906346 & 0.021700 & 0.00 & 0.00 & 0.00 & 0.00 \\
0.001604 & -17.00 & 0.00 & 0.00 & 0.00 & 0.00 & -0.055028 & -0.001714 & 0.998483 & 0.00 & 0.00 & 0.00 & 0.00 \\
0.00 & 0.00 & 0.00 & 0.00 & 0.00 & 0.00 & 135.454006 & 0.00 & 7.465902 & 0.00 & 0.00 & -0.082542 & -5.902896
\end{bmatrix} \tag{C.2}$$

$$B = \begin{bmatrix}
0.00 & 0.00 & 0.00 & 0.00 & 0.00 & 0.00 & 0.00 \\
0.00 & 0.00 & 0.00 & 0.00 & 0.00 & 0.00 & 0.00 \\
0.00 & 0.00 & 0.00 & 0.00 & 0.00 & 0.00 & 0.00 \\
9.260479 & 0.00 & -5.008374 & 78.234939 & -78.234939 & 33.013190 & -33.013190 \\
0.00 & -133.690541 & -0.004718 & 3.000712 & 2.996010 & 2.623788 & 2.623788 \\
0.843834 & 0.00 & -82.041062 & -5.752142 & 5.752142 & -1.794120 & 1.794120 \\
0.00 & 0.469794 & -0.838533 & 0.650334 & -0.185432 & 0.362058 & 0.362058 \\
0.00 & 0.00 & 5.302141 & 0.00 & 0.00 & 0.00 & 0.00 \\
0.00 & -2.702760 & -0.046218 & -6.558172 & -6.604237 & -10.250666 & -10.250666 \\
0.00 & 0.00 & 0.00 & 0.00 & 0.00 & 0.00 & 0.00 \\
0.00 & 0.00 & 0.00 & 0.00 & 0.00 & 0.00 & 0.00 \\
0.00 & 0.00 & 0.00 & 0.00 & 0.00 & 0.00 & 0.00 \\
2503.283764 & 0.00 & 0.00 & 0.00 & 0.00 & 0.00 & 0.00
\end{bmatrix} \tag{C.3}$$

$$C = \begin{bmatrix}
1.00 & 0.00 & 0.00 & 0.00 & 0.00 & 0.00 & 0.00 & 0.00 & 0.00 & 0.00 & 0.00 & 0.00 & 0.00 \\
0.00 & 1.00 & 0.00 & 0.00 & 0.00 & 0.00 & 0.00 & 0.00 & 0.00 & 0.00 & 0.00 & 0.00 & 0.00 \\
0.00 & 0.00 & 1.00 & 0.00 & 0.00 & 0.00 & 0.00 & 0.00 & 0.00 & 0.00 & 0.00 & 0.00 & 0.00 \\
0.00 & 0.00 & 0.00 & 1.00 & 0.00 & 0.00 & 0.00 & 0.00 & 0.00 & 0.00 & 0.00 & 0.00 & 0.00 \\
0.00 & 0.00 & 0.00 & 0.00 & 1.00 & 0.00 & 0.00 & 0.00 & 0.00 & 0.00 & 0.00 & 0.00 & 0.00 \\
0.00 & 0.00 & 0.00 & 0.00 & 0.00 & 1.00 & 0.00 & 0.00 & 0.00 & 0.00 & 0.00 & 0.00 & 0.00 \\
0.00 & 0.00 & 0.00 & 0.00 & 0.044350 & 0.00 & -0.594529 & 0.00 & 0.808056 & 0.00 & 0.00 & 0.00 & 0.012599 \\
0.00 & 0.00 & 0.00 & -0.038823 & 0.00 & 0.155293 & 0.001974 & -0.872591 & 0.00 & 0.00 & 0.00 & 0.00 & 0.00 \\
0.00 & 0.00 & 0.00 & 0.00 & -1.255646 & 0.00 & -0.736914 & 0.00 & -7.559804 & 0.00 & 0.00 & 0.00 & 0.00 \\
0.00 & 0.00 & 0.00 & 0.00 & 0.00 & 0.00 & 0.998484 & 0.00 & 0.055034 & 0.00 & 0.00 & 0.00 & 0.00 \\
0.00 & 0.00 & 0.00 & 0.00 & 0.00 & 0.00 & 0.00 & 0.058824 & 0.00 & 0.00 & 0.00 & 0.00 & 0.00 \\
0.00 & 0.00 & 0.00 & 0.00 & 0.00 & 0.00 & -0.003237 & 0.00 & 0.058734 & 0.00 & 0.00 & 0.00 & 0.00 \\
0.00 & 0.00 & 0.00 & 0.00 & 0.00 & 0.00 & 0.00 & 0.00 & 0.00 & 0.00 & 0.00 & -1.00 & 0.00 \\
0.00 & 1.00 & 0.00 & 0.00 & 0.00 & 0.00 & 0.003237 & 0.00 & -0.058734 & 0.00 & 0.00 & 0.00 & 0.00
\end{bmatrix} \quad (C.4)$$

$$D = \begin{bmatrix}
0.00 & 0.00 & 0.00 & 0.00 & 0.00 & 0.00 & 0.00 \\
0.00 & 0.00 & 0.00 & 0.00 & 0.00 & 0.00 & 0.00 \\
0.00 & 0.00 & 0.00 & 0.00 & 0.00 & 0.00 & 0.00 \\
0.00 & 0.00 & 0.00 & 0.00 & 0.00 & 0.00 & 0.00 \\
0.00 & 0.00 & 0.00 & 0.00 & 0.00 & 0.00 & 0.00 \\
0.00 & 0.00 & 0.00 & 0.00 & 0.00 & 0.00 & 0.00 \\
0.00 & 0.469794 & -0.838533 & 0.650334 & -0.185432 & 0.362058 & 0.362058 \\
0.00 & 0.00 & 5.302141 & 0.00 & 0.00 & 0.00 & 0.00 \\
0.00 & -2.702760 & -0.046218 & -6.558172 & -6.604237 & -10.250666 & -10.250666 \\
0.00 & 0.00 & 0.00 & 0.00 & 0.00 & 0.00 & 0.00 \\
0.00 & 0.00 & 0.00 & 0.00 & 0.00 & 0.00 & 0.00 \\
0.00 & 0.00 & 0.00 & 0.00 & 0.00 & 0.00 & 0.00 \\
0.00 & 0.00 & 0.00 & 0.00 & 0.00 & 0.00 & 0.00 \\
0.00 & 0.00 & 0.00 & 0.00 & 0.00 & 0.00 & 0.00
\end{bmatrix} \quad (C.5)$$